2005

SURFO Technical Report No. 2006-01

SURFO

Recommended Citation

SURFO, "SURFO Technical Report No. 2006-01" (2005). *SURFO Technical Reports.* Paper 7.
http://digitalcommons.uri.edu/surfo_tech_reports/7

Papers from
the

SUMMER UNDERGRADUATE RESEARCH FELLOWSHIP PROGRAM IN OCEANOGRAPHY

at

THE UNIVERSITY OF RHODE ISLAND
Graduate School of Oceanography
and
Department of Ocean Engineering

NARRAGANSETT, RHODE ISLAND

June - August 2005

UNIVERSITY OF RHODE ISLAND
URI
GSO
SUMMER FELLOWSHIP IN OCEANOGRAPHY

This program was funded by Grant OCE-0243794 from the National Science Foundation.

GSO Technical Report No. 2006-01

PARTICIPANTS IN THE 2005 SUMMER UNDERGRADUATE RESEARCH FELLOWSHIP PROGRAM IN OCEANOGRAPHY

FELLOWS

Rika Anderson	Carleton College, Northfield, MN
Ilana Cohen	Brandeis University, Waltham, MA
Ben Diehl	Brandeis University, Waltham, MA
Nicole M. La Sota	Rutgers University, New Brunswick, NJ
Dave Lishego	Pennsylvania State University, University Park, PA
Kevin Miklasz	University of Chicago, Chicago, IL
Melinda Montano	Eckerd College, St. Petersburg, FL
Argenta Price	Yale University, New Haven, CT
Amanda Shields	Winona State University, Winona, MN
Betsy Zunk	Muskingum College, New Concord,OH

ADVISORS

Deanna Bergondo
Jeremy Collie
Peter Cornillon
Steven D'Hondt
Kathy Donohue
Tetsu Hara
Chris Kincaid
Rainer Lohmann
Kathryn Moran
Robert Pockalny
Vitalii Sheremet
David C. Smith
Bruno Soffientino
Arthur Spivack
Randy Watts

PROGRAM ASSISTANTS

Chris Popham, Kim Carey & Rhonda Kenny

PREFACE

This report presents the papers written by the 10 participants in the 2005 Summer Undergraduate Research Fellowships in Oceanography (SURFO) program at the Graduate School of Oceanography (GSO), University of Rhode Island (URI). This past summer represented the 19th year in which the program has been coordinated and extended through the several disciplines in oceanography and ocean engineering at URI's Narragansett Bay Campus. The 2005 program continued excellence beyond the official duration of the program with at least one project resulting in a manuscript to be submitted for publication. In addition, five presentations were made at national meetings, including AGU and ASLO.

During the fall of 2004 advertisements were sent to physics, chemistry, biology and geology departments, including faculty advisors at a number of minority colleges.. Flyers and overheads were provided to colleagues presenting invited talks at various undergraduate institutions. The SURFO web site has continued to be updated and more useful links describing possible research programs at GSO/URI have been added. We received 78 applications for the program, and about two-thirds of these applicants used the electronic application form. This represents the third consecutive year that about two-thirds of the students have used the SURFO website to apply electronically. Ten students were selected for the program with a breakdown by oceanographic discipline as follows: 2 Geological, 3 Physical, 1 Chemical, 2 Biological, 2 Astrobiological. The gender break-down returned to a female majority (7 female, 3 male) and two participants were from under-represented groups in science.

The timeline of the 11-week program was adjusted slightly this year to provide students with an extended orientation period during the first two weeks. This orientation period began with a breakfast to welcome the new students and introduce them to the GSO campus community, and was followed by a tour of the campus and facilities. For the next 5 work days, daily background/introductory seminars were presented by graduate students from the various sub-disciplines of oceanography, including: biological oceanography, marine and atmospheric chemistry, marine geology & geophysics, physical oceanography, and ocean engineering. During the remainder of the program weekly seminars (on Tuesdays) on “hot topics” in oceanography were presented by a GSO faculty member or marine scientist. On Thursdays of each week, a professional development workshop or discussion was held to round-out the students experience. Topics such as “learning/research styles”, “scientific writing and effective presentations”, and “hands-on modeling methods” were provided..

We continued an informal round-table meeting with several faculty members, graduate students and SURFOs to discuss how to get into graduate school and what will be expected of them. We also instituted a similar round-table format to discuss possible careers in oceanography. Our exit questionnaires revealed that students found these seminars interesting and very useful, and the exposure to a wide range of disciplines/research topics helped students identify additional areas of interest. Other undergraduates (NOT affiliated with the SURFO program) working at EPA or NOAA labs on the Bay Campus and even graduate students at GSO also attend many of these seminars.

Included in the summer events was our annual day of kayaking in Wickford Harbor, led by Bob Sand, to investigate the flora and fauna of an estuary. A subset of SURFOs also participated in a series of field days funded by other projects where water sampling and fish trawls were made at several locations in Narragansett Bay and Rhode Island Sound. We also continued with our tradition of having an informal noon-time barbecue each Friday for the SURFOs on the veranda at the Horn Lab. This provided the SURFOs with a taste of graduate-student life in an informal setting where they were able to meet with GSO faculty, graduate students and staff. The annual SURFOs vs ADVISORS softball game was won by the advisors, and continued the advisors undefeated streak.

One measure of success of our program is if fellows continue on with graduate studies in science and, specifically, in oceanography or ocean engineering. The exit questionnaire and follow-up conversations indicate that 9 of 10 the students definitely plan to continue on with graduate studies in science/engineering. Of these, 6 said they are seriously considering oceanography. Three of the students have applied to GSO for the fall 2005 semester.

The participants in the 2005 SURFO program are grateful to the National Science Foundation for its support of the program through grant OCE-0243794. The NASA Astrobiological Institute at GSO/URI (Steve D'Hondt, David Smith and Art Spivack) also provide supplemental funds for Rika Anderson. The SURFO participants and I would like to thank all of those individuals at URI who contributed to the program's success including those who advised the students and who gave SURFO seminar presentations. In addition, our thanks to Rhonda Kenny and Kim Carey for their assistance in the preparation of this report as well as the administrative, financial and recruitment tasks. Finally, we would like to thank Chris Popham who served as a graduate coordinator for the program, Friends of Oceanography for providing seminar refreshments, and Bob Sand for running the kayak trip.

Robert A. Pockalny
SURFO Site Director

TABLE OF CONTENTS

A Test for Phylotype Bias in a Cell Separation Protocol Using 16S rRNA-Based Techniques

Rika Anderson[1] and David C. Smith

Graduate School of Oceanography, University of Rhode Island, Narragansett, Rhode Island

Abstract. Studies have shown that the deep marine biosphere harbors a significant amount of biomass and plays an important role in global biogeochemical cycles. To facilitate studies of microbial communities residing in marine sediments, a number of protocols have been designed to separate the cells from the sediment matrix. A separation protocol currently being developed has been shown to successfully remove up to 70% of the cells from the sediment. In order for a cell separation protocol to provide an accurate representation of microbial communities, it is necessary that the technique remove all phylotypes without bias. Our study uses molecular techniques to provide a qualitative comparison of genetic diversity in cells that have been separated from a sediment sample and cells that are left in sediments after separation. 16S rRNA genes in DNA extracted from these samples are amplified through polymerase chain reaction and then compared through denaturing gradient gel electrophoresis. Resulting band patterns are compared between samples to determine if the genetic diversity of the separated cells has been altered by the cell separation protocol. This will allow us to determine whether or not the protocol provides a true random sample of the microbial community in sediment samples.

1. Introduction

A large fraction of the Earth's biomass resides within the deep marine subsurface, harboring diverse microbial communities of both *Bacteria* and *Archaea* as deep as 800 mbsf and as old as 15 million years (Webster et al., 2003; Kormas et al., 2003). Studies of the Deep Biosphere have shown that the microbial communities residing in this environment are more physiologically and phylogenetically complex than previously thought (Amend and Teske, 2005). To better understand the organisms residing in deep subsurface sediments, scientists often employ the use of 16S rDNA for detection of novel organisms or for indications of genetic diversity (Teske et al., 2002, Kormas et al., 2003, Newberry et al., 2004). However, PCR amplification of DNA extracted directly from environmental samples is often hindered by the presence of PCR inhibitors co-purified in soils, such as humic acids (Gonzalez et al., 2005). Thus, whole-cell separation protocols have been developed to separate cells from the sediment matrix in order to more easily analyze the diversity of microbial communities residing in sediments (Frischer et al., 2000).

A cell separation protocol currently being developed in this lab employs the use of detergents and enzymes to degrade the extracellular matrix, followed by the addition of a density liquid and centrifugation to separate low-density cells from high-density sediment. However, the current cell separation protocol is unable to extract 100% of all cells in the sediment matrix. Therefore in order for the cell separation procedure to give an accurate representation of the diversity of microbial communities residing in sediments, cells must be separated without regard to their physiology or phylogeny. The aim of this study was to determine if the cell separation protocol currently being developed provides an accurate representation of microbial communities residing in sediments. To test the hypothesis that cells are separated from sediments without bias, we amplified 16S rDNA in both *Bacteria* and *Archaea* and performed DGGE to compare the relative genetic diversity of microbial communities in intact sediment samples and in separated cell samples.

2. Materials and Methods

2.1. Sediment Samples; DNA Extraction and Purification

All sediment samples for this investigation were obtained from the Salt Pond Marina in Narragansett, RI and cells were separated from the sediment matrix according to a cell separation protocol currently being developed. Samples of intact sediment, separated cells (supernatant) and residual sediment and cells after separation (pellet) were stored at -80°C until processing. DNA was extracted from sediment samples with three different kits. DNA was extracted from 0.5 g intact sediment and pellet samples and 300 μl of supernatant using the FastDNA Spin Kit for Soil (QBiogene, Irvine, CA, USA) with modifications as described by Webster et al. (2003). DNA was also extracted from 50 mg of intact sediment and 1 ml of supernatant using the Bactozol TRI reagent extraction kit (Molecular Research Center, Cincinnati, OH, USA) according to the manufacturer's protocol. A third DNA extraction was carried out on 0.25 g of intact sediment and pellet samples and from 200 μl of supernatant samples using the PowerSoil DNA Isolation Kit (MoBio Laboratories, Inc., Solana Beach, CA, USA) according to the manufacturer's protocol, with the exception of adding 200 μg polyadenylic acid to the lysis mixture, eluting in 100 μl sterile distilled water and collecting in 1.5 ml Fisherbrand siliconized/low retention microcentrifuge tubes (Fisher Scientific, Hampton, NH, USA). DNA was also purified after extraction with Microcon

---

[1] Carleton College, Northfield, MN, 55057

Centrifugal Filter Devices (Millipore, Billerica, MA, USA) and Centri-Spin Columns (Princeton Separations, Inc., Adelphia, NJ, USA). DNA was quantified with a NanoDrop spectrophotometer (NanoDrop Technologies, Wilmington, DE, USA).

2.2. PCR Amplification of 16S rRNA Gene sequences

Primers used for nested PCR amplification of 16S rRNA genes in *Bacteria* and *Archaea* are listed in Table 1. All amplification reactions were performed in sterile conditions with a PTC-100 thermal cycler (MJ Research, Inc., Waltham, MA, USA) in 0.5 ml thin-walled reaction tubes. Success of PCR amplification was determined using gel electrophoresis on 2% agarose gels stained with ethidium bromide and visualized with UV illumination. Negative controls were included in all reaction mixes by substituting template DNA with molecular grade water to provide a contamination check.

Primary amplification of *Bacteria* 16S rDNA was performed using a reaction mixture of 25 µl Master Mix (1.25 units *Taq* Polymerase, 1x QIAGEN PCR Buffer, 200 µM each dNTP; QIAGEN Inc., Valencia, CA, USA), 2.5 µl each of primers 27F and 1492R (Integrated DNA Technologies, Inc., Coralville, IA, USA), and 5 µl template DNA, made up to 50 µl with molecular grade water. Intact sediment DNA was diluted 1:1000 and pellet DNA was diluted 1:100 to overcome PCR inhibition problems. Reaction mixtures were held at 94˚C for 3 min followed by 35 cycles of 94˚C for 30 s, 45˚C for 30s, and 72˚C for 90s, with a final extension step of 10 min at 72˚C. Nested PCR amplification of *Bacteria* 16S rDNA was performed with 2.5 µl each of primers 357F-GC and 518R, 25 µl MasterMix, and 1 µl of PCR product diluted 1:1000 as template DNA. Reaction mixtures were brought up to 50 µl with molecular grade water. Reaction mixtures were held at 94˚C for 3 min followed by 35 cycles of 94˚C for 30 s, 54˚C for 30s, and 72˚C for 1 min, with a final extension step of 10 min at 72˚C.

Archaea 16S rDNA was amplified with 1/10 dilutions of extracted DNA from intact sediment and pellet samples using primers Arch21F and Arch958R. Reaction mixtures included 25µl MasterMix, 2.5 µl each primer, and 5 µl template DNA, brought up to 50 µl with molecular grade water. Reaction conditions included an initial 94˚C for 3 min, followed by 35 cycles of 94˚C for 30s, 45˚C for 30s, and 72˚C for 1 min, with a final extension of 72˚C for 10 min. Nested PCR amplification of *Archaea* 16S rDNA was performed using primers SAf and PARCH519R with the same nested PCR reaction mixture as above. Reaction mixtures were held at 94˚C for 3 min, followed by 35 cycles of 94˚C for 30s, 53˚C for 30s, and 72˚C for 1 min, with a final extension step of 10 min at 72˚C.

2.3. DGGE Analysis

Amplified 16S genes from *Bacteria* and *Archaea* were compared through denaturing gradient gel electrophoresis (DGGE) as described previously (Muyzer et al., 1993). PCR product was separated according to base sequence using 30% acrylamide gels with a denaturant gradient between 30-60%. 100% denaturant was defined as 105 g urea, 100 ml formamide, 52.5 ml 38% acrylamide stock, and 2.5 ml 50x TAE, made up to 250 ml with deionized water. Gels were poured with the aid of a 20 ml gradient maker (CBS Scientific Co., Del Mar, CA, USA). Electrophoresis was run for 16 hours at 75 volts in 0.5x TAE. Gels were stained with 10 µl SYBRGreen in 100 ml of 0.5x TAE and visualized with UV illumination.

3. Results and Discussion

3.1. Extraction and Amplification of 16S rDNA

The presence of co-purified PCR inhibitors in extracted DNA prevented successful amplification of the 16S gene in both *Bacteria* and *Archaea*. Humic acids are among most commonly reported PCR inhibitors co-extracted from sediments. Many extraction and purification procedures have been used to prevent PCR inhibition by these compounds, but many of these methods are inconsistent or are specific to the sediments used (Gonzalez et al., 2005; Webster et al., 2003, Sørensen et al., 2004). The PowerSoil kit, which has been specifically designed to target humic acids and includes a solvent meant to precipitate organic compounds that act as potential PCR inhibitors, was the only consistently successful means of extracting purified. Some success was also had in the use of serial dilutions to dilute humic acids enough to effectively prevent them from interfering with the PCR reaction.

Amplification target	Primer code	Sequence 5'-3'	Approx. product size (bp)
General 16S rDNA for	27F	AGA GTT TGA TCM TGG CTC AG	1502
Bacteria	1492R	GGT TAC CTT GTT ACG ACT T	
General 16S rDNA for	Arch21F	TTC CGG TTG ATC CYG CCG GA	1362
Archaea	Arch958R	YCC GGC GTT GAM TCC AAT T	
General 16S rDNA for	357F-GC	CCT ACG GGA GGC AGC AG	194
Bacteria for DGGE	518R	ATT ACC GCG GCT GCT GG	
General 16S rDNA for	SA1f	CCT AYG GGG CGC AGC AGG	150
Archaea for DGGE	SA2f	CCT ACG GGG CGC AGA GGG	
	PARCH519r	TTA CCG CGG CKG CTG	

Table 1. PCR primers used in this study. All primer sequences were obtained from Newberry et al. (2004).

Successful amplification was achieved from DNA extracted with the FastDNA extraction kit that had been pooled and purified with Microcon Centrifugal Filter Devices and diluted 1/100, but amplification success from DNA extracted with this kit was inconsistent. In contrast, all dilutions of both purified and unpurified DNA extracted by PowerSoil kit were successfully amplified. Figure 1 depicts gel electrophoresis of the amplified 16S rRNA gene in *Bacteria* and *Archaea* from DNA that had been extracted with the PowerSoil kit. Nested PCR was also successful from DNA amplified with this method, as depicted in Figure 2.

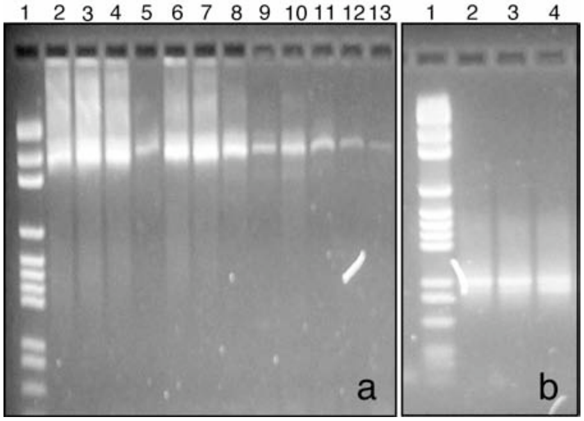

Figure 1. a) Gel electrophoresis of amplified 16S rDNA in *Bacteria* from DNA extracted with the PowerSoil extraction kit from Salt Pond sediment samples. Lane 1, BenchTop pGEM DNA marker; lanes 2-4, intact sediment; lanes 5-8, pellet; lanes 9-12, supernatant. **b)** Gel electrophoresis of nested PCR product in *Bacteria*. Lane 1, BenchTop pGEM DNA marker; lane 2, intact sediment; lane 3, pellet; lane 4, supernatant.

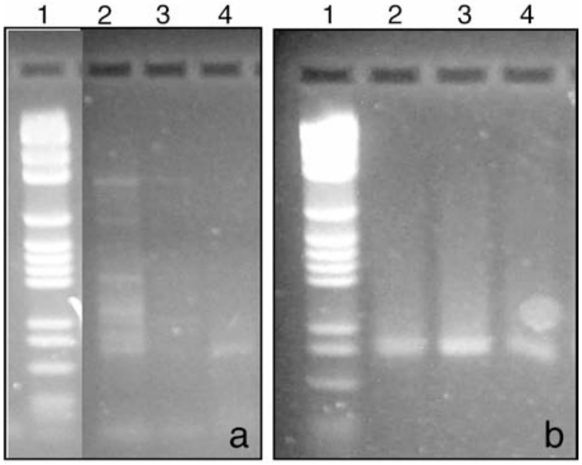

Figure 2. a) Gel electrophoresis of amplified 16S rDNA in *Archaea* from DNA extracted with the PowerSoil extraction kit from Salt Pond sediment samples. Lane 1, BenchTop pGEM DNA marker; lane 2, intact sediment; lane 3, pellet; lane 4, supernatant. **b)** Gel electrophoresis of nested PCR product in *Archaea.* Lane 1, BenchTop pGEM DNA marker; lane 2, intact sediment; lane 3, pellet; lane 4, supernatant.

3.2. DGGE Analysis of Relative *Bacterial* and *Archaeal* Diversity

Denaturing gradient gel electrophoresis profiles of 16S rRNA genes indicate that there are clear differences between intact sediment, pellet and supernatant samples. 16S genes amplified with *Bacteria* primers indicate that some phylotypes are present in intact sediments that do not appear in the separated cells. Figure 3 indicates that at least three bands (1, 2, and 3) appear in the lanes containing DNA extracted from intact sediment and pellet samples, but do not appear in supernatant samples. As individual bacteria may possess multiple, distinct copies of the 16S gene, these data indicate that at least one phylotype is not successfully separated into the supernatant in the cell separation process.

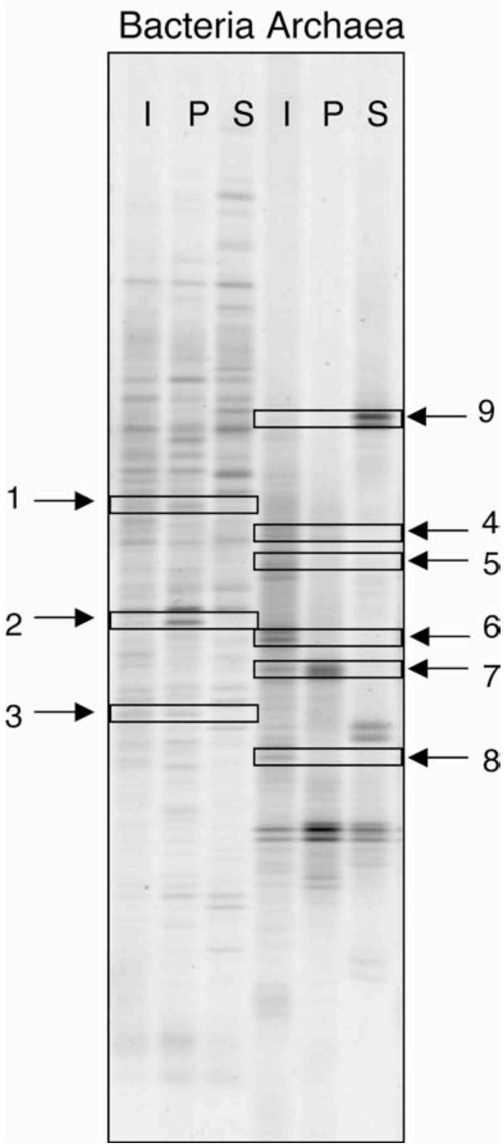

Figure 3. Denaturing gradient gel electrophoresis profiles of 16S rRNA genes in intact sediment (I), pellet (P) and supernatant (S) samples. Genes were amplified with nested PCR with *Bacteria* primers 357F-GC and 518R and with *Archaea* primers SAf and PARCH519r. Gel was stained with SYBRGreen nucleic acid stain.

DGGE profiles of 16S rRNA genes amplified with *Archaea* primers also initially suggest that not all phylotypes in this domain are successfully separated from sediments. As indicated in Figure 3, at least five bands (4, 5, 6, 7, and 8) are present in intact sediment samples and absent from supernatant samples. This indicates that there is a possible bias in the cell separation procedure as some phylotypes that were originally present in intact sediment samples are not successfully separated into the supernatant.

While all *Bacteria* bands that are absent in supernatant lanes appear in both intact sediment and pellet lanes, within the *Archaea* there exist some bands that are absent from both pellet and supernatant lanes, such as band 5. The cause of this may have been destruction of the cells through cell wall rupture or a similar mechanism following sonication, leaving these cells in the density liquid or otherwise preventing extraction of their DNA in either the supernatant or pellet samples.

In both *Bacteria* and *Archaea* samples, some bands are present in supernatant lanes that are absent from both intact sediment and pellet lanes, indicating the presence of some phylotypes in supernatant samples that do not appear in intact or pellet samples. Band 9 is a particularly bright example of this occurrence. A likely explanation for this is PCR bias. In the diverse microbial community of intact sediments, this particular phylotype may have been too dilute for visible amplification to occur, while other phylotypes were preferentially amplified. After separation, however, this phylotype may have become relatively more dominant and thus produced a visible band after amplification. An alternative explanation is contamination, which is possible for *Bacteria* samples but is unlikely for *Archaea* due to the relative scarcity of *Archaea* in potential contamination sources.

Some instances occur in both the *Bacteria* and the *Archaea,* such as bands 2 and 7, in which the pellet band is darker or more saturated than the corresponding intact sediment band and absent from the supernatant lane. This may be the result of a failure to separate these phylotypes from the sediments. These phylotypes would thus be left behind and become more dominant in the pellet, creating a stronger signal after amplification in the pellet than it had in the more diverse intact sediments.

4. Conclusion

Initial analysis indicates that a bias does exist in the cell separation procedure currently being developed in this lab. This would imply that this procedure does not provide an accurate profile of the diversity of the microbial community residing in sediments. Certain phylotypes are excluded in the separation and are left in either the pellet, as indicated by bands present in both intact sediment and pellet lanes, or possibly destroyed or left in the density liquid, as suggested by bands present only in intact sediment lanes.

Further studies and replication of results are required to affirm these findings. Successful extraction and amplification was achieved with sediments obtained from the Western Arabian Sea Transect (WAST), and thus it would be informative to repeat this test with these sediments as well. Extraction and amplification of DNA found in the density liquid would indicate whether or not certain phylotypes are left in the density liquid rather than in the pellet or supernatant. Finally, it is important to note that interpretation of the gel image is often subjective when analyzed visually due to the presence of faint bands, and thus would greatly benefit from a more stringent data imaging analysis to definitively indicate the presence or absence of bands when the visual image is ambiguous.

Acknowledgments. The authors would like to thank Dr. Jens Kallmeyer for providing sediment samples for analysis, as well as Dr. Andrew Staroscik for his aid in DGGE analysis. We also thank Stephanie Forschner and the lab of Dr. Dave Rowley for their collaboration and support in DNA extraction methods, and Dr. Andreas Teske for his advice regarding DNA purification from sediments.

References

Amend, J.P. and Teske, A., Expanding frontiers in deep subsurface microbiology, *Palaeogeogr. Palaeoecol., 219*, 131-155, 2005.

Frischer, M.E., Danforth, J.M, Newton Healy, M.A., and Saunders, F.M., Whole-Cell versus Total RNA Extraction for Analysis of Microbial Community Structure with 16S rRNA-Targeted Oligonucleotide Probes in Salt Marsh Sediments, *Appl Environ Microbiol., 66(7),* 3037-3043, 2000.

Gonzalez, J.M., Portillo, M.C., and Saiz-Jimenez, C., Multiple displacement amplification as a pre-polymerase chain reaction (pre-PCR) to process difficult to amplify samples and low copy number sequences from natural environments, *Environ Microbiol., 7(7)*, 1024-1028, 2005.

Kormas, K.A., Smith, D.C., Edgcomb, V., Teske, A., Molecular analysis of deep subsurface microbial communities in Nankai Trough sediments (ODP Leg 190, Site 1176), *FEMS Microbiol Ecol., 45,* 115-125, 2003.

Muyzer, G, De Wall EC, Uitterlinden AG, Profiling of complex microbial populations by denaturing gradient gel electrophoresis analysis of polymerase chain reaction-amplified genes coding for 16S rRNA, *Appl. Environ. Microbiol, 59,* 695-700, 1993.

Newberry, C.J., Webster, G., Cragg, B.A., Parkes, R. J., Weightman, A.J., and Fry, J.C., Diversity of prokaryotes and methanogenesis in deep subsurface sediments from the Nankai Trough, Ocean Drilling Program Leg 190, *Environ Microbiol*., 6(3), 274-287, 2004.

Teske, A., Hinrichs, K-U., Edgcomb, V., de Vera Gomez, A., Kysela, D., Sylva, S.P., Sogin, M.L., and Jannasch, H.W., Microbial Diversity of Hydrothermal Sediments in the Guaymas Basin: Evidence for Anaerobic Methanotrophic Communities, *Appl Environ Microbiol., 68(4),* 1994-2007, 2002.

Webster, G., Newberry, C.J., Fry, J.C., and Weightman, A.J., Assessment of bacterial community structure in the deep sub-seafloor biosphere by 16S rDNA-based techniques: a cautionary tale, *J. Microbiol. Methods., 55*, 155-164, 2003.

R. E. Anderson and D. C. Smith, Graduate School of Oceanography, University of Rhode Island, Narragansett, RI 02882. (andersor@carleton.edu, dcsmith@gso.uri.edu)

The Origin and Distribution of Organic Pollutants in the Surface Water of Narragansett Bay

Ilana Cohen,[1] Eric Morgan, and Rainer Lohmann

Graduate School of Oceanography, University of Rhode Island, Narragansett, Rhode Island

Abstract. In a bay environment, understanding the distribution of persistent organic pollutants (POPs) between the air, water, and particulate phases is key to predict their bioaccumulation and sedimentation rates. In this study, the partitioning of polycyclic aromatic hydrocarbons (PAHs) was investigated in weekly air and water samples. Surface water samples were taken from Narragansett Bay, RI and air samples from the nearby University of Rhode Island Graduate School of Oceanography campus. In the laboratory, seawater was filtered and both phases extracted to obtain solid-bound and dissolved fractions of PAHs identified by gas chromatography-mass spectrometry (GC-MS). Total Suspended Solids (TSS) and carbon and nitrogen analysis (CHN) were used to calculate the concentration of PAHs in the organic carbon fraction. These data, with the PAH concentrations detected in the dissolved phase, were used to calculate the particulate-water distribution coefficient (K_{pw}). Chl-a data, used as a proxy for phytoplankton concentration, was examined to determine if the PAH concentration in the carbon/TSS could be considered equivalent to the PAH concentration in phytoplankton. The concentration of PAHS in the air, as determined by GC-MS analysis was used to derive the relative chemical activities of the pollutants in phytoplankton/TSS, the water column and the gas phase. This study focused on determining the details needed for the proper water analysis procedure, the potential for use of pre-made cartridges to extract the dissolved compounds, the validity and implications of the determined distribution constants, and the appropriateness of associating PAH concentrations in phytoplankton with PAH concentrations in TSS and carbon concentrations. The results indicate that the procedure is highly delicate, yet may be sensitive enough to detect changes in the equilibrium of pollutants in the bay. Additionally, the pre-made cartridges failed to function as an efficient substitute for extracting PAHs from the liquid phase. Finally, there was an indication that PAHs in the water are being absorbed by non-living, particulate material.

1. Introduction

The persistent organic pollutants classified as PAHs (polycyclic aromatic hydrocarbons) have chemical properties allowing them to transfer between gas, water, and solid phases as well as bioaccumulate in the tissues of living organisms. Proceeding air-water exchange, phytoplankton in the surface waters absorb the lipophylic PAH molecules from the surrounding water and then either sink to the bottom of the ocean, in which case the PAHs are removed from the cycle, or are consumed, allowing the PAHs to travel through food webs, being metabolized by some organisms. These toxic pollutants effect reproduction and can be carcinogenic [K.C. Jones, P de Voogt, 1999] indicating the need for significant study of the flux of POPs in the environment.

Pollutants move through environmental phases to establish chemical equilibrium. This equilibrium is quantified by the distribution coefficient, or the ratio of the pollutant concentrations in two different phases. The air-water distribution coefficient (Kaw) is described by equation 1 and the particulate-water distribution coefficient (Kpw) is described by equation 2:

$$Kaw = Ca/ Cw \quad (1)$$

$$Kpw = Cp/C\ w \quad (2)$$

where, Ca is the concentration of PAHs in the air (ng/L), Cw is the concentration of PAHs in the water (ng/L) and Cp is the concentration of PAHs in the organic carbon of the total suspended solids (TSS). As a reference, Kpw values can be compared to literature Kow values which describe the chemical's partitioning between water and octanol (equation 3)

$$Kow = Co/Cw \quad (3)$$

where Co is the PAH concentration in octanol (ng/L) and the Cw is the PAH concentration in water (ng/L). Due to octanol's comparability to the biochemical composition of organic matter, the Kow is used as a point of reference for experimentally determined Kpw values.

To consider the complexity in associating the PAH concentration in carbon with only phytoplankton, a measurement of black carbon was also taken to determine if some of the PAHs were actually associated with black carbon, rather than phytoplankton. The concentration of PAHs in the TSS was also calculated in order to analyze PAH association with solids other than matter containing organic carbon and black carbon The total suspended solids- water distribution coefficient (Ksw) is described by equation 4, where Cs is the PAH concentration in the suspended solids (ng/kg TSS).

$$Ksw = Cs/Cw \quad (4)$$

2. Methods

This study focused on the proper procedure for a liquid extraction of PAHs from the seawater in order to

---

[1] Now at Brandeis University, Waltham, Massachusetts

get accurate data for these equations. Additionally, a substitute method using a pre-made C_{18} cartridge (Waters Sep-Pak® Vac) was tested for its reliability. Preliminary data about the flux of PAHs in the Narragansett Bay was collected and analyzed, and the validity of using carbon as a proxy for phytoplankton concentrations was questioned.

Data was collected weekly, at two sampling stations, one for air, located on the roof of the CACS building of the University of Rhode Island Graduate School of Oceanography, and the other for water, in the Narragansett Bay at 41˚ 34.24 N, 7 1˚ 24.34 W. Air and water samples were taken on corresponding days. Control water samples were run with pre-extracted mili-Q water, and field and lab blanks were run as controls to correspond with the air samples. To eliminate laboratory contamination, water and air samples came in contact with only metal, glass, and teflon laboratory equipment.

Using a vacuum pump, 3-4 L of seawater were filtered through a pre-baked, glass fiber filter (Gelman Sciences® Type A/E 142 mm) to separate the particulate from the dissolved phase. 50µl of an internal standard [d_{10}-anthracene 40.04 µg/mL, in acetone] was added to the liquid fraction and to the filter containing the particulate fraction. PAHs in the liquid phase were extracted with a series of three 150 ml additions of dichloromethane (DCM); PAHs in the particulate phase were extracted in three, 15 minute sonifications, each in 70-90 ml of DCM. The extractions from each fraction were collected into corresponding round bottom flasks and approximately 0.5 mL of iso-octane was added to prolong the final stage of evaporation.

For some weeks, a duplicate 3-4 L sample of water was filtered as described above, and then the liquid fraction pumped through a pre-made C_{18} cartridge as a replacement for the liquid-liquid extraction process. The cartridge was first rinsed with 18 ml DCM, and then conditioned with 18 ml methanol, followed by 18 ml mili-Q water. 50 µL of the previously mentioned internal standard was added directly to the cartridge prior to the addition of the sample. PAHs were eluted from the cartridge by an addition of 4 ml of methanol, which was discarded, followed by 2 ml of methanol and 20 ml DCM, which contained the PAHs. For convenience of rotary evaporation 200 ml of DCM and approximately 0.5 mL of iso-octane were added (to rid the samples of methanol).

The samples were concentrated to 25-100 µl using a rotary evaporator. After transfer to a GC vial with a volume saving insert, 10 µL of a d_{10} pyrene standard [4.78 ng/µL, in octane] was added. The peaks from the GC-MS were analyzed for the presence of the PAHs in Table A, and the deuterated compounds from the two standards. The amount of each PAH was calculated relative to d_{10}-anthracene.

A volume of 500 mL of seawater was also filtered through a pre-weighed and pre-baked glass fiber filter (Whatman® GF/C 55 mm) which was run through a CHN analyzer to determine the amount of carbon and nitrogen in the particulate. A section of the filters was then baked again at 375 ºC for 24 hours, ridding the filter of any organic carbon and leaving behind any black carbon to be detected by a second CHN analysis. Additionally, an arbitrary amount of filtered water was collected for a dissolved organic carbon analysis, but this analysis has yet to be completed.

Two air samples were taken separately from the night before the water sampling date, and then through the day of the water sampling. The flow of air was measured at the start of each sampling period and the time noted. Air was pumped first through a Wilkem Scientific® Grade A-E 8” x 10” pre-baked glass fiber filter and then through two pre-extracted 3” x 3” polyurethane plugs (Tisch Environmental®), placed into a glass cartridge, one on top of the other. The majority of PAHs was detected in the plugs, hence the results from the filters are not included in the analysis. After sampling, 100 µL of standard SRM 2269 [d_{10}-phenanthrene 24.76 µg/mL, d_{10}-flouranthrene 41.6 µg/mL, d_{12}-benz[*a*]anthracene 25.22 µg/mL in iso-octane] was added to the plugs. After soxhlet extraction with DCM, the samples were cleaned up using activated silica gel. The final volume was then reduce to approximately 100 µl first by rotary evaporation, and then under nitrogen. 5-15 µL of the same deuterated pyrene standard as mentioned previously was added to the samples once they were in GC vials with inserts. The peaks from these samples were quantified by a comparison of the desired PAH to the deuterated PAH from the standard with the closest mass.

3. Results and Discussion

3.1 Water Analysis

The complete analysis of the particulate, water, and air fractions focused on the weeks of July 18th and July 25th , 2005, when the most reliable data was obtained. Most of the initial results from the water analysis indicated contamination in the liquid-liquid extraction procedure, thus modifications were made until concentrations of selected PAHs were lower in the control than in the samples. The GC-MS was not always able to detect anthracene and acenaphthene; frequently phenanthrene concentrations in the sample were very similar to the concentrations in the control, thus these compounds were sometimes left out of the analysis. The

PAH	mass (amu)	Kaw	Kow
acenaphthene	154	5.93×10^{-3}	1.04×10^{4}
phenanthrene	178	1.34×10^{-3}	4.47×10^{4}
anthracene	178	9.83×10^{-4}	4.24×10^{4}
methylphenanthrene	192	2.02×10^{-3}	1.38×10^{5}
pyrene	202	5.02×10^{-4}	1.40×10^{5}
flouranthrene	202	5.39×10^{-4}	1.31×10^{5}
benz[a]anthracene	228	3.84×10^{-4}	8.13×10^{5}
chrysene	228	3.88×10^{-5}	2.77×10^{5}

Table A. PAHs considered and their properties. Distribution constants from Beyer 2001, except for methylphenanthrene from Bamford, 1999 using Henry’s Law Constant.

PAHs	July 18th				July 25th			
	liquid-liquid control (ng/L)	liquid-liquid seawater (ng/L)	cartridge control (ng/L)	cartridge seawater (ng/L)	liquid-liquid control (ng/L)	liquid-liquid sample (ng/L)	cartridge control (ng/L)	cartridge sample (ng/L)
Ace	0.91	5.79	17.98	73.44	nd*	8.89	60.72	16.15
Phen	13.05	28.00	39.82	29.25	15.96	31.76	70.14	12.29
An	1.46	5.06	7.05	14.30	nd	nd	nd	3.86
Me-Phen	4.47	18.55	20.93	27.95	nd	27.95	13.61	7.35
Pyr	22.54	10.28	207.74	31.85	11.05	76.22	82.71	5.90
FlAn	30.12	10.38	242.10	59.79	nd	90.82	14.66	6.63
BaA	4.56	1.60	30.26	15.60	nd	12.70	nd	nd
Chr	20.35	1.76	162.69	14.95	nd	76.22	nd	nd

Table B. PAH Concentrations in the liquid fraction (ng/L) for July 18th and July 25th. *nd= not detected.

PAHs	July 18th			July 25th		
	control (ng/L)	seawater particulate (ng/L)	seawater particulate (ng/kg carbon)	control (ng/L)	seawater particulate (ng/L)	seawater particulate (ng/kg carbon)
Ace	nd*	nd		nd	nd	
Phen	17.37	18.49	3.85×10^7	7.12	9.93	2.36×10^7
An	0.00	2.84	5.93×10^6	nd	nd	
Me-Phen	2.68	7.65	1.59×10^7	nd	1.60	3.81×10^6
Pyr	2.18	18.49	3.85×10^7	1.88	18.89	4.50×10^7
FlAn	6.78	24.89	5.19×10^7	3.28	21.13	5.03×10^7
BaA	nd	2.13	4.45×10^6	0.78	3.20	7.62×10^6
Chr	3.92	7.11	1.48×10^7	2.58	6.56	1.56×10^7

Table C. PAH Concentrations in the Particulate Fraction (ng/L) for July 18th and July 25th. *nd= not detected.

PAH concentrations in each fraction and the controls for July 18th and July 25th are shown in Tables B and C. In Table C, the PAH concentration in the particulate is corrected to the ng/kg carbon as it was used for final calculations.

The results in Table B clearly indicate that the pre-made cartridges were not appropriate for this study due to the high concentrations of PAHs found in the cartridge controls in both weeks. Comparing the liquid-liquid extraction data from the two days, a small change in the distribution of PAH concentrations on the 25th was observed. The concentrations of PAHs in the water on July 25th increased from the concentrations detected on the 18th, while the PAH concentrations in the carbon particulate are similar between the two dates (Table C). For example, pyrene increased from 10.28 ng/L to 76.22 ng/L in the dissolved fraction, yet only from 3.85×10^7 ng/kg to 4.50×10^7 ng/kg in the particulate. The increase in concentrations of PAHs in the particulate phase, without a corresponding increase in dissolved PAHs, suggest that the particulate-water system was not at equilibrium at the time the sample was taken on the 25th.

3.2 PAH concentrations in air and water

From the C-water and the C-air, the Kaw value can be calculated and compared to a literature Kaw value, as shown in Figures 1a and 1b. In these graphs, the experimentally determined Kaw values from the C-air during the night and the Kaw values from the C-air during the day were calculated separately.

On July 18th, the night and day Kaw values were both close to the literature values, due to similar night and day concentrations in PAHs. However, on July 25th, the PAH concentrations in the daytime air sample were relatively higher, than in the nighttime sample (data not shown). The Kaw values calculated from the day air samples correlate more closely with the published Kaw values, confirming that the higher PAH levels detected during the day were at equilibrium with water.

Correspondingly, if the PAH concentration in water is viewed as a function of the Kaw, the higher C-air values at equilibrium validate the higher C-water values seen on the 25th. For this analysis, the measured C-water was compared to the predicted C-water based on the measured C-air and the published Kaw constants (measured Cw = measured Ca/ measured Kaw vs. predicted Cw= measured Ca/ published Kaw). This comparison is shown in Figures 2a and 2b. In these graphs, the water concentrations were calculated based on the daytime air samples, since for the 25th, these concentrations align better with predicted Kaw values.

The correlation between the increase in C-air values and the increase in C-water values suggest that during

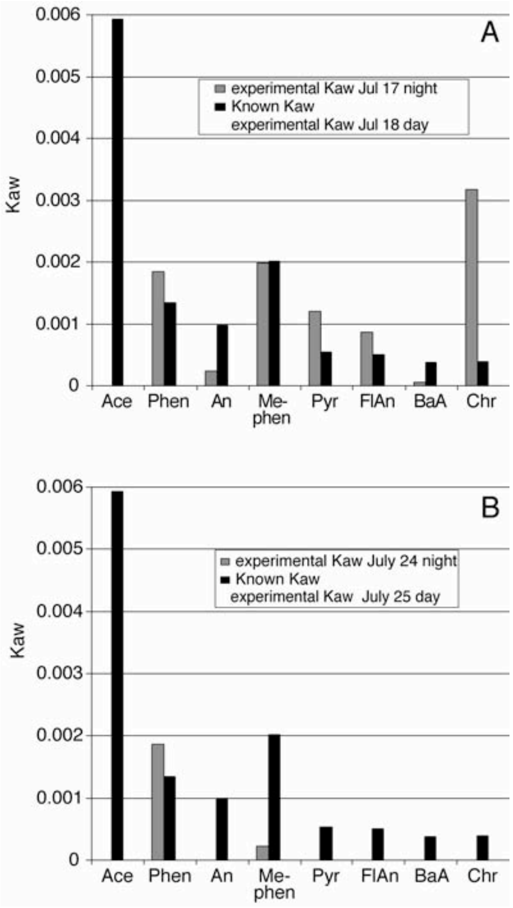

Figure 1. a) Measured Kaw (night and day) compared to published Kaw values for Jul 17-18. (Kaw values from Beyer 2001 and Bamford 1999). b) Measured Kaw (night and day) compared to published Kaw values Jul 24-25. Experimentally measured Kaw values from day and night compared to published values.

the morning of the 25th, PAHs were released into the air, followed by equilibration of these PAHs between the air and dissolved phase. At the time the water sample was taken, the PAHs had not yet equilibrated between the water phase and the particulate. This is indicated by the increase of C-water values compared to the week prior, but a lack of any change in the particulate levels. Consequentially, the Kpw values for the week of the 25th were lower than the coefficients from the 18th, and some lower than the octanol-water distribution constants as shown in Figure 3.

3.3 Kpw and Kow values

From the C-particulate and the C-water, the particulate-water distribution coefficient (Kpw) can be calculated and compared to the published Kow. Figure 3 shows these numbers with a one-to-one line to indicate how closely the experimentally determined values align with the published values.

The data show that the experimentally measured PAH distributions were above the literature Kow values.

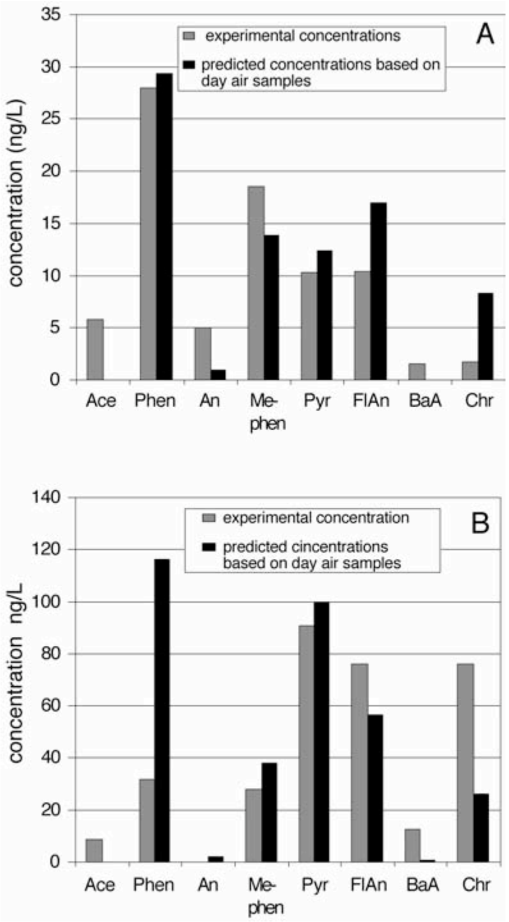

Figure 2. a) Measured compared to predicted concentrations of PAHs in Seawater July 18. Predicted concentrations were based on published Kaw values. b). Measured compared to predicted concentrations of PAHs in Seawater July 25. Predicted concentrations were based on published Kaw values.

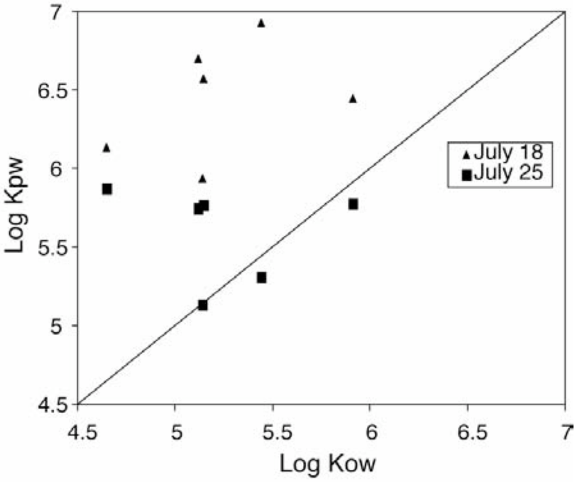

Figure 3. Experimental Kpw values compared to published Kow values.

Those that have lower Kpw values for both weeks, such as methylphenanthrene and chrysene, may establish equilibrium at lower rates than the other compounds because of their relatively bulky or heavy structures. Similar studies have also shown that while some heavier compounds have observed distribution coefficients that are lower than the predicted value, most compounds tend to have distribution coefficients above the predicted value (Sobek et *al*., 2004). Another possible explanation for this is the expected difference in mass between octanol and carbon, and complexity in comparability between the Kpw and the Kow.

3.4 Phytoplankton, Carbon, and TSS

The calculated particulate-water distribution coefficients are based on organic carbon found in the TSS which could correspond to the amount of phytoplankton. However, it seems equally possible that the measured distribution coefficient based on carbon accounts for more than the PAH association with phytoplankton. A more accurate proxy of phytoplankton concentration than an organic carbon measurement is the amount of chlorophyll-a in the water. Chlorophyll-a concentrations, including the compound detected in live and dead matter, are found in Table D.

The chlorophyll-a data can be used as a relative gauge to determine if changes in phytoplankton concentrations correspond to changes in PAH concentrations in the carbon. In this situation, the slight increase in the chlorophyll-a concentration does not correspond to any significant changes in the levels of PAHs detected in the carbon-containing particulate, yet a correlation should be detected in a larger and more accurate data set. Without more complex measurements of phytoplankton and PAH interactions, this study could not determine a direct way to relate the amount of chlorophyll-a found in the water to the amount of PAHs taken up by only phytoplankton. Future work could consider laboratory techniques and calculations to bridge this gap.

Additionally, the question of PAH association can be addressed by looking at the black carbon analysis to see if some of the organic carbon was black carbon, meaning that some of the PAHs detected in the particulate were actually associated with black carbon rather than phytoplankton. The results from this test indicate that less than 3.6 x 10^{-4} mg black carbon/mg TSS was detectable in the samples. This suggests that black carbon may not play an important role in the cycle of PAHs in the Narragansett Bay. However, more research is needed to verify these preliminary results.

Date	TSS mg/L	carbon mg/L	total Chl-a mg/L	%chl-a in TSS
18-Jul	5600	480	5.127	0.092
25-Jul	9800	420	6.652	0.067

Table D. Particulate Components. Data regarding the different ways to interpret the association of PAHs with the particulate.

It is conceivable that PAHs bind with something other than black carbon and carbon from living matter. This can be addressed with a plot of the distribution coefficients calculated from the PAHs in the total suspended solids (Ksw), compared to the Kow values corrected for the fraction of organic carbon (foc) as shown in Figure 4. The distribution constants based on the total suspended solids are higher than the comparable Kow values, confirming that there is something in the particulate phase, different from organic carbon, which does bind PAHs. Another study conducted on harbor waters and sediments showed similar results when the PAH concentrations were based on TSS, rather than living matter, as shown in Figure 5. However, in their study, the observed higher activity for various POPs was attributed to the presence of black carbon.

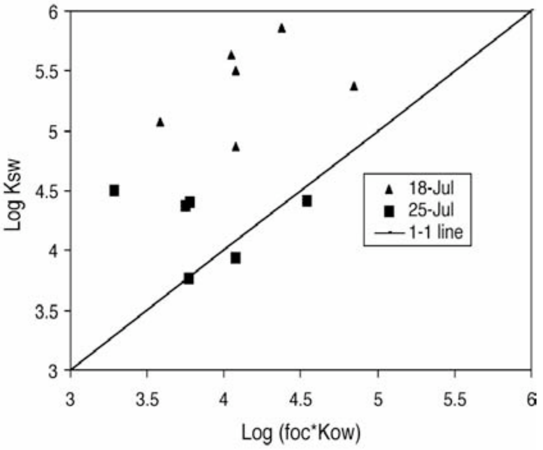

Figure 4. Measured Ksw values compared to published Kow values. The Kow values were adjusted to reflect the fraction of organic carbon (foc). High distribution coefficients relative to predicted values indicate that there may be PAHs in the particulate associated with non-living matter.

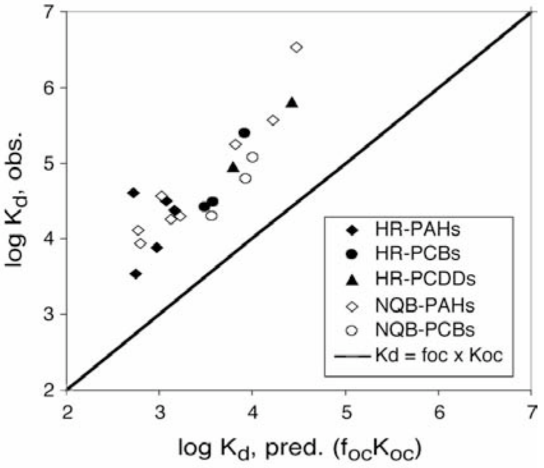

Figure 5. Measured Ksw values compared to published Kow values. The Ksw and Kow values have been adjusted to the conditions under which the study was done.

The results from the separate study also indicate that PAHs may associate with non-living particulate matter (Lohmann R., 2005). These figures indicate that or other inorganic matter that is found in the water column can absorb PAHs, with a matrix equally attractive as phytoplankton. More research in this area would lead to a better understanding of the future of POPs in our waters.

4. Conclusion

The results of this study provide a basis for future research on POPs in the Narragansett Bay. The proper procedure for a liquid extraction was determined, and a potential substitute method using pre-made cartridges was deemed inappropriate for this type of trace-analysis. The preliminary data also showed that the established procedure may have the desired sensitivity to detect changes in the PAH levels of different environmental phases as was seen on July 25th. Thus, continued sampling could lead to a record of the fluxes of POPs in the Narraggansett Bay in order to better understand their movement and fate in this urbanized body of water. It would be desirable to be able to monitor any increase in uptake of POPs by phytoplankton, the primary producers in marine food webs.

Additionally, it is clear that measuring the PAHs in the organic carbon is not an exact measure of the PAHs in phytoplankton. The chlorophyll-a count can be used as a proxy for phytoplankton concentration; more research needs to be conducted on relating this number to the amount of PAHs in carbon, and the possibility of directly measuring the PAHs in phytoplankton through experimentation. Also, it appears that black carbon may not have a significant effect on the cycle of PAHs, in the Narragansett Bay. However, this study and another suggest that there is something other than living matter in the particulate fraction which may provide an equally attractive matrix to PAHs as living matter.

Acknowledgments. We thank all involved staff and faculty at GSO and the NSF.

References

Bamford HA, Poster DL, Baker JE. 1999. Temperature Dependence of Henry's Law Constants of Thirteen Polycyclic Aromatic Hydrocarbons Between 4ºC and 31ºC. *Environmental Toxicology and Chemistry* 18:1905-1912.

Beyer A, Wania F, Gouin T, Mackay D, Matthies M. 2001. Selecting Internally Consistent Physiochemical Properties of Organic Compounds. *Environmental Toxicology and Chemistry* 21: 941-953.

Jones KC, de Voogt P. 1999. Persistent organic pollutants (POPs): state of the science. *Environmental Pollution* 100:209-221.

Lohmann R, MacFarlane JK, Gschwend PM. 2005. Importance of Black Carbon to Sorption of Native PAHs, PCBs and PCDDs in Boston and New York Harbor Sediments. *Environmental Science and Technology* 39:141-148.

Sobek A, Gustafsson O, Hajdu S, Larson, U. 2004. Particle-Water Partitioning of PCBs in the Photic Zone: a 25-month Study in the Open Baltic Sea. *Environmental Science and Technology* 38:1375-1382.

I.R. Cohen, E. Morgan. and R. Lohmann, Graduate School of Oceanography, University of Rhode Island, Narragansett, RI 02882. (ilanac@brandeis.edu, lohmann@gso.uri.edu)

The Effect of a Cape on Separation of a Western Boundary Current

Ben Diehl[1], Peter Cornillon, Vitalii Sheremet, and Joe Kuehl

Graduate School of Oceanography, University of Rhode Island, Narragansett, Rhode Island

Abstract. All of the major ocean basins have western boundary currents. These poleward flowing currents are narrow (~100km), fast (~1-2m/s) and located on the western side of the basin. All of these currents detach from the continental boundary at mid-latitudes. The Gulf Stream, a western boundary current, flows along the continental shelf from the Florida Straits to Cape Hatteras, North Carolina, where it turns east-northeast, flowing out into the Atlantic. The geography of the region following separation is complicated with the continental boundary also turning to the east some 100 km to the north of the point of separation. In this study, we investigate how geography such as Cape Hatteras effects separation of a physically modeled, steady-state, western boundary current. To create the current we use a circular tank with sloped bottom on a rotating table. Flow on the table is configured so as to give rise to an intense western boundary current. Experiments with currents covering a range of values are performed while the flow is recorded using one of two techniques. Particle Image Velocimetry allows one to obtain velocity fields at a fixed depth over a rectangular region in the tank. Dye studies allow visualization of several streamlines as a function of time. Using graphics obtained we show that the point of separation is more dependent on cape type barriers than on the rate of rotation of the tank, but neither are sensitive factors in creating this separation.

1. Introduction

Western Boundary Currents (WBCs), a feature present in every major ocean basin, have many traits in common. Besides having fast poleward flows (~1-2m/s) and being narrow relative to the size of their containing basin, all WBCs detach from the continental shelf in mid-latitudes. A notable example of this is the Gulf Stream. It follows the eastern coast of the United States from the Gulf of Mexico northward to Cape Hatteras, North Carolina. Upon reaching this point the current separates from the continental shelf and heads east-northeast into the Atlantic while the shoreline and shelf turn almost directly north.

Less than perfect understanding of exactly why separation occurs has puzzled many in geophysical fluid dynamics for a long time. The previous example of the Gulf Stream has led to many theories on how the presence and location of a cape affects the point of separation. In this investigation we have created a physical model of a WBC. Using this model we vary the position of a cape-like barrier in relation to the point where separation occurs without such a barrier.

We will describe the experimental setup used to create our WBC and the type of variations that were considered in Section 2 of this paper. Then we will explain the methods used to observe the current created in Section 3 before presenting the data, results and our conclusions in the final two sections.

2. Experimental Setup

The equipment used in this investigation breaks into three categories quite nicely. Firstly, the general apparatus includes everything needed to create a Western Boundary Current, all of which is used in the experiment, of which there are two main types: experiments with a rigid lid and those with a cape. In experimental runs done. The rest can be categorized by actuality cape experiments should be a subset of rigid lid experiments but are significant enough to be dealt with individually. After explaining the setup in detail we will go through the settings varied in each part.

To create a Western Boundary Current a cylindrical tank of 50 cm radius and with a height of 45 cm was centered on a rotating table. Figure 1 shows a topside view of this cylindrical tank. The left half is the active side, which is separated from the right half by a foam barrier. This active side has a false bottom with slope of 0.05 in the meridional direction so as to give east-west lines constant depth. This false bottom was marked with radial lines every 15 degrees and concentric half-

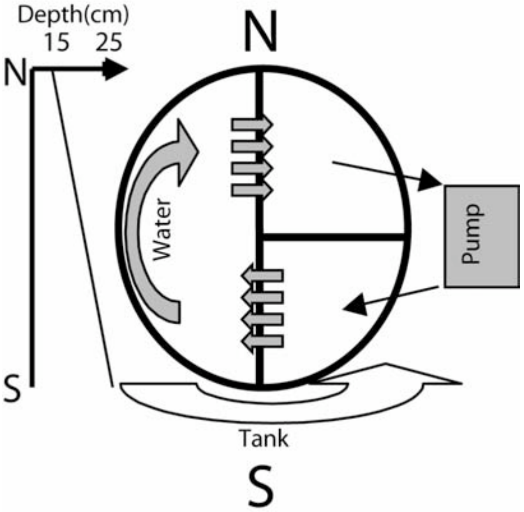

Figure 1. An overhead view of the general tank setup. Water flow is clockwise from south to north, with the tank rotating counterclockwise. On the left is a scale of water depth for the rigid lid model.

---

[1] Carleton College, Northfield, MN, 55057

circles with radii in 5 cm increments from 5 to 45 cm. Two additional pieces were made to cover the bottom: one of clear plastic to allow the lines to be visible and one painted black for runs where no excess reflection was wanted. The thickness of these two pieces was the same so that the depth of the fluid was constant regardless of which bottom was in place. After filling the tank with water, the initial current is created by pumping from the top-right (north-east) quadrant into the bottom-right (south-east) quadrant. The resulting difference in water level creates a pressure difference and thus forces water uniformly through the foam walls. With the addition of rotation to the water flow and known change in water height we create the β-effect needed for existence of a WBC and its eventual separation.

Once the general setup was found to be consistent between runs, a rigid lid was added. This was needed to eliminate the parabolic water surface that forms due to the rotation of the tank and its contained water. The lid is a thick sheet of plastic cut such that it fits closely when the lid is placed in the tank at an angle that mirrors the bottom, with a -0.05 slope. For these experiments the height of the lid above the sloping bottom was chosen such that the water was 20 cm deep along the east-west line bisecting the active region. Water is then added until the space between the lid and bottom is completely filled. This defines the 'rigid lid' setup. A number of experiments were run with this configuration.

A second set of experiments was undertaken following the addition of a "cape" to the rigid lid setup. The shape of the cape is a generalized form of what might be found in nature. The cape was designed to redirect the WBC off the boundary into the interior of the active area and then quickly turn away from this new path. The shape chosen fulfills such criteria as symmetrically as possible while maintaining a corner perpendicular to the level and filling the space between the bottom and lid. Figure 2 shows an overhead view of the cape. The height of the cape is determined by the position in which it is placed.

Combining these pieces of the setup gave three distinct types of experimental runs that were observed. The 'basic' setup included only what is needed to have a WBC and showed that not only was such a current being formed, but that there was a β-effect sufficient to force separation of the current. This setup was filled with 10 cm of water, measured along the same line as the rigid lid water level, creating a barotropic model. A 'standard' collection of settings was used starting with this setup. The standards used were a rotation rate, Ω, of 1 rad/sec, flow rate of pump, Q, of 60 mL/sec, and pump direction of poleward flow, as shown in Figure 1. This is defined as the poleward direction because the water becomes shallower as it moves clockwise around the tank, i.e., northward. For the 'basic' runs, flow was set at 20, 40, and 60 mL/sec for both poleward and equatorward directions with all other settings remaining at standard. The rigid lid was then added to create a completely uniform change in water height. The water height of 20 cm was chosen to allow for the doubling of the slope from the 'basic' setup. Runs done with this setup varied one setting from standard at a time. Rate of flow was set at 20, 40, 60, 80, and 120 mL/sec. Rotation rate was varied over three settings, 0.500, 1.000, and 1.945 rad/sec, recorded to precision of the rotating table. We will refer to these rates as 0.5, 1, and 2 rad/sec. Finally, using the rigid lid runs as a control, a cape was placed in one of two locations at -60° from N and -30° from N which was close to the normal separation point for our standard settings. Once the cape's location was set the three rotation rates were used to vary the position of the cape in relation to the normal separation point.

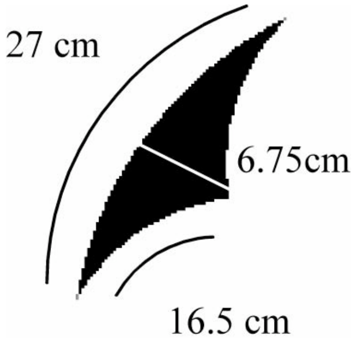

Figure 2. Shape and dimensions of the top of the cape piece.

3. Methods.

Having the WBC separate from the boundary is meaningless if there is no accurate way to track the path the current takes. We used two methods to visualize the current in all our experimental runs: dye and PIV. For the 'rigid lid' setup we also took advantage of a numerical model for comparison.

Dye experiments were run by using neutrally buoyant colored dye to trace long-term particle paths in the current. Holes were drilled in the lid to allow dye needles to be inserted 1 cm inside and parallel to the foam. These holes were 2 cm and 23.5 cm from the south edge. The needles were inserted to half the depth of the water at each location, roughly 12.5 cm and 11 cm, with the clear cover over the bottom, so that reference lines were visible. A camera was also attached to the table superstructure to view all or part of the active region. To start a run the pumps and table rotation were set at the rates indicated for the run and left to spin-up for about 20 minutes so that a steady state could be reached. After this time the dye was started at rates of 18 mL/hr for the 2cm needle, and 12 mL/hr for the 23.5 cm needle. After about 30 minutes, when both dye streams had reached the north foam, pictures were taken of the full path at a rate of no more than one per rotation. When the table is at steady state, the dye lines are assumed equivalent to streamlines for the current. After taking pictures the rotation rate or flow rate was changed and spin-up was again allowed to occur before taking images of the new run.

Particle Image Velocimetry (PIV) experiments allowed collection of instantaneous velocity data for a rectangular region of the tank. To do this we use LaVision software DaVis to couple a Nd:YAG laser with two cameras. The cameras were calibrated by taking normal images of a grid of evenly spaced references. DaVis then created a calibration file by comparing known grid spacing to that imaged. By seeding the tank with spherical grains having diameters of approximately ten microns, the laser light is reflected in all directions by these spheres and recorded by the cameras mounted vertically over the tank. This dependence on reflection required use of the black bottom cover. Pairs of images were taken separated by a short time, 90 milliseconds for these experiments. The DaVis software was then used to cross-correlate subregions of each image. A maximum in the cross-correlation occurs for a displacement of a subregion in one image relative to the corresponding subregion in the other image that corresponds to the mean displacement of particles in the subregion. The software applies this algorithm to all of the subregions covering the entire image thus generating a velocity field for the image pair. Image pairs were taken every tenth of a rotation for the slower two rotation rates. This rate did not allow for enough time to download images to the computer while spinning at the fastest rotation rate so a picture rate of 5 per rotation was used instead. During a normal run, the tank would be seeded and then immediately set to spin-up. After 15-20 minutes, sets of 30 to 100 image pairs were taken for analysis. A post-processing method was used to remove vectors, which were greater than 1.3 times the root-mean-square of its eight neighbors and iteratively to replace vectors that were less than 2.5 times the root-mean-square of its neighbors. This method also applied a mask, which removed all vectors in specified regions, outside and including the tank and cape boundary. This processing method results in a number of vector fields equal to the number of original image pairs. These vector fields were then averaged, by a root-mean-square process to produce a single vector field describing the flow of the tank for the region included in the image.

A numerical model, developed by Vitalii Sheremet was also used for comparison with the two visualization methods for runs with a rigid lid and no cape. This model was calibrated to the radius of the tank, slope of top and bottom, flow rate, and rotation rate used in the tank. It is a numerical solution to the Shallow Water Equations making use of cylindrical coordinates so as to accurately model the circular boundary of the physical tank. It calculates evolution of a stream function with trapezoidal time stepping until a steady state is achieved. The function was then plotted along contours to be mapped to observed data.

Once pictures, vectors, and plots had been obtained MATLAB was used extensively for analysis of each data type. Dye runs were first to be analyzed. The main process done was scaling the images to the physical tank. This was done using a least-squares fit to align a circle to one of the reference circles. Knowing the radius of the reference and the center position of the calculated circle the axes for the entire picture were easily scaled. To help in identification, many points along the dye lines were manually digitized and connected linearly to create digitized lines. If the dye was not a simple line but covered an area in a periodic manner, two lines were mapped to bound the area. PIV runs were also scaled before being plotted on top of the already scaled dye images. This process was very similar to the scaling of dye pictures. The normal picture used for calibration was used to fit a circle to the edge of the tank, since no references are visible through the black bottom cover. The edge of the reference grid was used to get the angle of the axes. This was possible because the grid was normally perpendicular to the north-south axis of the tank. Rotating the vectors by the calculated angle allowed the PIV and dye data to be compared directly. The numerical model data was easiest to compare as it was already of the correct scale and was just rotated to the angle found from a radial line on the dye pictures.

4. Results and Discussion

4.1. Rigid Lid

Data from the rigid lid method was used for two very different purposes. The first was a strict comparison of the methods of visualizing the current of the spun-up tank. The second was to show that rotation rate could be used as a substitute for many positions of the cape. To accomplish this, all that is needed is knowledge relating to how rotation rate changes the position of normal separation. With this, changes in rotation rate can be used instead of fine adjustment to cape position. The runs performed while varying rotation rate were also used as a standard to tell how separation varied in the cape runs.

All three methods were used to collect data for the standard settings, Q=60 mL/sec poleward and Ω=1 rad/sec. A dye run at these setting was found to give true streamlines, as there was no variation over a period of ten minutes, which includes over 100 full rotations. A picture from this run was used to compare both the PIV data averaged over a 100 image set, and the numerical model separately in Figure 3a and b, respectively. Figure 3c contains both PIV data and numerical data. The three forms visibly agree quite nicely. The numerical model is especially close and adds to the confidence in which we assert the average PIV data is of the WBC as we expect and includes much more information about instantaneous behavior than can be seen in either the numerical model or dye streams.

Since the methods we used were in agreement, we moved on to look at the different points at which the current would separate in relation to a cape. As noted above, changes rotation rate were used in place of changes in the location of the cape. Dye runs were done in the rigid lid setup at three different rotation rates, 0.5, 1, and 2 rad/sec, Figure 4a, b, and c, respectively. As expected, increasing the rotation rate moved the separation point farther north, to the right, while the increase in the β-effect pushed the boundary current farther west, toward the top. This result is similar to Munday and Marshall's (2005) finding that a β-effect

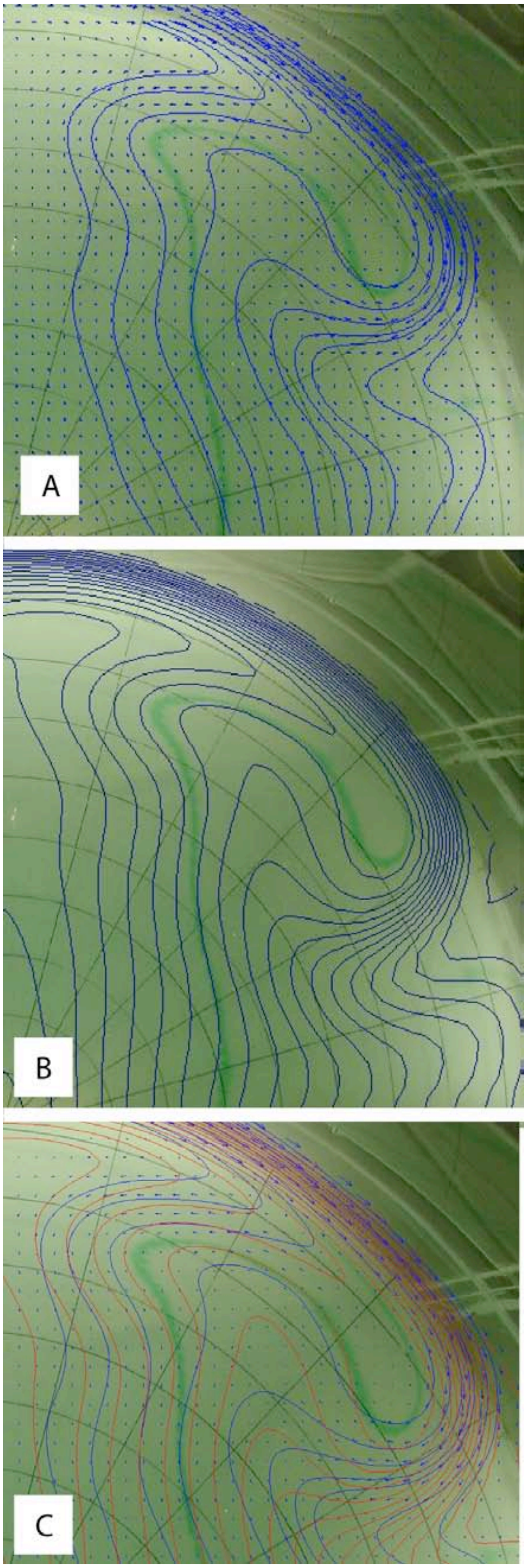

Figure 3. Comparison of PIV and Numerical Model on an image from a dye run at standard settings. A is PIV and dye; B is dye and model, while C is a combination of all three methods.

increase will delay flow separation in their numerical cape model. The trend found is very evident in 4d, where the outside lines of all three runs have been digitized and superimposed on top of the image from the 1 rad/sec run. In this Figure, 4d, the solid digitized line is from the outside of 4c, the heavy dashed line from 4b, and the finely dashed line from 4a. This change in separation point is slight but will allow a single placement of the cape to be tested against three different distances from natural separation points. For this reason these runs were also used to determine this natural point for comparison with later cape runs.

4.2. Cape Shaped Barriers

Taking full advantage of needing fewer cape placements, only two cape shaped barriers were made for the positions of 220° and 250° referred to as high and low placements. These positions were picked from the normal separation point of standard settings being at approximately 250°. The first cape was placed in the high position to observe how separation would be altered with a cape in the way of normal separation. This placement is shown in Figure 5a. Experimental runs were done at the three rotation rates and the lines digitized in the same manner as without a cape. Figure 5a shows the 0.5 rad/sec in green, 1 in blue, and 2 in red. It is clearly visible that the same trends observed without a cape apply to this situation. The difference being that the separation is from cape itself and not the tank boundary. It is very obvious that increasing the rotation rate still pushes the interior part of the WBC farther west while it can still be seen that the current gets farther north before separating. In the case of the 0.5 rad/sec run the outside line does not even reconnect to the tank boundary. We assume this is due to the fact it normally flows through this region away from the wall and not that the current has been forced extensively away from the boundary as real ocean examples might indicate. In order to test if early separation might be induced by the presence of a cape the placement of the second one was at the high position as pictured in Figure 5a. The results from the three rotation rates done with this high cape followed patterns observed in the other cape position. The flow separated later for higher rotation rates, again agreeing with the stated findings of Munday and Marshall (2005).

5. Conclusion

The classic Gulf Stream example of WBC separation stirs up many theories on what might affect where the separation point is located. The most inspiring is that of the nearby geographic feature Cape Hatteras. Taking this to heart, our physical model varied the distance between the point an uninterrupted Western Boundary Current separates and position of a cape-shaped barrier protruding into the interior of its circulation basin. As discussed the separation point in our barotropic model has some dependence on rotation rate and therefore β-effect, as one would expect. A dependence of similar significance exists with the

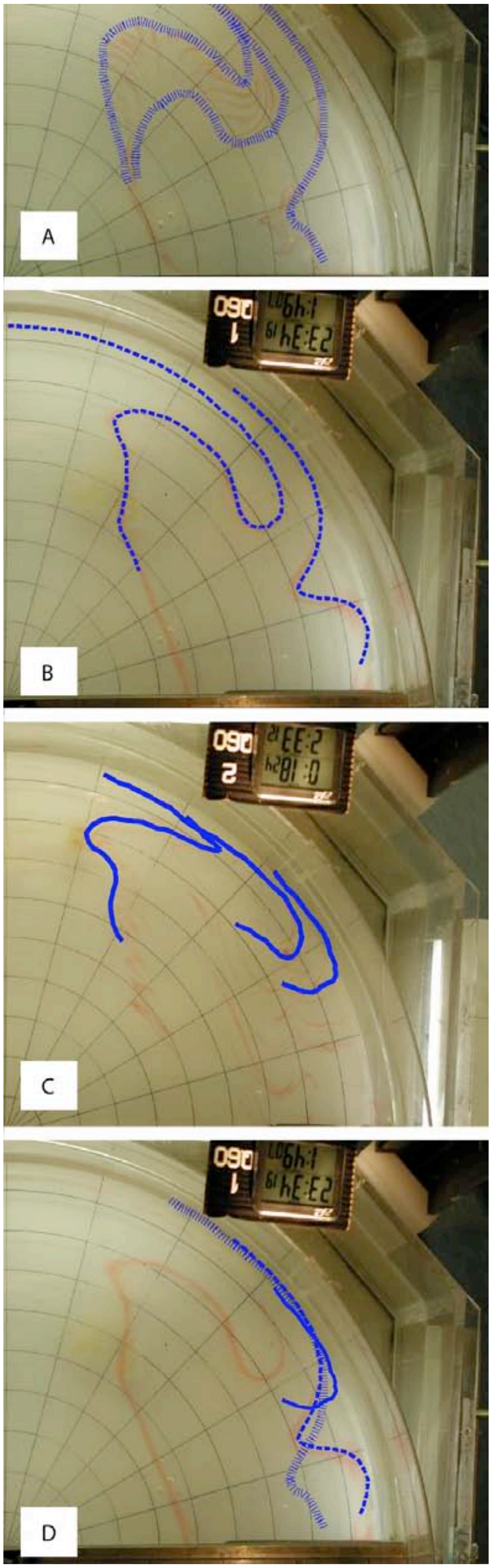

Figure 4. Movement in separation point due to change in rotation rate. A is from a dye run at 0.5 rad/sec, B is from a dye run at 1 rad/sec, and C is from a dye run at 2 rad/sec. D is the outside-digitized lines from A, B, and C appearing in the same style as they do individually.

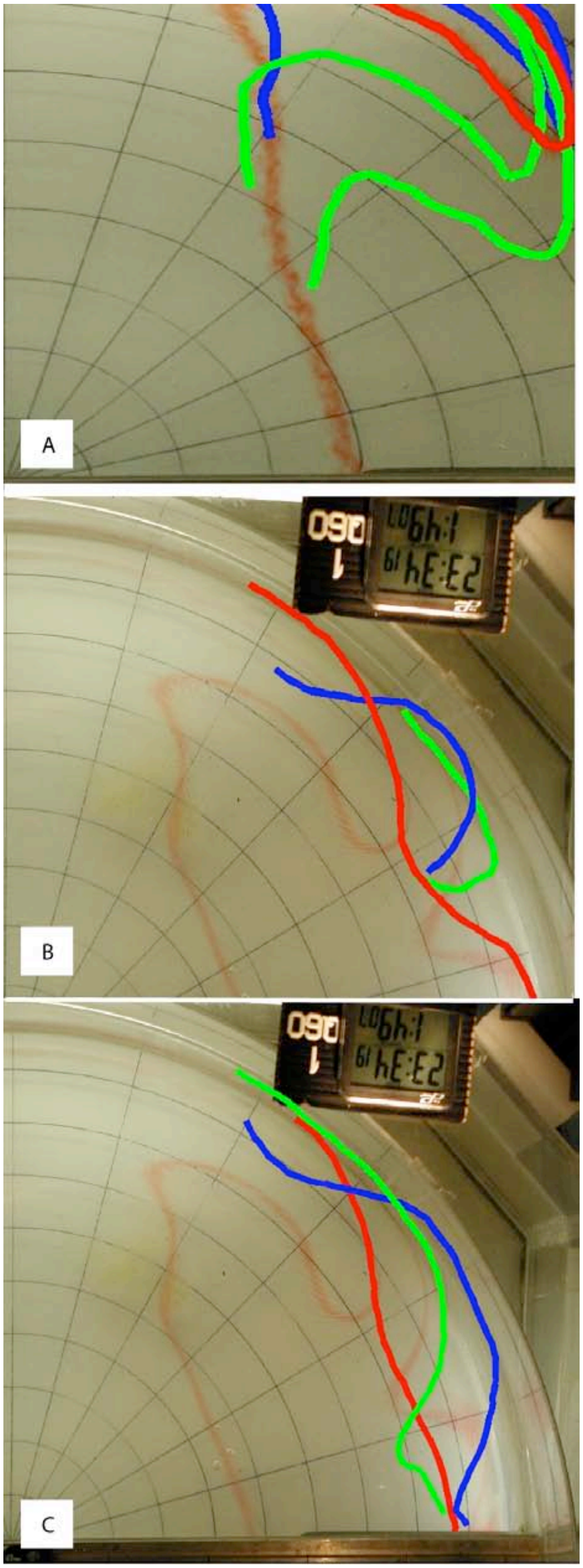

Figure 5. Results of cape runs. A is a composition of digitized lines from all three rotation rates: 0.5 (green), 1 (red), and 2 rad/sec (blue). B and C are the digitized versions of the outer dye lines from runs with no cape (green), a high cape (red), and a low cape (blue). B is from three runs at 2 rad/sec while C is from runs at 0.5 rad/sec.

presence of a cape. Figure 5b shows the three setups with a rotation rate of 1.945 rad/sec: the high cape is pictured in red, the low cape in blue and no cape in green. It can be observed from the change in adding the low cape, green to blue, the cape's presence does in fact force early separation. Figure 5c has the same color scheme for the three setups using a rotation rate of 0.500 rad/sec. Here the same observation can be made. Moving the cape from a low to high position also appears to force separation even earlier; although, the proximity of the foam barrier to the cape in the high position makes this uncertain. Combining the comparisons over all runs done shows effectively that there exists some level of dependence on the existence and position of a cape with regard to the location of separation. This dependence does not appear very significant as only the rotation rate of 0.5 rad/sec for the high cape has the possibility of forcing extended separation. Changing the position of the cape by 30° does have more effect on the point of separation than changing the rate of rotation by a factor of four. We must conclude that a cape's existence and position does effect the location of the point of separation for a Western Boundary Current more so than sole rotation rate, but neither creates significant change in the barotropic system.

Acknowledgements.. I would like to thank Rob Pockalny and Kim Carey for organizing and coordinating the 2005 SURFO program and to thank everyone else involved with making this program what it is.

References

Cushman-Roisin, B. 1994. Introduction to Geophysical Fluid Dynamics. Prentice Hall, N.J.

Kiss, A. E. 2002. Potential vorticity "crises", adverse pressure gradients, and western boundary current separation. *J. Mar. Res.*, **60**, 779-803.

Munday, D. and Marshall, D. 2005. On the Separation of a Barotropic Western Boundary Current from a Cape. *J. Phys. Oceanogr.*, In Press

---

P. Cornillon and V. Sheremet, Graduate School of Oceanography, University of Rhode Island, Narragansett, RI 02882. (pcornillon@gso.uri.edu, vsheremet@gso.uri.edu)

B. Diehl, Carleton College, Northfield, MN, 55057. (diehlb@carleton.edu)

Building a Coupled Biological-Physical Model of Narragansett Bay

Nicole M. La Sota,[1] Deanna Bergondo, and Chris Kincaid

Graduate School of Oceanography, University of Rhode Island, Narragansett, Rhode Island

Abstract. Hypoxia is a reoccurring problem in upper Narragansett Bay. Most of our understanding of hypoxic events comes from data sets that are either fixed sites or field surveys. By applying the hydrodynamic model, Regional Ocean Model System (ROMS) to Narragansett Bay, we can combine spatial and temporal data sets to better understand the system. This study will determine how well the Fasham based biological component of ROMS represents Narragansett Bay to further our understanding of the biology in the bay. The biological model was tested using data from the nutrient addition experiment conducted in the Marine Ecosystems Research Laboratory mesocosms from 1981-1983. The conditions of the nutrient addition experiments were replicated in a one-dimensional (vertical) numerical model and were compared to the observations. Numerical experiments were conducted to compare how changes in the parameterization of the biological terms differ. Experiments included default values, extremes, and a combination of the two. The default model showed great similarities with MERL temperature, phytoplankton, and zooplankton results and through the parameter comparison models, a mixed parameter model was run that improved these similar average trends. Changing the light attenuation by seawater, phytoplankton slope of the P-I curve, phytoplankton mortality rate, phytoplankton ammonia inhibition, light attenuation by chlorophyll, and Eppley temperature-limited growth parameter made significant differences to the model oxygen concentrations, while changing the zooplankton half-saturation constant for ingestion shifted the model oxygen, phytoplankton, and zooplankton concentrations, and changing the inverse half-saturation for phytoplankton ammonia uptake didn't change any of the model results. The results of this study found that the ROMS biological model can represent Narragansett Bay's average values for biological variables that include oxygen, phytoplankton, and zooplankton, but does not represent the seasonal values accurately.

1. Introduction

Hypoxia (low oxygen) is a reoccurring problem in the summer in upper Narragansett Bay (Bergondo et al. 2005, Deacutis et al. 2005, RIDEM 2003). Hypoxic events are the result of an overgrowth of phytoplankton caused by excess nutrients entering the bay by sewage and waste water treatment plant effluents, fertilizer runoff, input from the Rhode Island Sound, and erosion runoff. When the phytoplankton die and decompose, oxygen is consumed resulting in harmful hypoxic or anoxic (no oxygen) conditions. Environmental factors such as tides, rain, river flow, and wind can either help create or prevent hypoxic conditions. Rain and river flow increases stratification in a water column (Bergondo 2004). Oxygen gets trapped on the top of the stratified water column and the bottom waters could get hypoxic. High tides and wind help mix the water column and breaks down the stratification, allowing oxygen in the bottom waters (Bergondo 2004).

On August 20, 2003 an anoxic event occurred in Greenwich Bay that killed over one million fish, mostly menhaden, as well as over hundreds of crabs, shrimp, and eels (RIDEM 2003). Nutrient loads and significant rainstorms resulted in a massive phytoplankton bloom in the shallow bay, and a rapid decline in dissolved oxygen (RIDEM 2003). Greenwich Bay receives most of its nutrient loadings from the East Greenwich sewage treatment plant and from septic systems (RIDEM 2003). In response to this massive fish kill, sewage treatment facilities have been ordered to reduce the nitrogen output by 35% (RIDEM 2003).

Most of our understanding of hypoxic events comes from data sets that are either fixed sites or field surveys. Fixed sites include moored buoy monitoring which are continuous data but only from a certain point in the bay (Bergondo et al. 2005). Field surveys are data from different locations in the bay but only from a certain point in time (Deacutis et al. 2005). Computer models provide a way to combine spatially detailed data and temporally detailed data to provide better understanding of a system in space and time. The public domain hydrodynamic model, Regional Ocean Model System (ROMS) developed at Rutgers University and UCLA (Shchepetkin and McWilliams 1998; 2003; 2005), has been applied to Narragansett Bay (Bergondo 2004) to understand circulation in the Bay. This study will determine how well the Fasham based biological component (Fasham et al. 1990) of ROMS represents the biology of Narragansett Bay.

This study uses the ROMS biological model coupled with a simplified one dimensional physical model to model nutrient addition experiments conducted in the Marine Ecosystems Research Laboratory (MERL) mesocosms at the Graduate School of Oceanography from 1981 to 1983. The MERL experiments were chosen because they dealt with the effects of different nutrient additions on Narragansett Bay and had a lot of data taken that was readily available. The ROMS biological model will then be incorporated in the Narragansett Bay model to increase our understanding of the biological and physical factors that cause hypoxic events, track where these hypoxic waters travel throughout the bay, and to determine the affects of the reduced nitrogen output of sewage treatment plants on hypoxic events. The results of this study found that the ROMS biological model can represent Narragansett

---

[1] Now at Rutgers University, New Brunswick, NJ

Bay's average values for biological variables that include oxygen, phytoplankton, and zooplankton, but does not represent the seasonal values accurately.

2. Methods

2.1. MERL nutrient addition experiments 1981-1983

The MERL experiments try to mimic the bay in terms of mixing, temperature, and turnover time, then added a different amount of nutrients into the mesocosms for 28 months. The MERL experiments were conducted from June 1981 through September 1983 using nine mesocosms (Figure 1) (Oviatt et al. 1986). Six mesocosms were treated with inorganic nitrogen daily in a logarithmic series, 1X (2.88mM N m^2 d^{-1}), 2X, 4X, 8X, 16X, and 32X the nitrogen found in the Providence River sewage effluents (Oviatt et al. 1986). Three mesocosms were treated as controls and did not receive nutrient addition (Oviatt et al. 1986). The 32X nutrient addition mesocosm conditions were used for comparison with the ROMS model. The water temperature in the mesocosm was maintained within 2°C of ambient Narragansett Bay water from the GSO dock in the west passage of Narragansett Bay (Oviatt et al. 1986). The water was mixed using a vertical plunger for 2h out of every 6h to mimic tidal currents (Oviatt et al. 1986). During the period the mixing plungers were operating, 120 L of bay water was pumped from the GSO dock for 12 min periods, 4 times daily (Oviatt et al. 1986). The nutrients were added to the mesocosm once a day during the morning mixing period. Bay water inputs resulted in an average turnover time of 27 days (Oviatt et al. 1986).

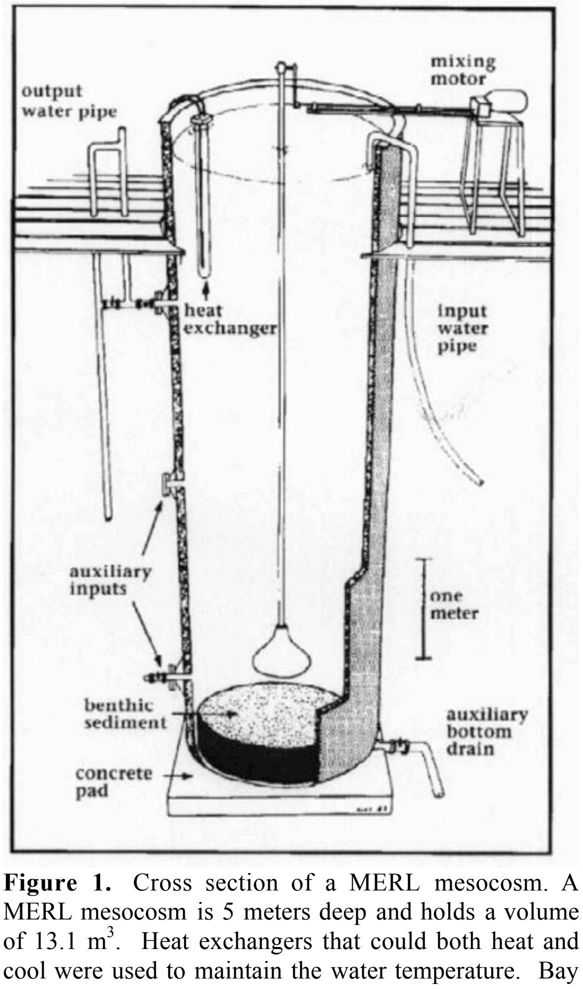

Figure 1. Cross section of a MERL mesocosm. A MERL mesocosm is 5 meters deep and holds a volume of 13.1 m^3. Heat exchangers that could both heat and cool were used to maintain the water temperature. Bay water was pumped in through the input pipe in a pulsed flow of 10 l min^{-1} for a 12 min period every 6 h. Mixing was done using a vertical plunger, 50 cm diameter, 2 h on and 4 h off (Oviatt et al. 1986).

The MERL experiments were chosen over Narragansett Bay as a starting point to apply the biological model because these controlled environments had simplified physics and extensively monitored oxygen, phytoplankton, zooplankton and nutrient concentrations. Consecutive dawn-dusk-dawn oxygen concentration measurements were taken weekly to estimate daily production and night respiration (Oviatt et al. 1986). Biomass of phytoplankton was sampled weekly during the mixing cycle by chlorophyll a analysis (Oviatt et al. 1986). Dissolved inorganic nutrients and zooplankton biomass were also sampled weekly during the mixing cycle (Oviatt et al. 1986).

2.2. ROMS

The ROMS model matched the physics of the MERL mesocosms in terms of boundary conditions, mixing, temperature, nutrient input, and sea water input. The ROMS model ran for one year from June 8th 1981 through June 7th 1982. The model was a square tank with northern and southern walls and eastern and western open boundaries that allowed water to flow in and out (Figure 2). The sea water flowed into the tank continuously through 6 small rivers on the western boundary at 0.0033 m^3 s^{-1} each, for a total of 0.02 m^3 s^{-1} combined flow in the entire tank. The flow resulted in an average turnover time of 27 days. A concentration of 18.25 mM m^{-3} of ammonia was added to the tank through the six rivers continuously. Mixing was done 4

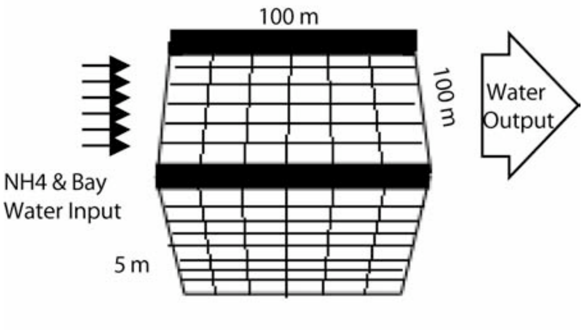

Figure 2. The ROMS model of a MERL mesocosm. A square tank with an area of 10,000 m^2 and a height of 5 m. There are two walls on the north and south side of the tank that allows the water to flow in and out of the sides. The nutrients and fresh sea water were added through 6 small rivers that flowed in continuously at each grid along the west side of the tank.

times a day at 1.0 x 10^{-4} m^2 s^{-1} using a sine curve to represent natural tidal mixing. The solar radiation was forced using real data from June 8th 1981 through June 7th 1982 obtained from Eppley Laboratory in Newport, Rhode Island. The air temperature was manipulated to maintain the water temperature within 5C of the MERL water temperature. The initial conditions of the model are shown in Table 1.

The ROMS biological model was based on Fasham's simple biological model (Figure 3). The variables of the model include nitrate, ammonia, oxygen, phytoplankton, zooplankton, chlorophyll, detritus (large and small), and bacteria. For this study, the parameters for phytoplankton and zooplankton were focused on. The equation for phytoplankton is:

$$\frac{\delta P}{\delta t} = \left(1-\gamma\right)\sigma\left(t, M, N_m, N_r\right)P - G - \mu P - \frac{\left(m + h\left(t\right)\right)P}{M} \qquad (1)$$

Where γ is the amount of phytoplankton exuded as DON, σ is phytoplankton specific growth rate as a function of temperature limited growth rate, the initial slope of phytoplankton P-I curve, mixed layer depth, phytoplankton ammonia uptake rate and inhibition, and phytoplankton nitrate uptake rate, G is the grazing rate of zooplankton, μ is phytoplankton mortality rate, and M is the mixed layer depth. The equation for zooplankton is:

$$\frac{\delta Z}{\delta t} = \beta^p G^p + \beta^b G^b + \beta^d G^d - \mu^e Z - \mu^m Z - \frac{h\left(t\right)Z}{M} \qquad (2)$$

Where β is zooplankton grazing efficiencies for phytoplankton, bacteria, and detritus, G is zooplankton grazing rates, μ_e is zooplankton excretion rate, μ_m zooplankton mortality rate, and M is the mixed layer depth. The parameters that were experimented with in this study are shown in Table 2, along with the range and default values. The model was run with all of the default parameters (Table 2). An additional 16 runs were conducted using the extremes of the parameter ranges (Table 2), one parameter change per model run with the rest of the parameters set to the default value. Finally, a run was conducted with a mixture of parameters based on results of the previous 16 experiments.

3. Results/Discussion

The results for the model with all of the default parameters set (Figure 4), 16 models that compared different parameters (Table 3), and a final combination model of mixed parameters are presented here. The default model showed great similarities with MERL temperature, phytoplankton, and zooplankton results and through the parameter comparison models, a mixed parameter model was run that improved these similar average trends.

Variable	Initial condition
NO3 (mM m^{-3})	0.87
NH4 (mM m^{-3})	38.13
Phytoplankton (mM N m^{-3})	0.72
Zooplankton (mM N m^{-3})	0.22
Chlorophyll (mg m^{-3})	85.2
Oxygen (mM m^{-3})	266.89
Temperature (°C)	17.5
Salinity (PSU)	32

Table 1. Initial Conditions of model.

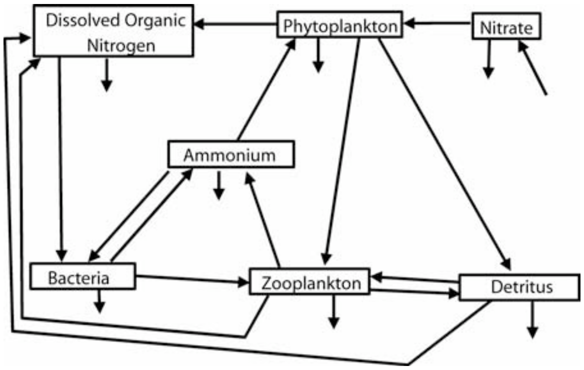

Figure 3. Fasham's simple biological model. The model is nitrogen-based of mixed layer plankton and nitrogen cycling showing the variables and the modeled nitrogen flows among variables (Fasham et al. 1990).

Parameter	Default Values	Tested Values
Light attenuation due to seawater (1/m)	0.04	0.4, 0.8
Light attenuation by chlorophyll (1/(mg CHL * m^2))	0.02486	0.02, 0.04
Eppley temperature-limited growth parameter	0.5	0.25, 1
Inverse half-saturation for phytoplankton NH4 uptake (1/(millimole N * m^3))	2	1.33, 4
Zooplankton half-saturation constant for ingestion (1/(millimole N * m^3)	2	0.5, 1
Phytoplankton, NH4 inhibition parameter (1/(millimole N))	1.5	0.75, 3
Phytoplankton, initial slope of P-I curve (mg C/(mg Chl * Watts* m^2*day))	0.0175	0.025, 0.05
Phytoplankton mortality rate (1/day)	0.055	0.072, 0.11

Table 2. Parameter comparison values.

Values	Oxygen	Phytoplankton	Zooplankton
0.04	Default		
0.4	Lower	Lower	Lower
0.8	Lower	Lower	Lower
0.02	Higher	Higher/Left	Higher/Left
0.02486	Default		
0.04	Lower	Right	Right
0.25	Lower	Lower	Lower
0.5	Default		
1	Higher	Higher	Higher
1.33	None	None	None
2	Default		
4	None	None	None
0.5	Lower	Lower	Lower
1	Higher	Higher/Left	Higher/Left
2	Default		
0.75	Higher	Higher/Left	Higher/Left
1.5	Default		
3	Higher	none	None
0.0175	Default		
0.025	Lower	Lower/Right	Lower/Right
0.05	Higher	Higher/Right	Higher/Right
0.055	Default		
0.072	Lower	None	None
0.11	Lower	Higher	Higher

Table 3. Parameters for model runs and changes in predicted plankton abundance.

3.1 Default Model

Comparison of the default model to the MERL results showed that the model agreed well with the temperature data (Figure 4a). The model results for the water temperature matched MERL with only a difference of less than 5°C from around weeks 25 through 44. This shows the manipulation of the air temperature was a success to maintain the model water temperature within 5°C of MERL water temperature.

The default model results for ammonia exceeded the concentrations found in the MERL experiments and lacked the detail shown in the data (Figure 4b). The model results for ammonia increased until it reached a concentration of approximately 500 mM m^{-3}, and remained significantly higher than the MERL data. The model definitely added ammonia to the tank, but there was no evidence that the ammonia was affected by any other processes. This is most likely due to the excessive amount of ammonia that was added into the 32X mesocosm.

The results for the model oxygen remained higher than the MERL oxygen and lacked all of the detail of the actual data (Figure 4c). The model oxygen grew more rapidly during the summer (weeks 0 through 20 and weeks 40 through 60) than winter (weeks 20

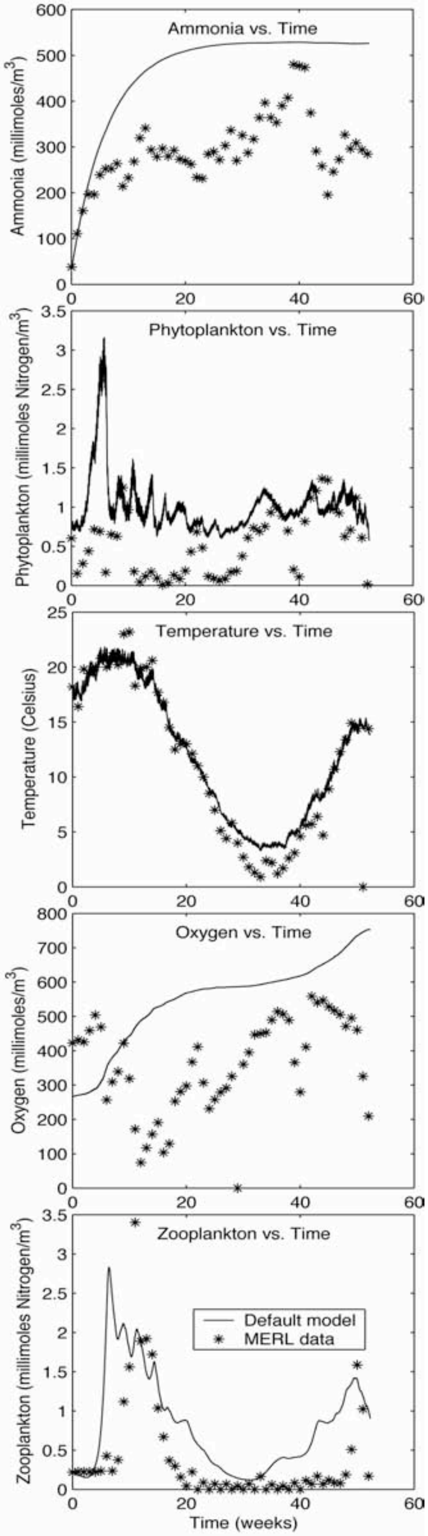

Figure 4. Model run with all of the default parameters set compared to MERL data. The model was run for a year from June 8th 1981 through June 7th 1982 representing MERL 32X nutrient addition mesocosm. The default model is represented by a solid line and the MERL data is represented with star points. Default model (**a.**) temperature, (**b.**) ammonia, (**c.**) oxygen, (**d.**) phytoplankton, and (**e.**) zooplankton results compared to MERL data.

through 40), which is an indication of primary production.

The model phytoplankton was at a higher range than MERL phytoplankton but included a lot of detail (Figure 4d). There is a correlation between the model oxygen and the model phytoplankton results. The time period the oxygen increased more rapidly was the time period phytoplankton were at a greater concentration and when phytoplankton were growing less is when the oxygen grew less rapidly (Figure 4c and d).

The model zooplankton showed great similarities to the MERL zooplankton and have obvious relationships with the phytoplankton results (Figure 4e). Two peaks were seen at the beginning and the end of the model year in the data and model output. Both records also leveled out in the middle of the year run. There were strong correlations between the model phytoplankton and zooplankton results. The zooplankton grew rapidly after the phytoplankton peaked and phytoplankton dropped in concentration with zooplankton following shortly after (Figure 4d and e). These correlations show the model makes sense in the relationships between the variables.

3.2. Parameter Comparison

A series of model experiments were done to document sensitivity of the results to the parameter ranges. Changing the light attenuation by seawater, phytoplankton slope of the P-I curve, phytoplankton mortality rate, phytoplankton ammonia inhibition, light attenuation by chlorophyll, and Eppley temperature-limited growth parameter made significant differences to the model oxygen concentrations, while changing the zooplankton half-saturation constant for ingestion shifted the model oxygen, phytoplankton, and zooplankton concentrations, and changing the inverse half-saturation for phytoplankton ammonia uptake didn't change any of the model results. There was no effect on the ammonia concentration throughout all of the parameter comparison runs. The 16 parameter comparison model results are summarized in Table 3.

As the light attenuation due to seawater (AttSW) was raised, it lowered the concentrations of oxygen (Figure 5a), phytoplankton (Figure 5b), and zooplankton (Figure 5c). This was expected since raising the AttSW means less light is getting through the water column, preventing phytoplankton growth. The less phytoplankton growth, the less oxygen produced. The less phytoplankton there are for zooplankton to feed on limits zooplankton growth.

The phytoplankton slope of the P-I curve (PhyIS) only had a notable affect on oxygen when it was changed (Figure 6). The higher PhyIS of 0.05 mg C mg Chl^{-1} $Watts^{-1}$ m^{-2} resulted in a higher oxygen concentration, followed by a oxygen concentration in the middle at 0.0175 mg C mg Chl^{-1} $Watts^{-1}$ m^{-2}, and a lower oxygen concentration at the PhyIS of 0.025 mg Chl^{-1} $Watts^{-1}$ m^{-2} (Figure 6a). The phytoplankton and zooplankton trends were generally the same for all the PhyIS values tested (Figure 6b and 6c).

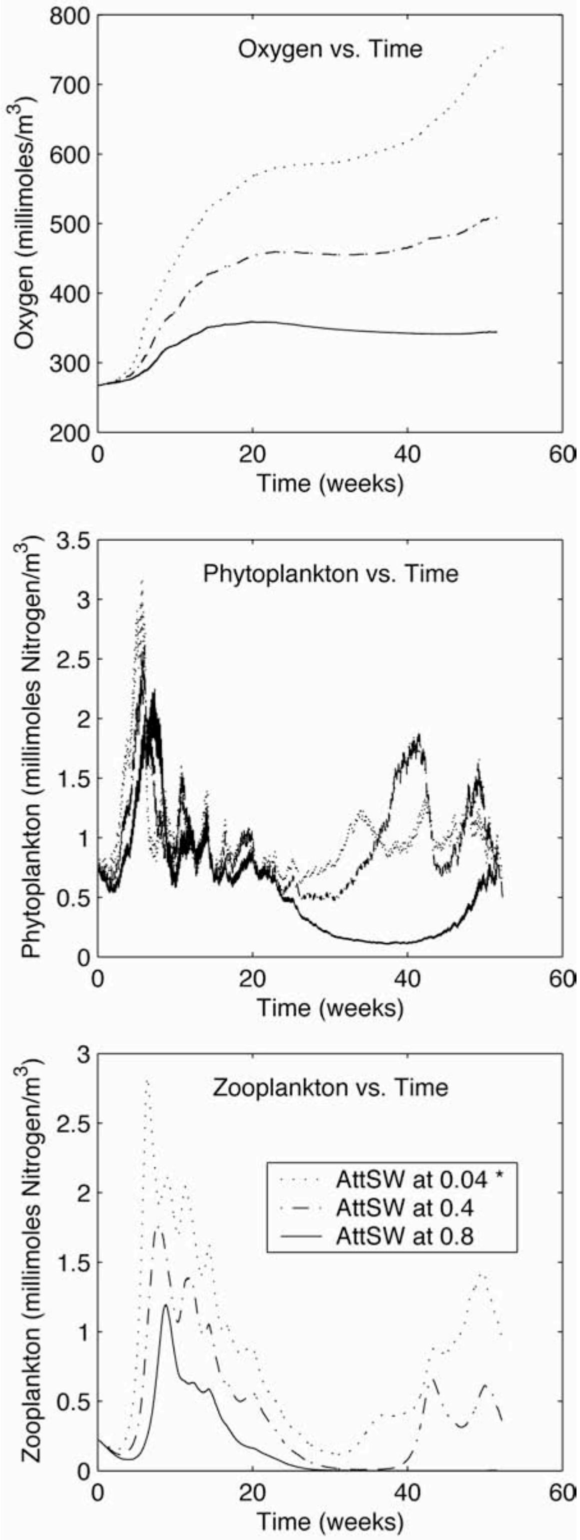

Figure 5. Comparison of three values for the light attenuation due to seawater (AttSW) parameter. The three values were the default value (*) of 0.04 m^{-1}, 0.4 m^{-1}, and 0.8 m^{-1}. The effects of the parameter changes were compared using the (**a.**) oxygen, (**b.**) phytoplankton, and (**c.**) zooplankton model results.

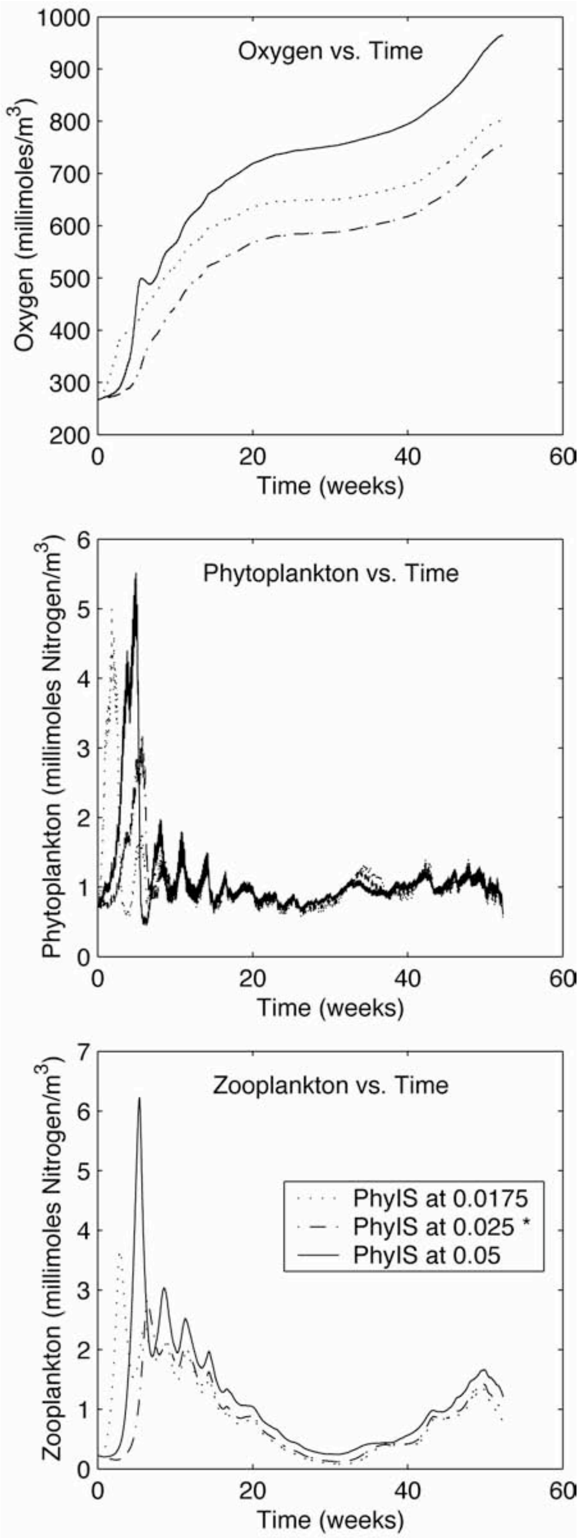

Figure 6. Comparison of three values for the phytoplankton initial slope of P-I curve (PhyIS) parameter. The three values were 0.0175 mg C mg Chl^{-1} $Watts^{-1}$ m^{-2}, the default value (*) 0.025 mg C mg Chl^{-1} $Watts^{-1}$ m^{-2}, and 0.05 mg C mg Chl^{-1} $Watts^{-1}$ m^{-2}. The effects of the parameter changes were compared using the (**a.**) oxygen, (**b.**) phytoplankton, and (**c.**) zooplankton model results.

As the phytoplankton mortality rate (μ) was raised, the oxygen concentration was lowered after 20 weeks (Figure 7a). The phytoplankton and zooplankton growth had the same general trends except for after 20 weeks with the μ of 0.072 day^{-1}, where it dipped lower than the other parameter model runs (Figure 7b and 7c). This is supported by the zooplankton reaching zero a little after 20 weeks, which allowed the phytoplankton to peak at 40 weeks.

The phytoplankton ammonia inhibition parameter (PhyIP) set at 0.75 mM N^{-1} had higher oxygen concentration results than the default and higher values (Figure 8a). This could be explained by the higher peak PhyIP made for the phytoplankton growth during the 0 through 5th weeks of the year run (Figure 8b). Other than those differences, all of the changes to the PhyIP parameter resulted with the same general trends (Figure 8c).

Raising light attenuation by chlorophyll (AttChl) resulted in a lower oxygen concentration (Figure 9a). The first peak of phytoplankton growth and zooplankton growth during 0 to 10 weeks was lowered substantially from the light attenuation of 0.02 mg Chl^{-1} m^{-2} to 0.02486 mg Chl^{-1} m^{-2} (Figure 9b and 9c). The first peaks of zooplankton and phytoplankton growth were also shifted to the right as the AttChl was raised. These results show that the more self shading by phytoplankton there is, the less oxygen is produced, and phytoplankton grows less. The phytoplankton and zooplankton growth after 10 weeks were the same for all of the AttChl values. This could be due to the amount of phytoplankton being too low to be influenced by self shading.

An increase in the Eppley temperature-limited growth parameter (Vp0) produced higher concentrations of oxygen, phytoplankton, and zooplankton (Figure 10). As the parameter was raised, it also created more peaks and detail to the phytoplankton and zooplankton growth. The Vp0 is simply a multiplier for the Eppley temperature limited growth rate (Vp), which makes these results make sense (Equation 3).

$$Vp = Vp0 * 0.59 * 1.066 * \text{temperature} \tag{3}$$

The results for the zooplankton half-saturation constant for ingestion (G) not only affected zooplankton but controlled phytoplankton as well. The G at 0.5 day^{-1} produced the lowest oxygen concentration, 1.0 day^{-1} had the highest oxygen concentration, and at 2.0 day^{-1} had an oxygen concentration in the middle (Figure 11a). As the zooplankton half-saturation constant for ingestion was raised, the phytoplankton and zooplankton general trends were raised (Figure 11b and 11c).

Changing the inverse half-saturation for phytoplankton NH_4 uptake (K_NH4) did not effect the oxygen, phytoplankton, or zooplankton concentrations (Figure 12). One possible reason for this is the amount of ammonia that was put into the tank was too much for this parameter to have an effect on the results.

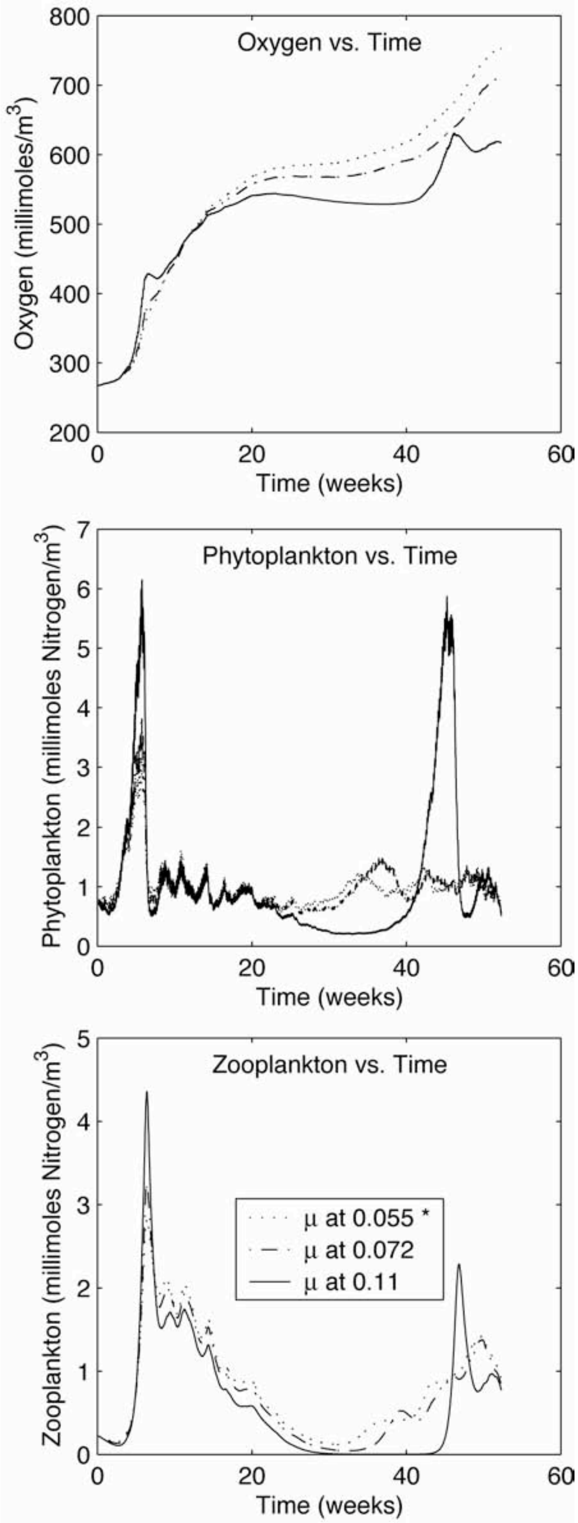

Figure 7. Comparison of three values for the phytoplankton mortality rate (μ) parameter. The three values were the default value (*) 0.055 day^{-1}, 0.072 day^{-1}, and 0.11 day^{-1}. The effects of the parameter changes were compared using the (**a.**) oxygen, (**b.**) phytoplankton, and (**c.**) zooplankton model results.

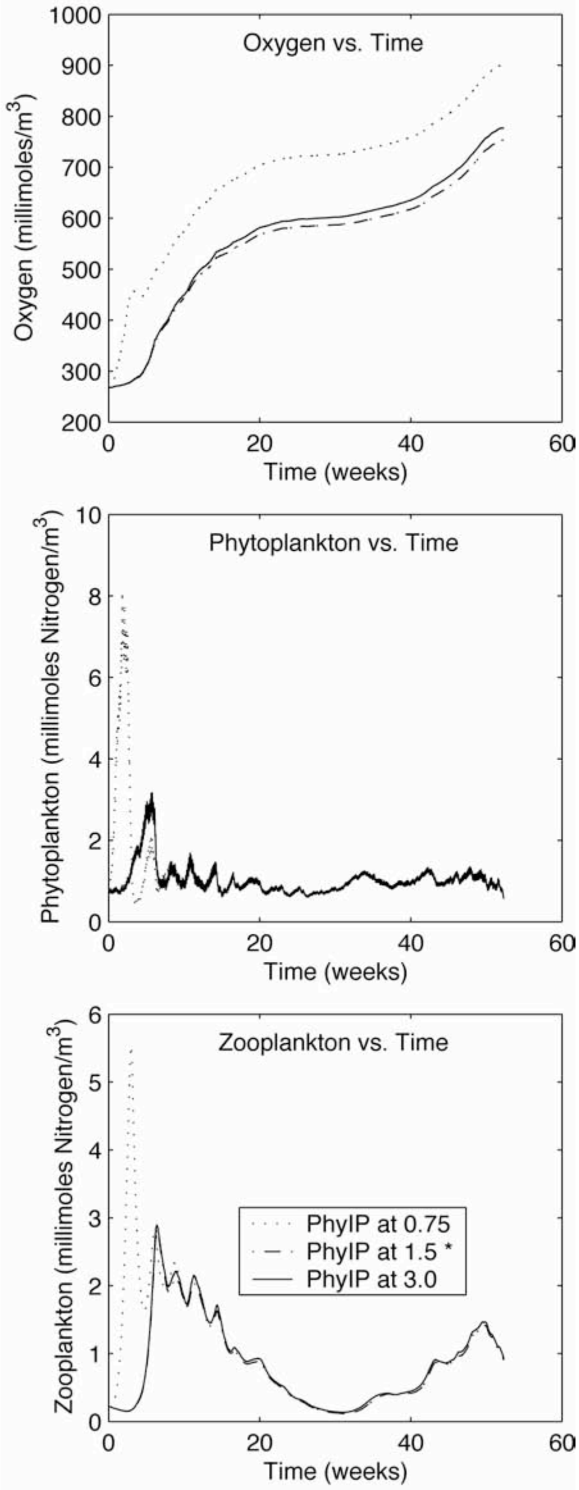

Figure 8. Comparison of three values for the phytoplankton ammonia inhibition (PhyIP) parameter. The three values were 0.75 mM N^{-1}, the default value (*) 1.5 mM N^{-1}, and 3.0 mM N^{-1}. The effects of the parameter changes were compared using the (**a.**) oxygen, (**b.**) phytoplankton, and (**c.**) zooplankton model results.

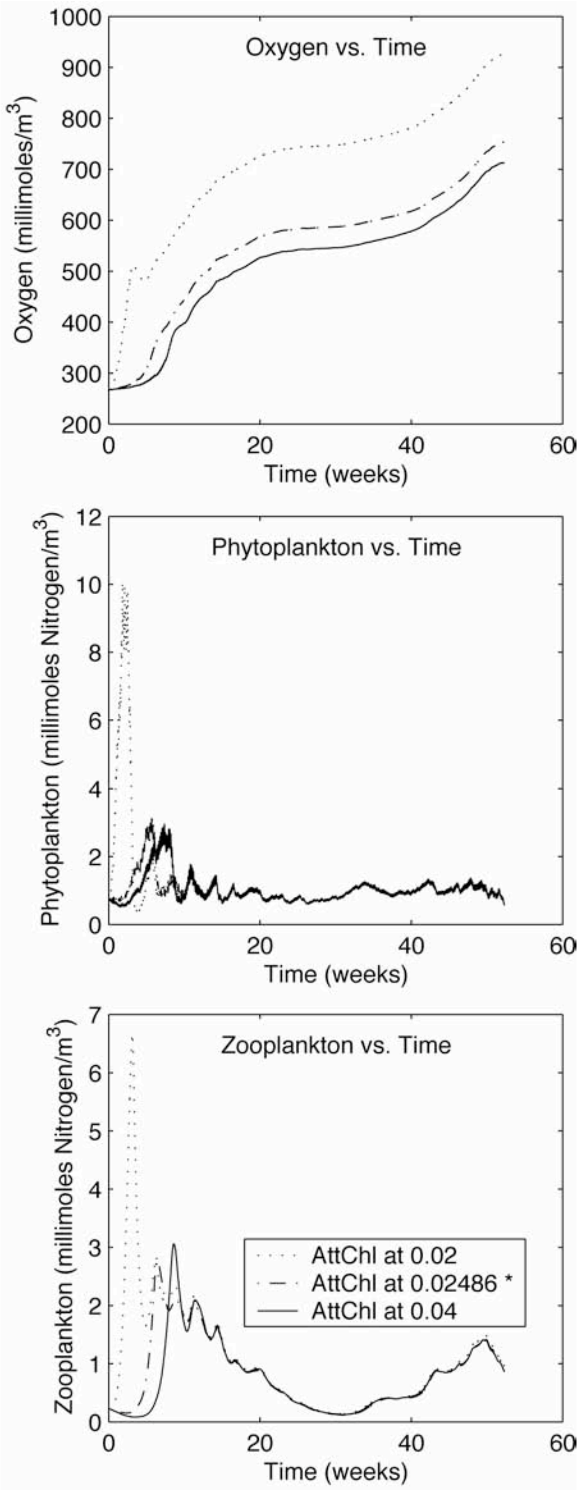

Figure 9. Comparison of three values for the light attenuation by chlorophyll (AttChl) parameter. The three values were 0.02 mg Chl^{-1} m^{-2}, the default value (*) 0.02486 mg Chl^{-1} m^{-2}, and 0.04 mg Chl^{-1} m^{-2}. The effects of the parameter changes were compared using the (**a**.) oxygen, (**b**.) phytoplankton, and (**c.**) zooplankton model results.

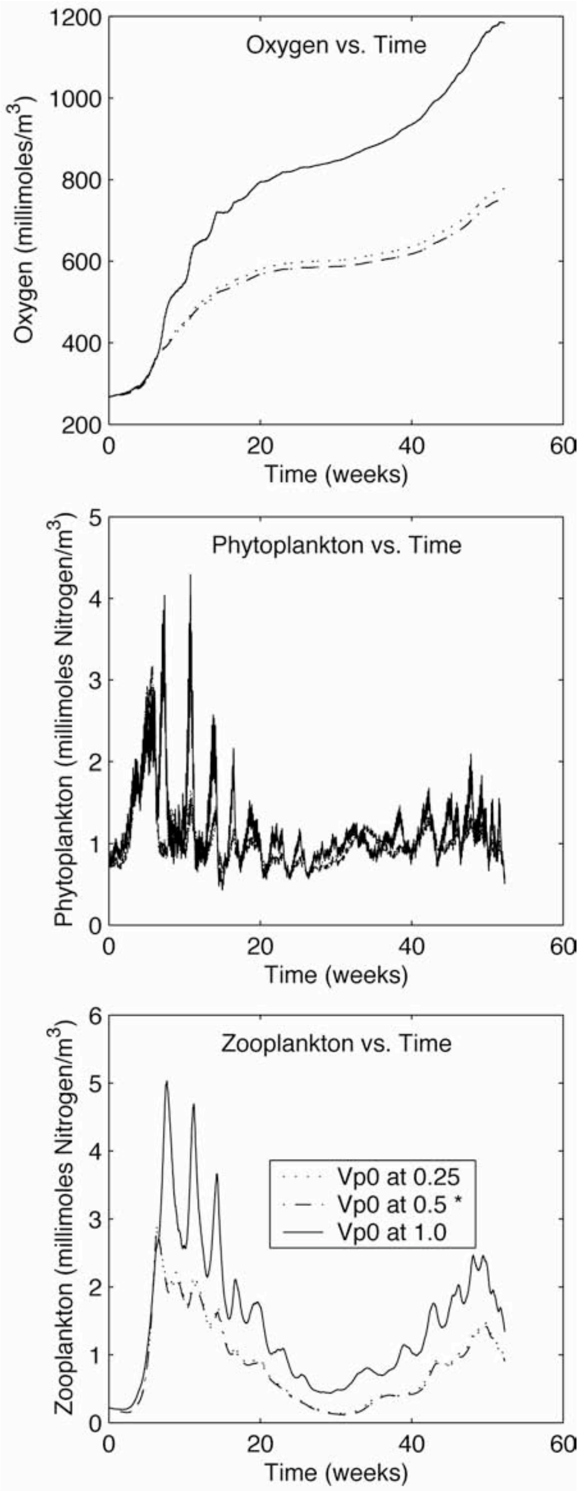

Figure 10. Comparison of three values for the Eppley temperature-limited growth (Vp0) parameter. The three values were 0.25, the default value (*) 0.5, and 1. The effects of the parameter changes were compared using the (**a**.) oxygen, (**b**.) phytoplankton, and (**c.**) zooplankton model results.

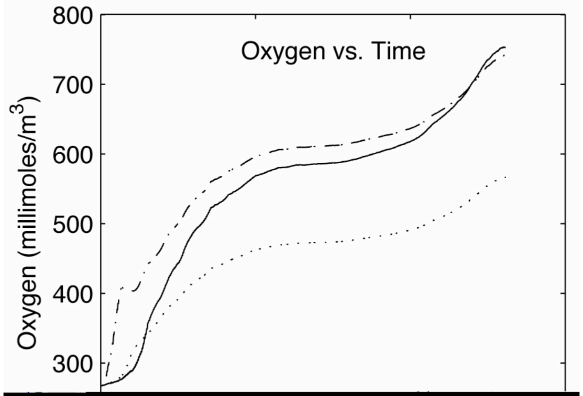

[redacted]

Figure 11. Comparison of three values for zooplankton half-saturation constant for ingestion (G) parameter. The three values were 0.5 day^{-1}, 1.0 day^{-1}, and the default value (*) 2.0 day^{-1}. The effects of the parameter changes were compared using the (**a.**) oxygen, (**b.**) phytoplankton, and (**c.**) zooplankton model results.

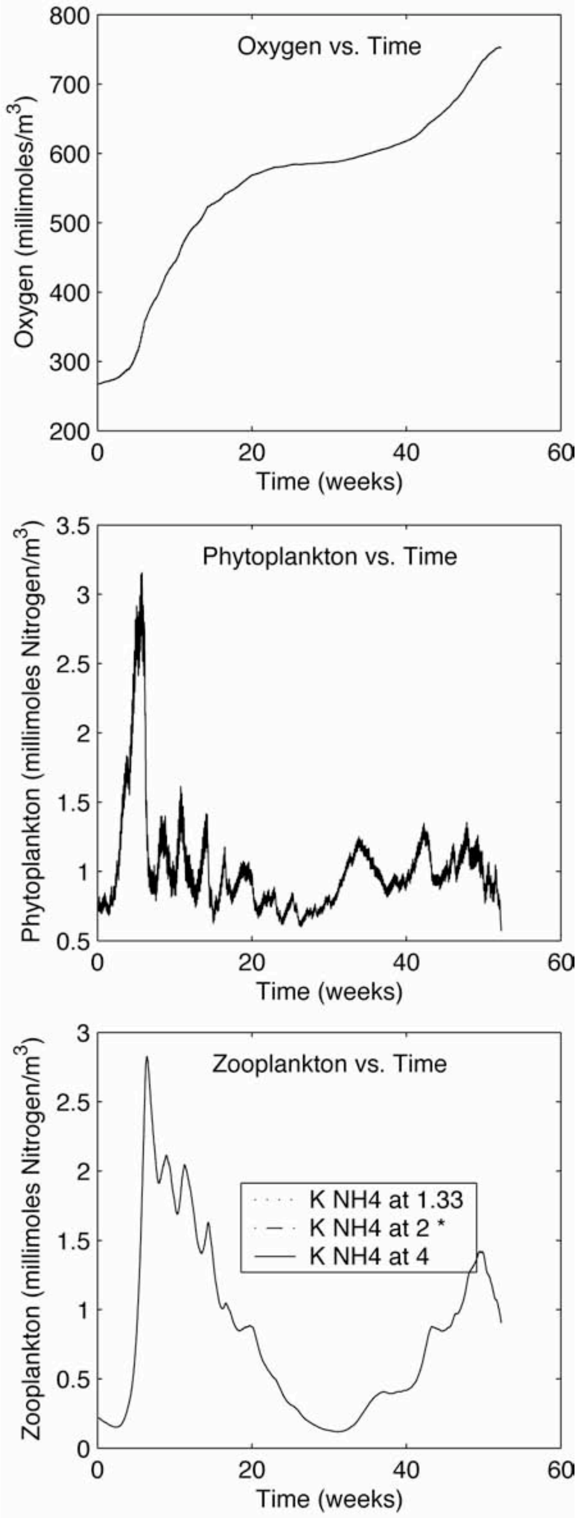

Figure 12. Comparison of three values for the inverse half-saturation for phytoplankton ammonia uptake (K_NH4) parameter. The three values were 1.33 mM N^{-1} m^{-3}, the default value (*) 2.0 mM N^{-1} m^{-3}, and 4.0 mM N^{-1} m^{-3}. The effects of the parameter changes were compared using the (**a.**) oxygen, (**b.**) phytoplankton, and (**c.**) zooplankton model results.

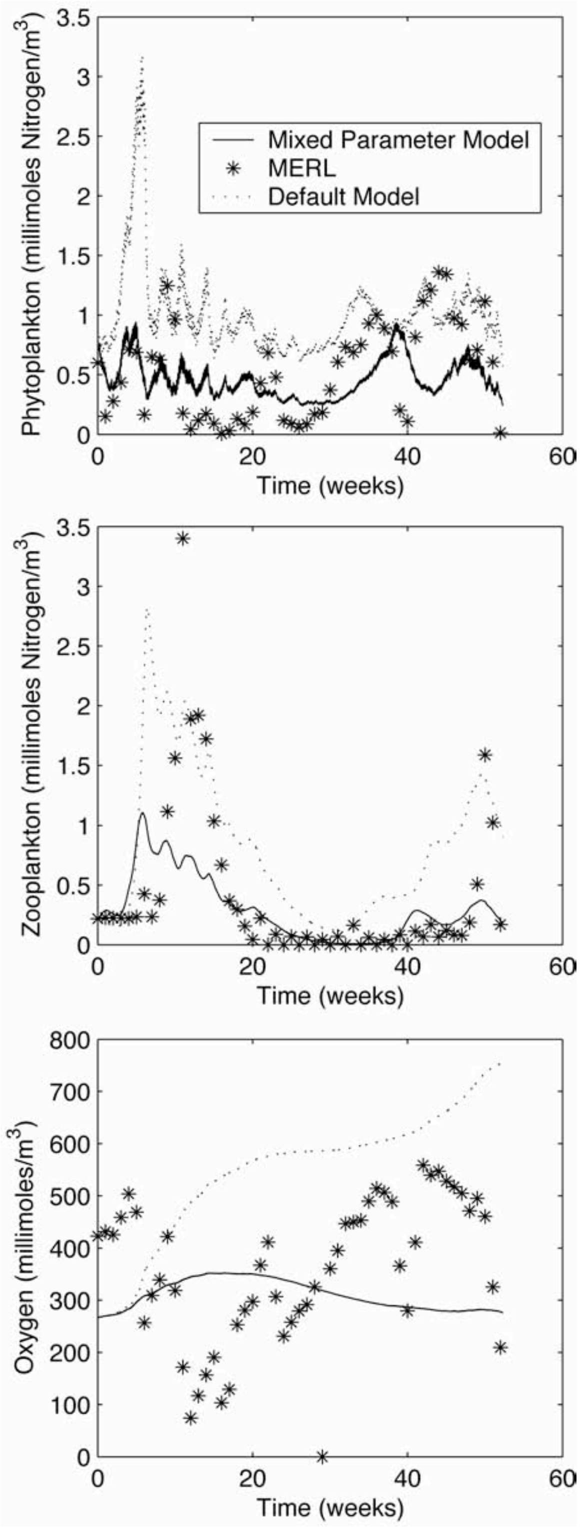

Figure 13. Comparison of a mixed parameter model run (solid line), the default model run (dotted line), and MERL data (star points). The mixed parameter effects were compared using the (**a.**) oxygen, (**b.**) phytoplankton, and (**c.**) zooplankton model results.

3.3. Mixed Parameter Model

The goal was to select parameters which produced the most realistic model results before using the model to predict ecosystem response to environmental conditions. To this point, the individual parameters were varied to better gauge their impact. Here we describe results of parameters combinations designed to produce an optimal match of the MERL data. The default model showed all of the variable results were relatively higher than the MERL data. After studying the parameter comparison results, the light attenuation due to seawater was set to 0.4 m^{-1} and the zooplankton half-saturation constant for ingestion was set to 0.5 mM N^{-1} m^{-3} because these values lowered all of the target variables (Table 3). The model oxygen results for this run showed that it lowered the oxygen concentration to the average of the MERL oxygen but still lacks the detail that the MERL data has (Figure 13a). The model phytoplankton results again lowered the default to be closer to the MERL phytoplankton range but the seasonal detail is missing from the model (Figure 13b). The model zooplankton was lower than the MERL zooplankton in the warmer weeks (weeks 0 through 20 and weeks 40 through 60) but showed similarity for the winter weeks (weeks 20 through 40) in the middle of the run year (Figure 13c).

4. Conclusions

The ROMS biological model works for the average value biology of Narragansett Bay but not for the seasonal values. One possible reason for this is the mesocosm chosen to be represented by the model. The 32X nutrient addition mesocosm added an excessive amount of ammonia into the mesocosm which could cause unstable relationships between the different variables especially dealing with processes like nitrification. A solution to this problem is to represent a lower nutrient addition mesocosm to have a more realistic ecology. Additional modeling experiments need to be conducted using the combined parameters to reach a greater similarity between the model and the MERL data. The model should also be tested using a temperature dependence on nitrification (Berounshy and Nixon 1990) and oxygen limitation on nitrification.

Acknowledgments. We thank the National Science Foundation for funding the SURFO program and everyone who was involved in the SURFO program for all of their support.

References

Bergondo, D.L., Examining the Processes Controlling Water Column Variability in Narragansett Bay: Time-Series Data and Numerical Modeling, Ph.D. Dissertation, University of Rhode Island, Narragansett, RI 02852, 187pp. 2004.

Bergondo, D.L., D.R. Kester, H.E. Stoffel, and W.E. Woods, Time-Series Observations During the Low Sub-Surface Oxygen Events in Narragansett Bay During Summer 2001, Marine Chemistry, in press. 2005.

Berounshy, V.M. and S.W. Nixon, Temperature and the annual cycle of nitrification in water of Narragansett Bay, *Limnology Oceanography*, 35(7), 1610-1617, 1990.

Deacutis, C.F., D.W. Murray, W.L. Prell, E. Sarrman, and L. Korhun, (in press). Hypoxia in the Upper Half of Narragansett Bay, RI During August 2001 and 2002, Northeast Naturalist, 2003.

Fasham, M.J.R., H.W. Ducklow, and S.M. McKelvie, A Nitrogen-based Model of Plankton Dynamics in the Oceanic Mixed Layer. *Journal of Marine Research*, 48, 591-639, 1990.

Oviatt, C.A., A.A. Keller, P.A. Sampou, and L.L. Beatty, Patterns of Productivity During Eutrophication: a Mesocosm Experiment. *Marine Ecology-Progress Series*, 28, 69-80, 1986.

Rhode Island Department of Environmental Management (RIDEM). The Greenwich Bay Fish Kill-August 2003. Causes, Impacts and Responses. http://www.state.ri.us/dem/pubs/fishkill.pdf 2003.

Shchepetkin, A.F. and J.C. McWilliams, Quasi-monotone advection schemes based on explicit locally adaptive dissipation, *Monthly Weather Review*, 126, 1541-1580, 1998.

Shchepetkin, A.F. and J.C. McWilliamns, A method for computing horizontal pressure-gradient force in an oceanic model with a non-aligned vertical coordinate, *Journal of Geophysical Research*, 108, 1-34, 2003.

Shchepetkin, A.F. and J.C. McWilliams, The regional ocean modeling system: A split-explicit, free-surface, topography-following coordinates ocean model, *Ocean Modelling*, 9, 347-404, 2005.

N. La Sota, D. Bergondo, and C. Kincaid, Graduate School of Oceanography, University of Rhode Island, Narragansett, RI 02882. (nlasota@yahoo.com, dbergondo@gso.uri.edu, kincaid@gso.uri.edu)

Deep Eddy Currents and Pressure Fields in the Kuroshio Extension

Dave Lishego,[1] Randy Watts and Kathy Donohue

Graduate School of Oceanography, University of Rhode Island, Narragansett, Rhode Island

Abstract. In 2004, 46 current and pressure recording inverted echo sounders were deployed off the eastern coast of Japan. The purpose of this study was to observe the Kuroshio Extension, a free jet formed from the Kuroshio western boundary current, and to characterize the dynamical processes governing the interactions between the Kuroshio Extension and its recirculation gyres. Data were recovered from these instruments in 2005 using pulse delay telemetry. The pressure data were de-drifted, removing a calibration drift caused by the high pressure (6000 dbar) conditions on the pressure sensor. A common mode, caused by local and remote atmospheric forcing was also removed. The processed data were then used to study the deep eddy currents and pressure fields by quantifying mean currents and variance ellipses, maps of eddy kinetic energy, correlation functions for the pressure data, and maps of the deep pressure anomalies. It was found that the deep circulation was dominated by the eddy field (magnitudes of 5-30 cm/s), while the mean currents were relatively weak (magnitudes less than 3 cm/s) . Features propagated southwest through the array contrary to original expectations. The features were time dependent, with periods of high energy and periods of low energy. In the future, studies may include determining the exact cause of the common mode and determining the generation, evolution, and propagation of deep eddies through the array and how these deep eddies are related to the meandering of the upper jet.

1. Introduction

The Kuroshio Extension, a free jet formed from the Kuroshio western boundary current off the eastern coast of Japan, creates a vigorously meandering boundary between the cold northern waters and the warm subtropical waters. A recirculation gyre exists south of the Kuroshio Extension and the region surrounding the Kuroshio Extension is home to one of the most intense air-sea heat interactions on the planet. These processes have many important implications regarding effects on climate, fisheries and storm tracks, among other things.

The importance of understanding this region led to the Kuroshio Extension System Study (KESS) project, a multi-year study of the Kuroshio Extension and surrounding area. The goal of the KESS project is to characterize the dynamical processes governing the interactions between the Kuroshio Extension and its recirculation gyres. The KESS project began in 2004 with a deployment cruise, where 46 Inverted Echo Sounders (IES) were deployed in an array (Figure 1). In 2005, a second cruise collected a years worth of IES data from 42 of the 46 sites (4 instruments did not return data). In 2006 there will be a third cruise to retrieve all of the instruments.

2005 proved to be an exciting year for collecting data in this region. The upper ocean currents transitioned from an extraordinarily stable state to a very unstable one, with large meanders and rings in the Kuroshio Extension. Moreover, for the first time in 20 years a large quasi-stable meander formed to the south of Japan. These changes are expected to modulate the cross-frontal fluxes.

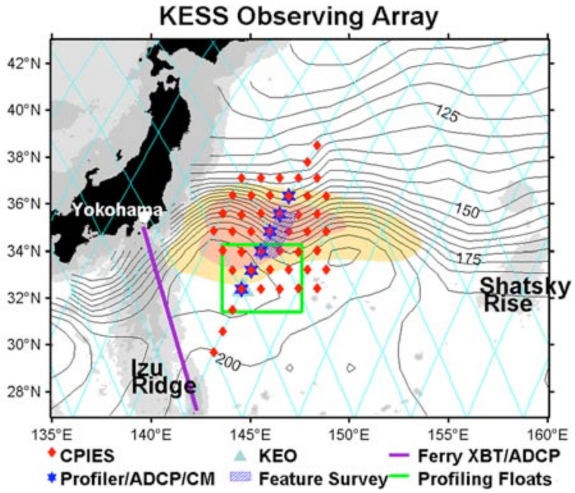

Figure 1. KESS array of C-PIES (red diamonds) and MPs(blue stars). Profiling floats were deployed within the green boxed region. Thin blue lines indicate T/P-Jason 1 ground tracks; the magenta line indicates the TOLEX Ogasawara ferry route. Solid lines are mean surface dynamic height contours in dyn~cm from Teague et al. (1990). The 2000 and 4000~m isobaths are shaded dark and light gray, respectively. Eddy kinetic energy > 0.18 and 0.24 m^2/s^2 is color shaded yellow and orange, respectively. Approximate locations of CTD/SADCP feature surveys shown in blue hatched region.

2. Data

The data used in this study were taken from IES deployed in the summer of 2004. Two types of IES were used: Pressure recording Inverted Echo Sounders (PIES) and Current and Pressure recording Inverted Echo Sounders (CPIES). PIES recorded the bottom pressures, acoustic travel time (tau) and yearday. CPIES recorded the same data as PIES, but also had a current meter to record current speed and heading.

---

[1] Now at Pennsylvania State University, University Park, PA.

These instruments were bottom mounted; the average depth was 5000-6000 meters. Both types of instruments sampled pressure and tau data every ten minutes and current data every 20 minutes (two sites sampled current every 10 minutes), then processed data internally and created a mean daily data file for each yearday. The tides were removed from pressure and current data.

3. Methods

The data from the PIES and CPIES were retrieved using pulse delay telemetry, which allowed the data to be collected without having to recover any instruments. Once the data were obtained, further processing was required for analysis. This processing included both de-drifting and removing a common mode from the pressure time series.

Due to the high pressure conditions at these great depths, the pressure sensors gave readings with an exponential drift (Watts et al. 1990). This drift caused the time axis for the pressure time series plots to have the shape of an exponential decay, as seen in Figure 2. A Mat Lab program was used to remove this drift, and focus upon the residual oceanographic signal. These drifts were typically less than .2-.5 dbars.

In addition to the drift, a common mode also had to be removed from each of the pressure time series. This common mode, a coherent signal across all of the pressure time series, will be the subject of a future study and was likely caused by local and remote atmospheric forcing. The common mode, shown in Figure 3, was calculated by taking the mean pressure of across all sites for each day in the series. This signal has a magnitude on the order of .1 dbar. Removing the common mode had no adverse effects on the calculations done in this study, since only the pressure gradient is relevant to eddy currents, and removing this signal from every site leaves the gradients unaffected. The final processed pressure time series for each site are shown in Figure 4.

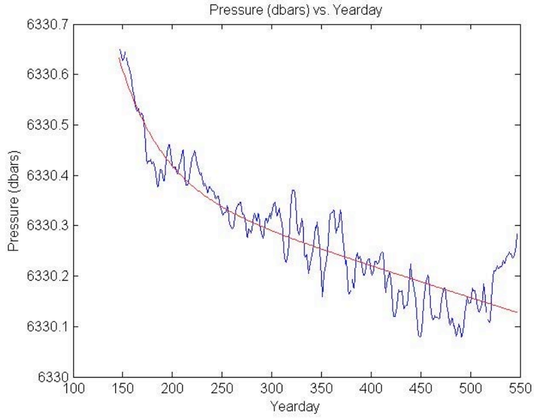

Figure 2. The blue curve represents the raw pressure time series before de-drifting, and the red curve is the fit for the drift curve.

4. Results

Mean currents and variance ellipses were calculated for each site in the array, shown in Figure 5. This showed that the mean currents were very small, on the order of .006 cm/s, while the variance is high. In other words, deep eddies dominated the circulation.

Next the Eddy Kinetic Energy (EKE) was calculated and contoured (Figure 6). The EKE, is given by:

$$\mathrm{EKE} = \_\ (u'^2 + v'^2) \qquad (1)$$

Where u' and v' are the zonal (u) and meridional (v) velocity components with the means removed. EKE is a measure of the kinetic energy of the deep eddy field.

The pressure data were also examined, beginning with the calculation of correlation scales. It was found that once the data were processed (drift and common mode removed) the pressure data were very highly correlated, with a length scale of 114 km. Figure 7 plots the correlation coefficient vs. distance between sites. This scale is much larger than the station spacing. The array resolves the eddies and future mappings would be very successful in interpolating between the sites.

After processing, the pressure data were used to create maps of the bottom pressure fields. These maps, shown in Figures 8-10, on which the current vectors were superimposed, proved very useful in examining the propagation of features. The high pressure, anti-cyclonic eddies had current vectors which were rotating clockwise, and the low pressure, cyclonic eddies had current vectors which were rotating counterclockwise. This showed that all of the sensors were working accurately and gave physically consistent readings.

5. Conclusions

The first year of data from the KESS array, showed that deep circulation was dominated by the eddy field and not by the mean field. Features propagated through the

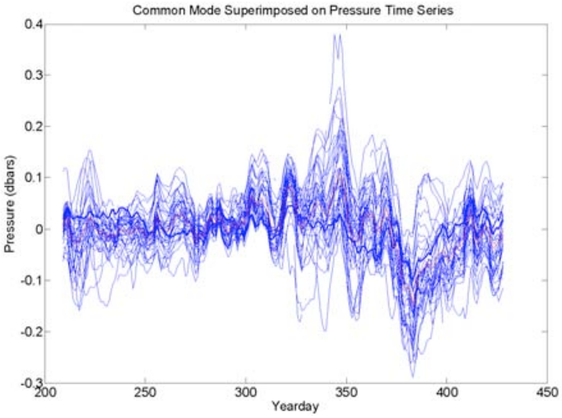

Figure 3. The blue curves represent the pressure time series for each individual site all superimposed on one another. The red curve is the common mode across all of these sites, which shows a very strong correlation to the individual series.

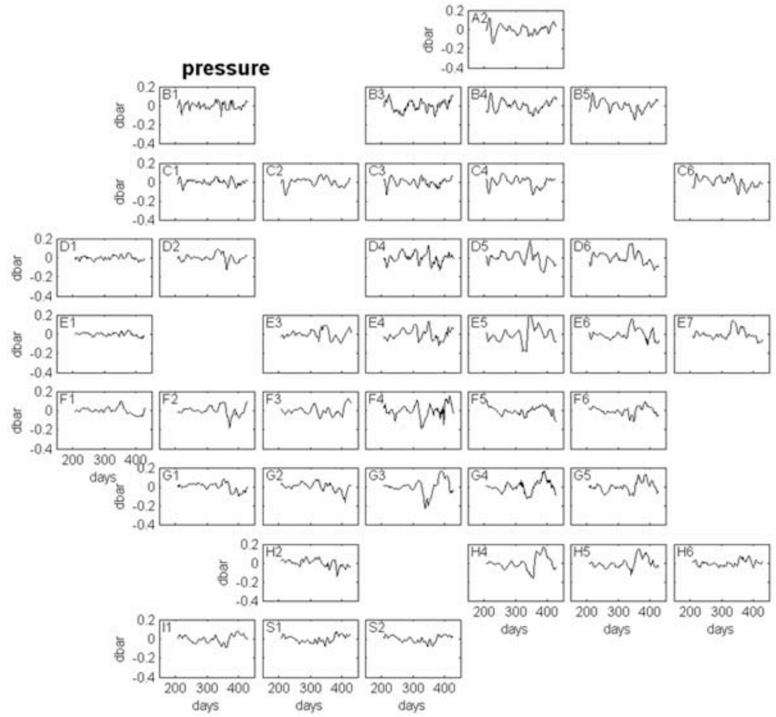

Figure 4. Fully processed pressure time series for each site in the array over the full range of days arranged geographically. The letter/number designations (i.e. H3) are the site designations in the array

..

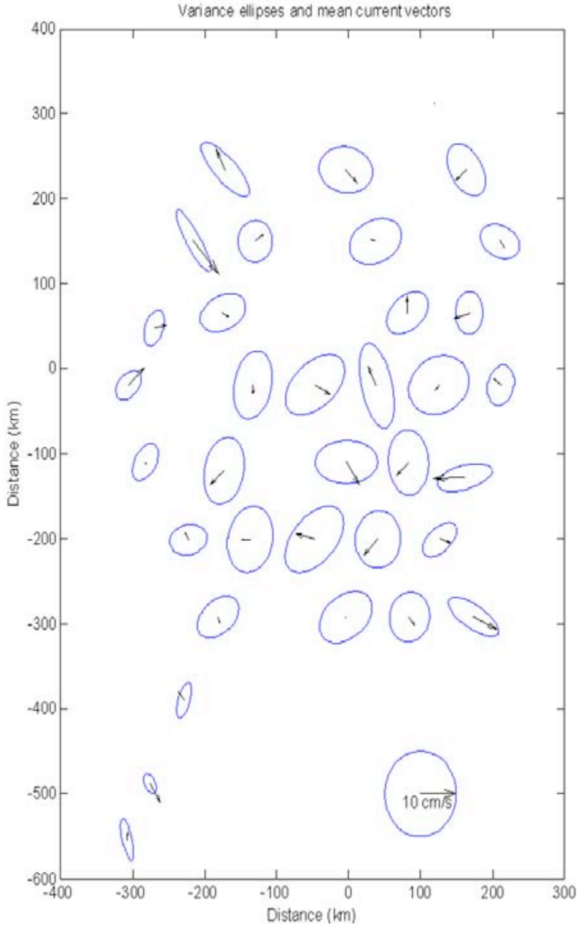

Figure 5. Variance ellipses and mean current vectors for each site in the array.

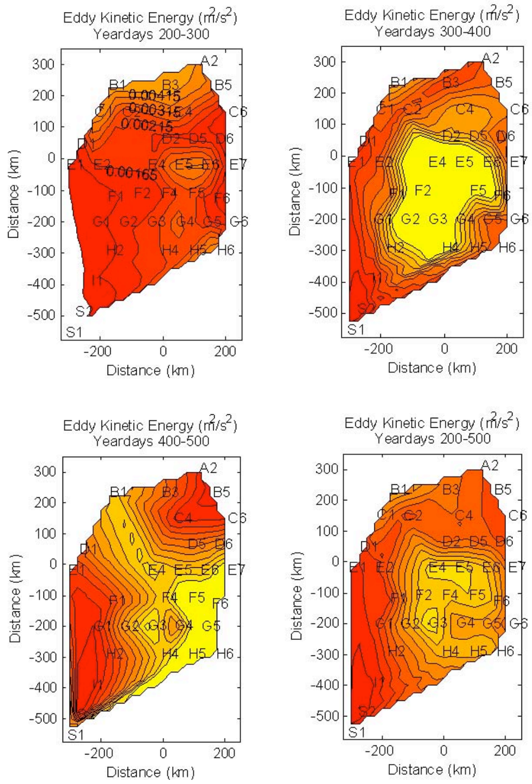

Figure 6. EKE contoured in 100 day segments, starting from day 200 and ending with day 500. Yellow regions have the highest energy, and red regions have the lowest energy. Contour interval is .0005 m^2/s^2. The earlier portion of the range has much lower energy, whereas the middle part, days 300-400 have very high energy. The origin (0,0) on this plot represents 35°N 146.5°E.

array, moving from northeast to southwest, which is contrary to our original expectation from Gulf Stream studies (Watts et al. 2001) that deep features would propagate due west. These features were time dependent, with periods of high energy and periods of low energy, as shown by the fluctuations in energies and pressures over the course of the year.

Overall the first year of the KESS project was successful, with 95% of the possible data recovered. There is still a great deal of research to be done. Future studies may include determining the exact cause of the common mode and determining the generation, evolution and propagation of deep eddies through the array and how they are related to the meandering of the upper jet.

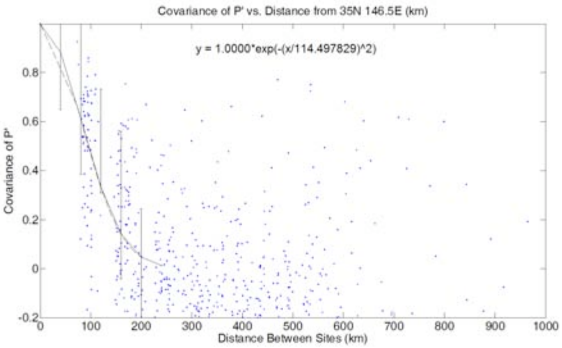

Figure 7. Shows the correlation coefficient vs. the distance between sites. The correlation function and an error bar set with 40 km bins are also shown.

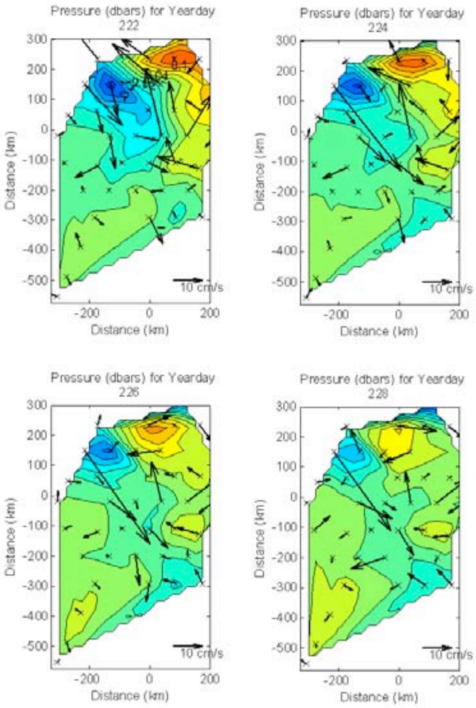

Figure 8. A cyclone-anticyclone pair propagates through the northern part of the array. The red areas represent the highest pressures (up to .2 dbars), the blue areas the lowest (down to -.2 dbars). The contour spacing is .02 dbars.

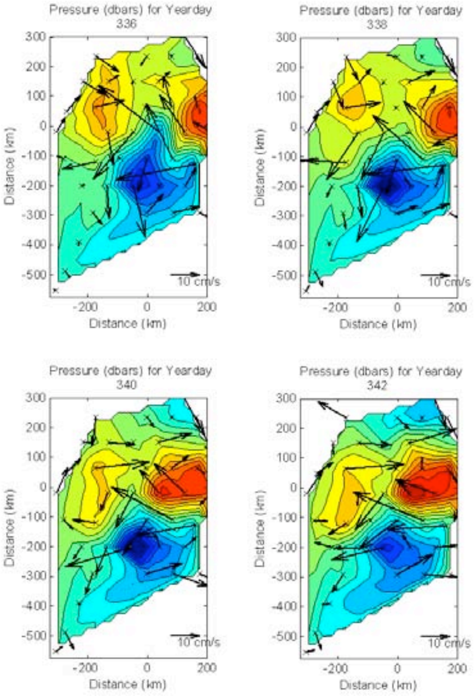

Figure 9. Several strong pressure anomalies propagated southwest through the array during this highly energetic time period (days 300-400). Contour intervals and shading as in Figure 8.

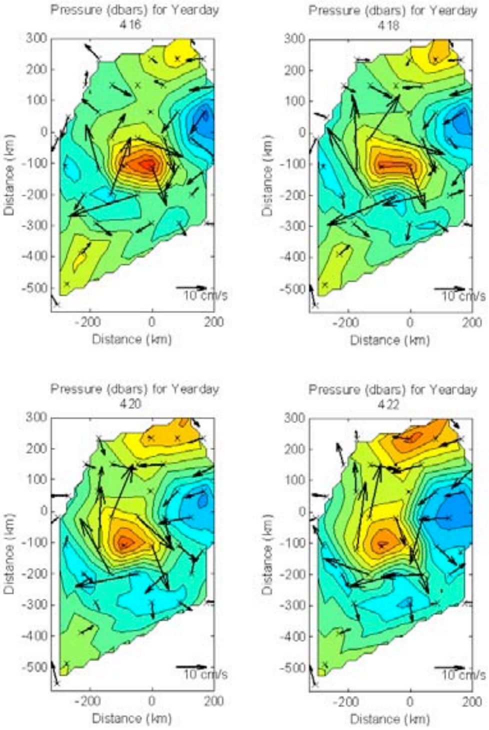

Figure 10. Eddies propagating southwest through the array in the time period between days 400-500. Contour intervals and shading as in Figure 8.

References

Teague W.J., M.J. Carron, and P.J. Hogan, 1990: A comparison between the Generalized Digital Environmental Model and Levitus climatologies. *J. Geophys. Res.,* 95, 7167-7183.

Watts, D.R., and H. Kontoyiannis. 1990. Deep-ocean bottom pressure measurement: Drift removal and performance. *Journal of Atmospheric and Oceanic Technology* 7:296-306

Watts, D.R., X. Qian, and K.L. Tracey. 2001. Mapping abyssal current and pressure fields under the meandering Gulf Stream. *Journal of Atmospheric and Oceanic Technology* 18:1052-1067.

Pings and Pongs: Basics and Applications of the BEAMER Acoustic Sensor System

Kevin Miklasz,[1] Tetsu Hara, David Farmer, Svein Vagle, and Peter Chandler
Graduate School of Oceanography, University of Rhode Island, Narragansett, Rhode Island

Abstract. Understanding bubble cloud formation and distribution is essential to understanding various air-sea interaction processes. This is especially true for high-wind environments, where bubbles play a vital role in air-sea gas transfer. Acoustic sensors and direct photography are two of the numerous methods used to study bubble clouds. A new acoustic sensor system called the BEAMER is set to be installed in Narragansett Bay. This devise will be used to study bubble clouds, surface waves and other physical and biological processes. The purpose of this study is to test the versatility and accuracy of the BEAMER acoustic sensoring system before it is installed in Narragansett Bay. The study is based on data taken from Martha's Vineyard in November through December of 2002. The results from the available data demonstrate that the system can be used to study bubble cloud formation and distribution. They also illustrate a desired range and relative placement of the sonars with respect to each other.

1. Introduction

The significance of bubble clouds in air-sea gas transfer has become more and more evident in recent years. In particular, for high wind speeds bubbles begin to dominate as the main means of gas transfer (Bortkovskii, 2002). Specific attributes of bubbles, such as size, distribution, and duration, are particularly important for determining how much bubbles contribute to the gas transfer. Measurement techniques of bubbles have included direct photography and acoustic sensors (Melville, Terrill and Ding, 1995, Vagle and Farmer, 1998). Bubble cloud measurements have been taken in laboratory environments as well as in the open ocean using both these techniques. Many open ocean measurements have been conducted from floats on the surface, following the near surface current (Farmer, 1995). Few studies have examined field conditions from a fixed sensor over an extended period.

A new acoustic sensing system entitled the BEAMER is set to be installed in Narragansett Bay. This sensor will be in place for a long time period (up to a few months) in the bay. This sensor is very versatile, allowing for its angle and position to be changed either manually or through a remote controlled system. The BEAMER is capable of looking both vertically and horizontally, with a circular beam spreading from the vertical sonars and a thin planar beam spreading from the horizontal sonars. This system will be able to measure the same ocean section for long periods of time. With its location held as a constant, prolonged studies of bubble clouds may be obtained in different weather conditions

The intent of this research is to estimate the versatility and accuracy of the new acoustic system before it is installed in Narragansett Bay. Much of the data was acquired from a test run of the BEAMER system in Martha's Vineyard from November and December of 2002. Although the sonar's relative location and direction were unknown from the test data, much can be still gained from the existing experimental data. In particular, the data sets are used to test two different models of bubble cloud shape and measure their relevant parameters. In addition, the possibility of using the system to study bubble cloud formation and decay is examined.

2. Methods

2.1 Data processing program

Data Format

The format of the data changed several times during the data acquisition period. The final matlab code is set to read the data in the format used for the last segment of the experiment, in early December. Two inputs are received at each moment in time, the Inphase and Quadrature components, or the real and imaginary components of the wave. The data from the two sensors in each data file is interlaced. The code de-interlaces the data, and sets the component to a pre-defined zero reference.

Intensity Calculation

The intensity is calculated according to the following formula:

$$\text{Intensity} = \text{Inphase}^2 * \text{Quadrature}^2 \qquad (1)$$

The intensity is then converted into decibels according to the following manipulation, 10*log(intensity).

Velocity Calculation

The Inphase and Quadrature components are taken at a specific moment in time and a subsequent quarter wavelength later. The complex amplitudes of each time moment are multiplied together, and the phase angle of the resulting complex amplitude is taken to be the Doppler shift. The inverse tangent of the complex pair is taken to find the phase angle and then multiplied by VI, a constant which puts the value into cm/s. The

---

[1] University of Chicago, Chicago, IL

formula for the velocity is given by the following equation:

$$Vel = VI*atan2(I2*Q1-I1*Q2,\ I1*Q1+I2*Q2) \quad (2)$$

where I and Q stand for Inphase and Quadrature components respectively, and 1 and 2 correspond to the original time and the time a quarter wavelength later, respectively.

Time and Range Averaging

In the beginning of the codes there are two variables, the time and range thinning factors. These factors average the data in either time or range. The number of points that are averaged together is equal to the average factor. Therefore, the length of the data is equal to the total length divided by the average factor. Averaging is done after intensity and velocities have been calculated, so they do not affect the placement of the quarter-wavelength jump in the velocity calculations.

Sonar Spread and Absorptions Correction

To account for sonar spread and absorption, corrections in the intensity data are added. According to the following formula (RD Instruments, 1996):

$$Int_{corr} = Int_{raw} + 40*\log_{10}(Range) + 4*\alpha*Range \quad (3)$$

where α is the absorption coefficient and can be changed at the beginning of the program, and Range is the distance each intensity data point is from the sonar. In general, these corrections are relatively small, though they are very important for such studies as the depth distribution estimation of bubbles using the topscan system. An important note: while the present data has been corrected for the sonar spread and absorption, the intensity graphs are not calibrated. Calibration was not performed for the instruments in this experiment. Therefore, the intensity calculations are not written as absolute decibels.

Filtering

Two filtering routines were employed in the program. Both used the filtfilt routine in Matlab. The first filter is a noncausal averaging filter, which removes insignificant fluctuations in the intensity data. It makes the bubble clouds easier to see. It can be set as an n-point filter, where n defines the range over which the averaging occurs. This filtering is implemented in the topscan and sidescan intensity data.

The second filter is a Chebyshev Type I bandpass filter. The passband is set with the Wp parameter and the falloff on either side of the passband is set with the Ws parameter. This filtering is used in the topscan sea surface data and in the sidescan velocity data, since periodic patterns are expected in both those data sets.

Fourier Transforms

Fourier transform methods are built into the program as well. The program is set to take Fourier transforms of sea surface data and velocity data. The data is chopped into 2*avefact-1 overlapping parts. The Fourier transform of each of these data sets is taken separately using a Hamming window, which is subsequently averaged together. The program can find the power-frequency spectrum of sea surface data. It can also take slices of the velocity data in range or time to find the power-frequency or power-wavenumber spectrum, respectively. Time and range slices taken are specified by the xx and yy variables found directly before the Fourier transform routine. The time slice spans a small range, and the range slice spans a small amount of time. Each time slice is averaged with respect to range, or range slice with respect to time, to result in a one dimensional data set. A routine is built into the program which takes the two dimensional Fourier transform of the velocity data and finds the Power vs. frequency and wavenumber graph. The limits of the Fourier transform are again specified by the xx and yy variables directly before the two dimensional Fourier transform.

Unusable Data

Several observations need to be made of the raw intensity data given from the topscan and sidescan data. For both systems, the data up to 4-5 m in front of the sonar is unusable due to ringing. Ringing is caused by leftover energy in the transducer after transmission has stopped. It takes time for this energy to die away before the transducer can act as a receiver. Fortunately, this does not greatly affect the data.

An additional concern is near-surface intensity measurements in the topscan system, especially on active days. This data was often hard to accurately understand. Data close to the surface can be considered unusable, depending on the spread of the sonar given by the following equation (add reference):

$$R_{max} = D * \cos(\theta) \quad (8)$$

where R_w is the maximum distance from the sonar data is usable, D is the water depth, and θ is the angle at which the sonar spreads. The spread of the sonar is not known in the Martha's Vineyard data, but this effect is observed 2-4 m below the surface. This gives reasonable sonar spread between 29° and 41°.

There is yet an additional concern in the sidescan system. Reflection from the surface and bottom interferes with the sonar signal, until the signal is able to level itself out. As a result, accurate bubble cloud information is started approximately 25-30 m from the sidescan sonar. In addition, the sidescan sonar stops detecting bubbles at range of about 80–100 m. Hence, there is roughly 50-60 m of usable data.

2.2 Interpretaion of data

Sonar Direction

The sonar direction is not recorded for the data set analyzed. Therefore it is calculated from the sidescan intensity data as follows. The velocity of the bubble clouds as seen by the sonar is calculated from the intensity data. The angle φ between the sonar and the current direction (which is always either east or west) is calculated as follows:

$$v = c * \cos(\varphi) \qquad (4)$$

where v is the measured velocity and c is the current speed determined from other instruments (obtained from the web site of the Martha's Vineyard Coastal Observatory).

Bubble Cloud Dimensions

Bubble clouds are modeled in two different ways. The first method models the bubble clouds as circular masses that extend into the water in a roughly conical shape (Figure 1). Therefore, two important dimensions are measured, cloud diameter and depth. Both diameter and depth can be measured directly from the sidescan and topscan sonar. The depth is simply the maximal penetration of each bubble cloud. The diameter is the maximum range covered by the cloud as it passes through the sonar's view. This gives the parallel diameter, or, the cloud's diameter along the direction of the sonar. To check for accuracy of the model, one may also calculate the cloud's dimension perpendicular to the sonar,as:

$$\text{Diameter} = t * c \sin(\varphi) \qquad (5)$$

where t is the total time the bubble cloud takes to pass through the sonar. This perpendicular diameter should match well with the parallel diameter if the circle model of bubble clouds is accurate.

In the second model, the bubble clouds are rectangular and have three dimensions, a length l and a width w and some depth. We'll assume for simplicity that the length is much greater than the width. The depth is measured in the same way as the circular model. The length is considered to be perpendicular to the wave direction, and the width parallel to the wave direction (Figure 1). The width is then related as follows:

$$\text{width} = x \cos(\alpha - \beta) \qquad (6)$$

where x is the measured maximum range of the bubble cloud, ϕ is the direction of wave propagation, and σ is the sonar angle, with both angles measured relative to the current direction. The length and the width are also related as follows:

$$c*t = \text{width}\{\cos\alpha+\cot\beta\sin\alpha\}+\text{length}\{\cot\beta-\tan\alpha\} \; (7)$$

where t is the total time that the bubble cloud is in view of the sonar. This equation is valid provided the length is bigger than $x*\sin(\alpha - \beta)$. Otherwise,. the distance measured along the sonar, or x, does not correspond to the width but rather to the length.

Bubble Cloud Spacing

The spacing between bubble clouds is measured in the sidescan and the topscan systems. In the topscan system, time between the end of one bubble cloud and the beginning of the next is multiplied by the current to give the spacing. This is given by:

$$\text{Spacing (topscan)} = \text{time} * c \qquad (6)$$

In the sidescan system a certain range is chosen. For this range, the time between the end of one cloud and the beginning of another is multiplied by the current perpendicular to the sonar, or:

$$\text{Spacing (sidescan)} = \text{time} * c * \sin(\varphi) \qquad (7)$$

Bubble Cloud Depth and Intensity

Two manipulations are made of the basic intensity plot. First, the intensity is integrated at each moment in time to give the total intensity as a function of time. Second, the depth that a certain percentage of the bubbles reach at each moment in time is calculated to give the bubble cloud depth as a function of time. The percentage of bubbles used to calculate the depth is given by the variable bubblepercent in the program.

3. Results and Discussion

3.1 Filtering

The filtering technique greatly improves data clarity. Figure 2a illustrates how the noncausal filter clarifies the bubble cloud images. Figure 2b shows how the noncausal filter works on the sidescan intensity data, and Figure 2c shows how the Chebyshev filter works on the sidescan velocity, after a filter in both time and range. Figure 3 demonstrates how the Chebyshev filter

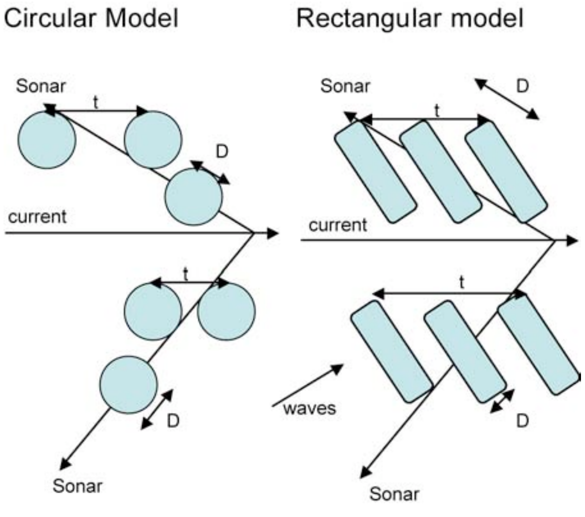

Figure 1. This figure represents the two bubble cloud models and shows how the bubble cloud would pass through the two likely sonar beams.

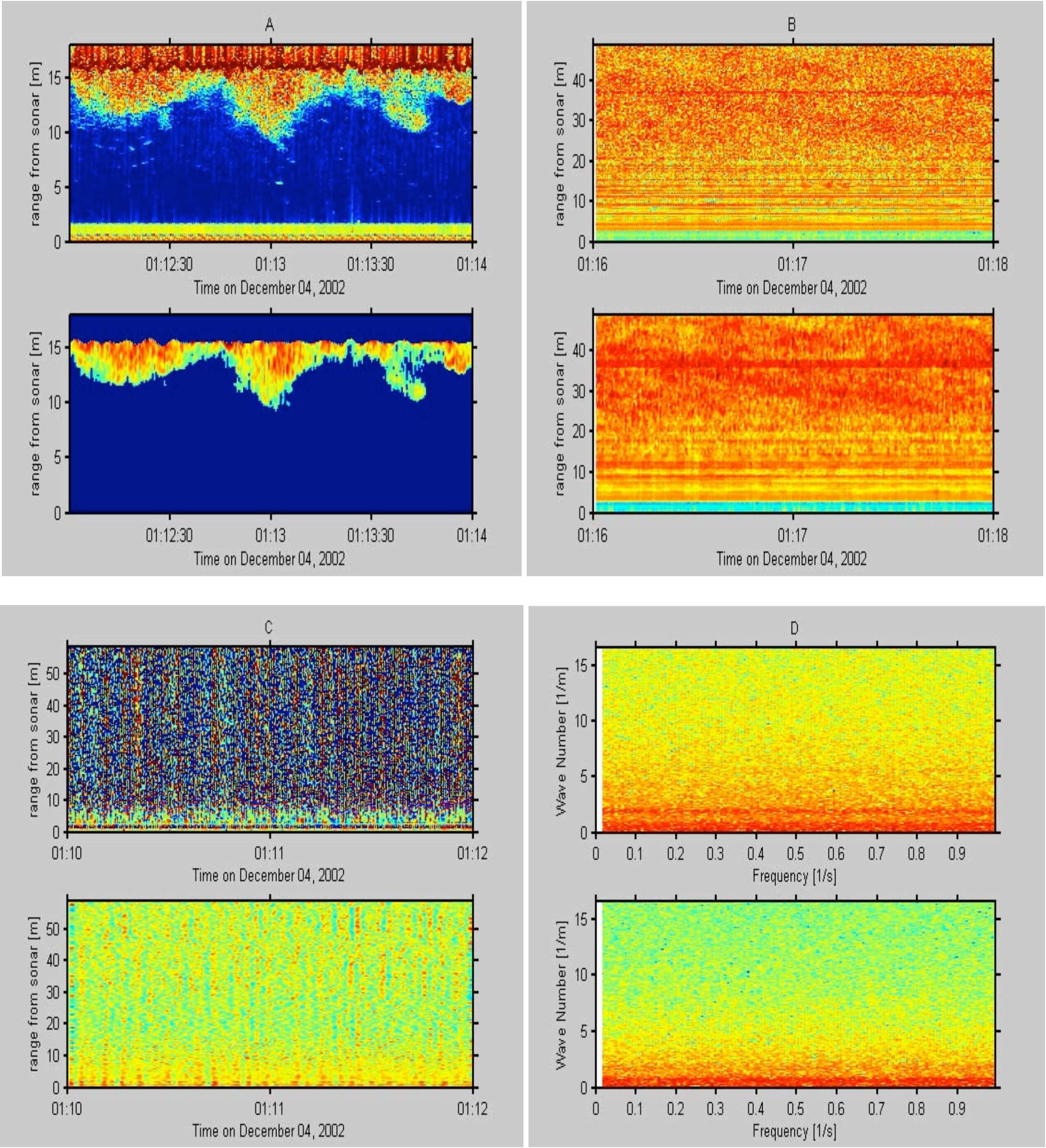

Figure 2. A: Topscan intensity is plotted as a function of range and time. The top panel shows unfiltered results and the bottom panel shows results after noncausal filtering is applied. B: Sidescan intensity is plotted as a function of range and time. The top panel shows unfiltered results and the bottom panel shows results after noncausal filtering is applied. C: Sidescan velocity data are plotted as a function of range and time. The top panel shows unfiltered results and the bottom panel shows results after a Chebyshev filter is applied in both time and range. D: The top and bottom panels show the two dimensional fourier transform of the sidescan velocity data from two different sonars.

works on the sea surface data. In all of these cases the data's clarity is improved and patterns emphasized.

3.2 Surface elevation

The frequency spectrum of the sea surface data is shown in Figure 4 for a calm day and a stormy day. It is found that the energy is held in the range expected for ocean waves. On the calm day, most of the waves are between 0.1 and 0.5 Hz. There are peaks at 0.12 Hz and 0.3 Hz, for the swell and wind waves, respectively. For the stormy day, there is one strong peak around 0.1 Hz. At this point in time, the storm had been going for quite a while. The wind waves had built up to the same frequency as swell waves, generating one strong peak. The stormy day has much more energy in its waves than the calm day by several orders of magnitude, as can be seen in the log plot. This all corresponds very well with the weather information obtained from the observatory web site.

3.3 Bubble clouds

There are four days in which samples were taken; a

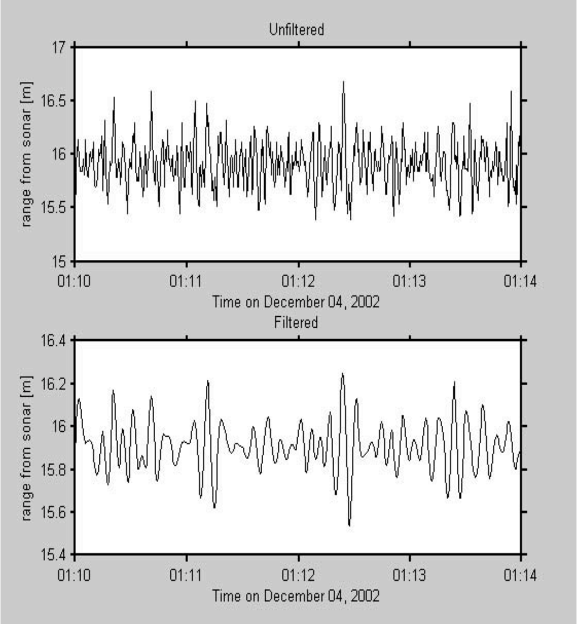

Figure 3. Topscan sea surface elevation data are shown without filtering (top panel) and with the Chebyshev filter (bottom panel).

calm day, two moderate wind days, and a stormy day.The topscan and sidescan are both present for the calm and stormy days. For each moderate wind day only one of the two sonars are in view. The calculations of spacing and dimensions are shown in Table 1, with comparisons of parameters from both models.

Two graphs illustrate bubble cloud time series; one from the calm day and one from the stormy day (Figure 5). Although each graph spans only a small time frame, about three minutes, they are representative of the entire data set for each day.

Sonar Angle

The calculations of the sonar angle with the circular bubble cloud assumption give reasonable results. The two days close to each other in time, the calm day and the stormy day, have the same sonar angle. The mild day has a completely different angle, but was taken almost a month beforehand. The sonar angle was probably changed from the mild day to the stormy day, but was not changed from the stormy day to the calm day, given the length of the time intervals. And this is indeed what is found from the results.

Bubble Cloud Depth and Spacing

The spacing and depth calculations are shown in Table 1. The depth data show slightly deeper clouds on stormier days. The spacing data are scattered. There is no definite trend to the data with respect to weather conditions, although the data set is quite small. There is a mismatch in topscan and sidescan measurements, and an order of magnitude mismatch between the mild days and the other days. This is probably because the data are not calibrated. These measurements depend a large part on the definition of the edges of bubble clouds, but each data set had values that spanned completely different ranges. This made such a definition of edges rather arbitrary. The same problem of edge definition may have caused the discrepancy between the topscan and sidescan spacing. Since these sonars look at bubble clouds in different ways, it is hard to find a common definition that works for both.

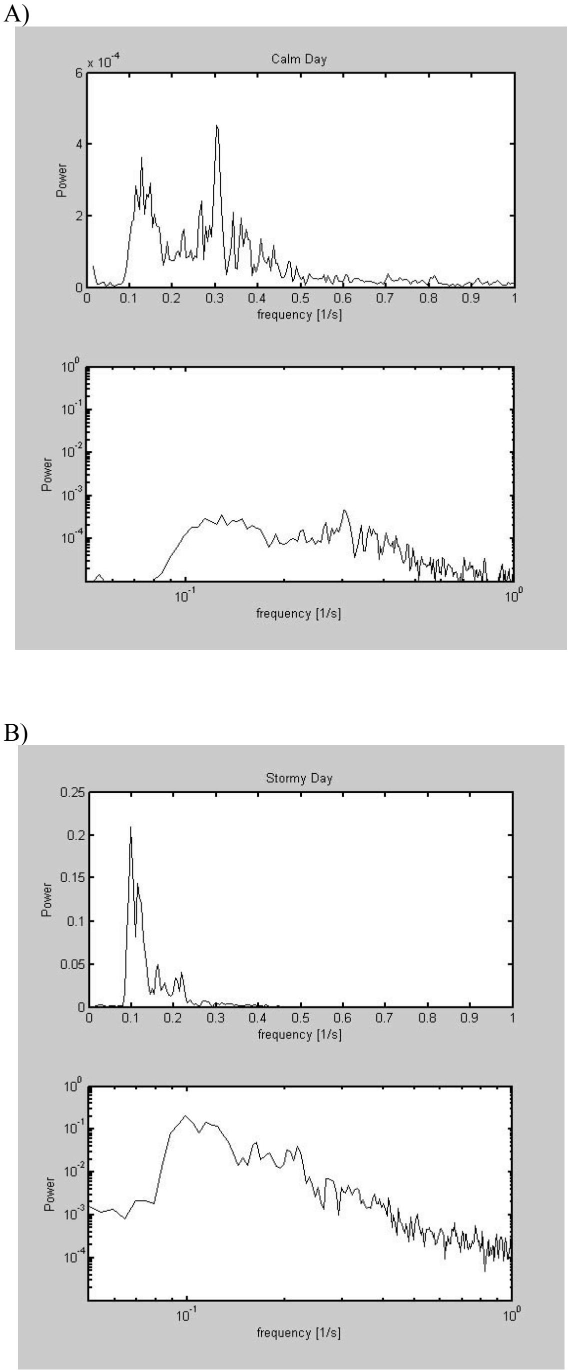

Figure 4. Power-frequency spectra of the topscan sea surface elevation data are shown for a calm day (A) and a stormy day (B). The top panels are in normal scale and the bottom panels in log scale.

	Calm	Mild (sidescan)	Mild (topscan)	Stormy
Date	4-Dec	7-Nov	3-Dec	30-Nov
Wind Speed (m/s)	5	10	8	11
Current speed (m/s)	0.35	0.25	0.20	0.15
Current direction (from N)	100	100	100	100
Wave direction (from N)	240-200	240-190	240-200	210-210
Sonar Angle (degrees)	19	74		18
Sidescan Spacing (m)	8.0	22.5		3.9
Topscan Spacing (m)	13.5		34.6	10.2
Max Depth (m)	4.8		5.8	5.5
Parallel Diameter (m)	7.4	5.1		7.8
Normal Diameter (m)	4.3	14.2		3.8
Width (m)	4.7	5.1		4.9
Length (m)	8.7	4.7		18.3
Check Length (m)	5.7	3.0		6.1

Table 1. List of the bubble cloud dimensions and spacing and environmental conditions for different days. All oceanographic and meterological data is taken from Martha's Vineyard Observatory website http://www.whoi.edu/mvco/data/data.html.

Bubble Cloud Models

First, the model of circular bubble clouds is tested. The parallel diameter and the perpendicular diameter estimated from this model are shown in Table 1. If the model is valid, these two diameters should be similar. However, the days with a sonar angle of 18-19^o had lower perpendicular diameters, but the days with a sonar angle of 74^o had a lower parallel diameter. This seems to suggest that the bubble clouds are not radially symmetric.

It seems likely that the bubble clouds may be orientated along the wave propagation directions, so dimensions were defined along the coordinates defined by the wave propagation in the second model. In all cases waves were propagating from about 210^o measured from N.

The results are shown in Table 1, along with the length check, or the minimum length the measurement must be for this model to be accurate. The calculated lengths all pass the length check. The length calculated for the calm and stormy days seem to be reasonable, and correspond well with the weather conditions. Bigger bubble clouds are found on the stormier days. The data from the mild day is not so good, with the length actually slightly shorter than the width. This could be due to slight inaccuracy in the wave and current angle information obtained from the Martha's Vineyard website. A larger data set and more complete model are needed to determine if this truly is a good model or not.

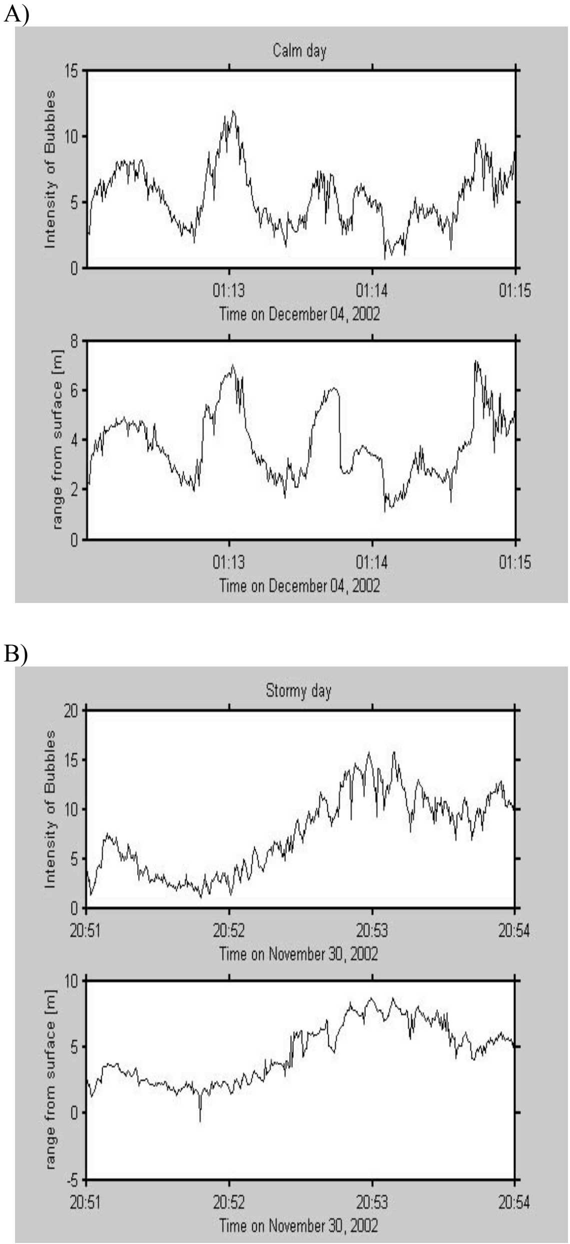

Figure 5. Time series of bubble clouds are shown for a calm day (A) and a stormy day (B). The top panels are the bubble cloud intensity integrated over the water column. The bottom panels are the depth 85% of the bubbles reach as a function of time.

Bubble Cloud Formation and Decay

The graphs outlining the time series of bubble clouds, Figure 5, show some interesting trends. The first trend to note is that the calm day has a current of 35 cm/s, whereas the stormy day has a current of about 15 cm/s. This accounts for the different number of bubble clouds seen on each day. This also means that the calm day is more likely to see bubble clouds that are simply passing through the sonar's view, whereas the stormy day is more likely to see bubble clouds forming or decaying directly overhead.

Looking at the graphs more closely, the graphs for the intensity and depth on the calm day seem to be pretty much in phase with each other. This indicates that bubbles are evenly dispersed over the depth. In the stormy day, the intensity graph seems to reach its peak about 10 to 15 seconds before that of the depth graph. This indicates that bubbles are first generated near the surface and then are carried deeper afterwards, which is what one would expect to find as a wave breaks and forms a bubble cloud. The phase of these two graphs could be used in such a way to study bubble cloud formation process.

A second interesting trend is found in the slope of the two graphs. The slow day has much steeper slopes than the stormy day. The steep slope in the data occurs when a bubble cloud is pushed by the current into or out of the sonar's view. The process is much more gradual and continuous in the stormy day, corresponding to a slower current.

3.4 Doppler velocity

The Doppler velocity data were not as reliable. One would expect this data to resemble a wave pattern, as the back and forth motion of the incoming waves is mapped out. This pattern was not found, though some signals were found in the data. The Fourier transform of time and range slices of the sidescan velocity graph is shown in Figures 6a and 6b, respectively. In addition, the two dimensional Fourier transform of the sidescan velocity graph is shown in Figure 2d for two different sonars.

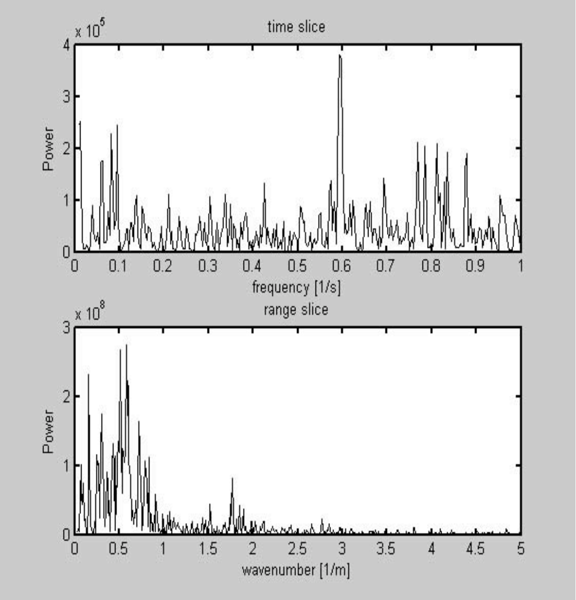

Figure 6. Power-frequency spectrum (top) and Power-wavenumber spectrum (bottom) of the sidescan velocity data.

The frequency spectrum seems to have random scatter except for a relatively strong signal around 0.6 Hz. Looking at the data, this signal is much too regular to be ocean waves. It must be assumed that this is some sort of background noise, possibly from the sonar being inadequately secured. This signal does not show up in all the data; in some data sets we only see random scatter.

The filtered velocity graph in Figure 2c (lower panel) seems to have some patterns running through it that are absent from the unfiltered graph. Specifically, there is a strong, slightly irregular signal which occurs about every 5 s, a reasonable period for ocean waves on that day. However, if the Doppler data truly maps wave motion, this signal should propagate through time as waves do. The observed signal is almost uniform in space, showing no propagation.

A two dimensional Fourier analysis should reveal energy concentrated along the dispersion relation of ocean waves. Unfortunately the actual graph simple shows a concentration of energy at low wavenumbers across the whole frequency range (Figure 2d). The scales of the two axes are very different from each other and not ideal for observing such a curve. This is due mostly to a function of the system itself. The sidescan sonar does not reach a large enough range to analyze very low wavenumber signals. In addition, the signal itself grows worse with range, rendering it impossible to understand the wave signal for this data set.

3.5 Future installation

Based on the observations seen from the sonar and the analysis of the results, several factors need to be considered when installing the new system in Narragansett Bay. The first and biggest concern is the visibility of the sidescan system. The sidescan does not give clear data for the first 30 m due to sea surface and bottom interference. For this reason, the sidescan sonar should be placed at least 30 m from the targeted area.

The second concern is the relative placement of different sonars. In the previous experiment, all the sonars were placed relatively close to each other. The topscan sonars viewed the water directly above the placement site, but the sidescan sonars viewed the water 30 m away. It would be ideal if the same bubble cloud can be concurrently viewed from two or possibly three different angles.

Finally, the third concern involves maneuverability. One of the main problems with the previous experiment was that bubble clouds were continuously carried out of view. This is particularly problematic in understanding bubble cloud formation. If the sidescan sonars can be steered in different directions and can map a volume of water, the sonars would be able to track bubble clouds through the water.

4. Conclusion

The sonar system is an accurate and versatile system. With a good setup, many aspects of bubble clouds can be accurately measured and analyzed. In this study, the intensity data in both the sidescan and topscan systems have reproduced results from which bubble cloud formation and dimension information has been derived. Although the Doppler velocity data did not result nearly as well from the available data set, we expect more reliable velocity data when the instruments are deployed in Narragansett Bay. Despite the drawbacks of the velocity data, the intensity data is very revealing and more than enough to delineate the BEAMER a welcome addition to the oceanographic equipment at Narragansett Bay.

Acknowledgments. We thank the National Science Foundation for providing the funding for this summer program. We thank Jim Miller for his useful conversations about the mechanics of bubble clouds and acoustic sensors. We would also like to thank all those from Martha's Vineyard that upkeep a great website with plenty of oceanographic and meterological data.

References

Bortkovskii, R. S., Atmosphere-Ocean Gas Exchange Due to Bubbles Generated by Wind Wave Breaking, in Gas Transfer at Water Surfaces, p.261-264, 2002.

Farmer, D.M., Breaking Waves, Bubbles, and Langmuir Circulation: a Measurement Strategy for Studying Bubble Enhanced Air-Sea Gas Transfer, in Third International Symposium on Air-Water Gas Transfer, p.297-304, 1995.

Martha's Vineyard Coastal Observatory, 2002: Oceanographic and Meterological data. Published as website. URL http://www.whoi.edu/mvco/data/data.html

Medwin, H., and Clay, C. S., Fundamentals of Acoustic Oceanography, Boston, Academic Press, p.287-347, 1998.

Melville, W.K., Terrill, E., and Ding, L., Field Measurements of Air Entrainment by Breaking Waves, in Third International Symposium on Air-Water Gas Transfer, p.285-295, 1995.

RD Instruments, Acoustic Doppler Current Profiler: Principles of Operation a Practical Primer, Tech manual, p.1-52, 1996.

Vagle, S., and Farmer, D.M., A Comparison of Four Methods for Bubble Size and Void Fraction Measurements, *IEEE Journal of Oceanic Engineering*, vol. 23, p.211-222, 1998.

Measuring enzymatic rates in subseafloor sediments

Melinda Montano[1], Bruno Soffientino, Steven D'Hondt, David Smith, and Arthur Spivack

University of Rhode Island, Graduate School of Oceanography, Narragansett, RI

Abstract. One-tenth to two-thirds of the earth's living biomass is estimated to exist in subseafloor sediments in the form of sulfate reducers, methanogens, and other microbes. Deep sediment cores reveal that microbes can live deep beneath the sediment. Current methods of measuring microbial activity are not sensitive enough at such great depths. Using a tritium-based radioassay, extremely low levels of activity can be measured. This assay targets the ubiquitous hydrogenase enzyme that can catalyze the exchange of hydrogen atoms between the pool of hydrogen in H_2O and the pool of hydrogen in H_2. We examined for the first time enzymatic activity of microbes in subseafloor sediments from cores collected on Leg 307 of the Integrated Ocean drilling Program.

1. Introduction

Little is known about the metabolic activity of microbial communities that live in subseafloor sediments (Parkes *et al.*, 1994). It is believed that 1/10 to 2/3 of the Earth's biomass is contained in the deep biosphere (Whitman et al., 1998; Parkes et al., 2000-always cite original sources if possible). Microbial cells and dissolved metabolites were found in the pore water of deep subseafloor sediments (D'Hondt et al., 2004). Traditional radiotracer methods for measuring microbial activities are not sensitive enough to detect activity in these deep sea sediments(Soffientino *et al.*, unpubl.). The goal of our work was to apply a highly sensitive, tritium-based radioassay to the deep biosphere to measure biological activity directly and routinely for the first time.

Biological activity in deep sea sediments was measured by exploiting the commonly used enzyme, Hydrogenase. Hydrogenase is expressed by any organism that either uses or produces hydrogen. This enzyme is particularly important for subseafloor microbes because many anaerobic metabolic pathways involve molecular hydrogen. Anaerobic processes such as sulfate reduction, methanogenesis, acetogenesis, and sulfate-dependent methane oxidation all require hydrogen (Schulz and Zabel, 2000). At great subseafloor depths, hydrogen might be the only available metabolic reductant (Morita, 2000-is this reference appropriate for this point?).

Hydrogenase catalyzes the splitting of molecular hydrogen according to the following equation:

$$E + H_2 \ \_\ E{:}H + H^+ \tag{1}$$

One atom of hydrogen is released into solution, the other hydrogen binds to Hydrogenase creating an enzyme/substrate complex that is used for energy. Because enzymes play a role in all biochemical reactions, it may be possible to scale the activity to overall metabolic rates.

A sensitive tritium-based radioassay was used to measure hydrogenase activity in sediment samples. Hydrogenase catalyzes an exchange between the pool of H atoms in H_2 gas and the pool of H atoms in water if there is disequilibrium between the two pools. When a radiolabel such as tritium is introduced, the radiolabel is transferred to the water:

$$HT + H_2O \ \_\ HTO + H_2 \tag{2}$$

Thus, the rate at which the tritiated gas (HT) is transferred to the water (HTO) indicates the activity of hydrogenase (Soffientino *et al.*, unpubl.). Sediment samples from the Integrated Ocean Drilling Program were examined because measurements of microbial enzymatic activity have not been taken at such depths by any other method. Also, the deep sea sediment environment lacks oxygen, where hydrogenase activity is most likely to occur.

2. Methods

2.1 Sample Preparation

We analyzed samples from five-centimeter long core sections from Integrated Ocean Drilling Program Leg 307, site 1317 (Figure 1). The samples were stored in a –80ºC freezer and thawed before analysis. Because the exposed outer edges of each section may have been exposed to drilling fluid, the outer 2 cm were chipped off and approximately 10 grams of sediment were sampled from the center of the section. A homogeneous sediment slurry was made by mixing the sediment sample with sterile seawater in a ratio of approximately 2:1. Ultrapure nitrogen was blown through the slurry to ensure anaerobic conditions.

Five milliliters of the slurry were drawn into gas tight syringes for radioassay. Prior to filling, the syringes were flushed 5 times with ultrapure nitrogen. after filling each syringe with about 5 ml of slurry, 5 ml of HT gas were introduced. Syringes were incubated on a shaker at 260 revolutions per minute for 2-3 hours. Each syringe was sub-sampled every 20 minutes, for a total of between six and nine time points. The subsamples were degassed by vortexing and vacuuming the vials twice for 20 seconds and flushing with unlabeled hydrogen for 20 seconds. The samples were then centrifuged to settle the solids and 75 µl of the supernatant from each vial were sampled for liquid scintillation counting.

---

[1] Now at Eckerd College, St. Petersburg, FL

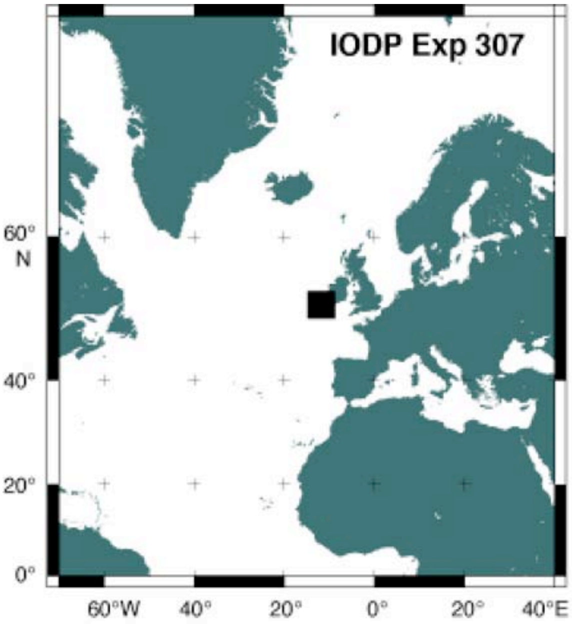

Figure 1. Location of Integrated Ocean Drilling Program Leg 307, sites 1316-1318.

2.2 Making the Headspace

The tritium gas (HT) was prepared by the method of Soffientino *et al.* (2005). A headspace apparatus was used to produce the HT gas introduced into the sample syringes (Figure 2). The apparatus consisted of a 0.6 L gas bag, the reaction vial, and the headspace syringe. Stainless steel tubing and three-way stopcocks connected the components. An oxygen trap containing palladium catalyst pellets was positioned between the gas bag and the reaction vial. A water trap with calcium sulfate was placed on the other side of the reaction vial, between the vial and the headspace syringe. Prior to making the gas, the headspace syringe and the gas bag were flushed with an H_2/N_2 mixture to remove all oxygen from the system.

A reaction vial containing 10 mCi tritiated sodium borohydride (^{3}H-BH$_4$ from Radiolabeled Chemicals, Inc.; specific activity, 15 Ci/m mol) was connected to the apparatus between the bag and the syringe. The H_2/N_2 mixture in the gas bag was used to flush the lines of the apparatus and the reaction vial prior to the reaction. The reaction vial was isolated from the gas bag and the oxygen trap during the reaction. Then HT gas was evolved by reacting tritiated sodium borohydride with 0.1 ml cobaltous chloride ($CoCl_2$). The connection between the reaction vial and the gas bag was opened and the headspace syringe was filled to 100 ml. Room temperature and pressure at the time of making the gas was recorded for later calculations (see Appendix).

2.3 Measuring headspace specific activity

Headspace specific activity was measured each time gas was evolved to standardize the enzyme rate. A known volume of gas from the headspace syringe was injected into a 30 ml vial containing air and palladium catalyst pellets. The palladium pellets catalyzed the formation of tritiated water, HTO, from oxygen and the tritiated headspace gas. Ten ml of distilled water were injected into the vial to trap and dilute the HTO. Fifty microliters of the HTO were sampled for liquid scintillation counting.

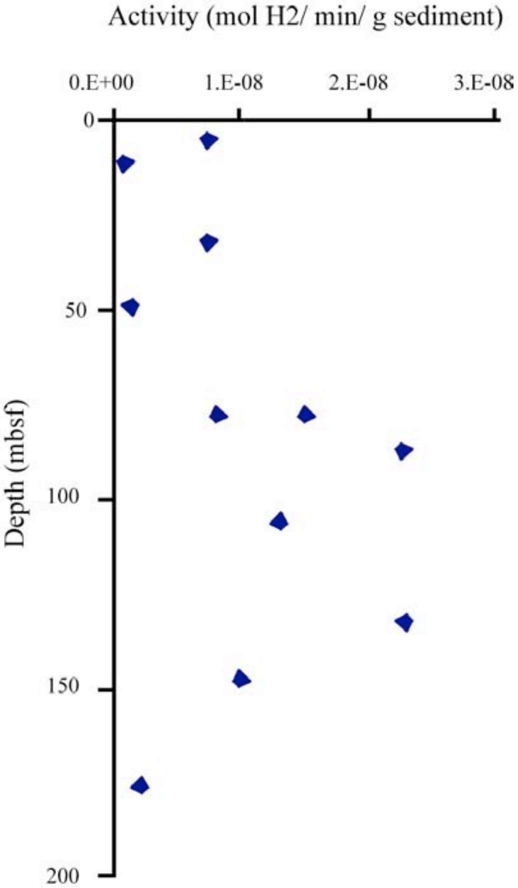

Figure 2. IODP Leg 307 Site 1317 Hydrogenase activity with depth in meters below the seafloor (mbsf). Data points standardized to specific activity show no apparent trend with depth.

2.4 Calculation of enzyme activity and data analysis

Hydrogenase enzyme activity rates were calculated from the slope of disintegrations per minute (DPM) versus incubation time per unit volume and standardized to the specific activity of the HT. Specific activity was determined by dividing the total DPMs in the HT by moles of H_2. Moles of H_2 were calculated from a modified Ideal Gas Law, $PV=nRT* 0.2004$, where P is the pressure (Pa) at the time the HT gas was made, V (L) is the total amount of hydrogen made multiplied by 0.2004 because the H_2/N_2 gas mixture is 20% hydrogen, n is the number of moles of H_2, R is the universal gas constant (8.3145 J/mol*K), and T is the room temperature (K) at the time the gas was made. Total DPMs of HT was calculated by multiplying the headspace DPMs per 50µL by 10^4µL per headspace volume and then multiplying by the total volume of HT gas made.

2.5 Preparation of the standard

Every run included as a standard an analysis of the bacterium *Clostridium pastueranium*. The standard itself consisted of a late exponential culture of *C. pasteurianum* that was aliquoted in microcentrifuge tubes and frozen at –80 °C.Each standard analysis required samples of two live syringes and a mercuric chloride killed sample. The activity of each run's standard was added to the long term standard mean. To remove variability due to day-to-day differences in assay performance, the sediment sample activity was normalized to the difference between the daily measurement and the long term mean of the standard.

3. Results

The data standardized to the specific activity displayed no apparent trend with depth in meters below the seafloor (mbsf; Figure 2). Once corrected to the difference in the daily standard and the long term standard mean, the data form a more apparent trend with depth (Figure 3). Activity remained nearly constant in the first 60 mbsf with a few outliers then increased until about 100 mbsf. Below 100 mbsf, activity decreased slightly.

The data begin to take shape when corrected for the kill control (Figure 4). The downhole trend in activity after all the corrections were made was a smooth curve, steadily increasing until about 110 mbsf. Hydrogenase activity then decreased until 170 mbsf.

4. Discussion

Peaks in activity were expected to occur in places where rates of certain metabolic processes such as sulfate reduction, methanogenesis, or sulfate-dependent methane oxidation are presumed to be highest based on the chemical profiles of the cored sediment. However, there was no definite correlation between the methane and sulfate profiles and the hydrogenase activity.

When hydrogenase activity was compared to dissolved inorganic carbon for site 1317, peaks occurred at about 130 mbsf in both profiles. Dissolved inorganic carbon includes carbonate and bicarbonate. This is of considerable interest because one of the metabolic products of sulfate reduction, methane oxidation and acetoclastic methanogenesis is bicarbonate. Therefore, net respiration may peak at about 130 mbsf.

5. Conclusion

This was the first time enzymatic activity was routinely measured in subseafloor sediments. From this work, we did observe a trend in activity with depth. However, it doesn't correlate with the chemical profiles, as expected.

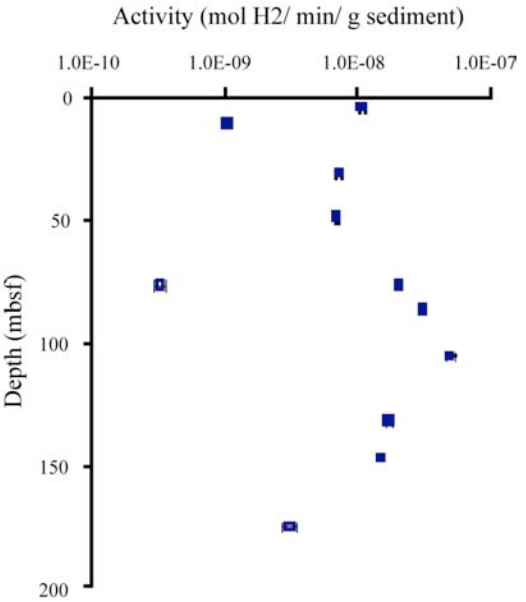

Figure 3. IODP Leg 307 Site 1317 Hydrogenase activity (± standard error) with depth. Data points standardized to specific activity and corrected to the difference in the daily standard and the long term standard mean. The curve was not entirely smooth.

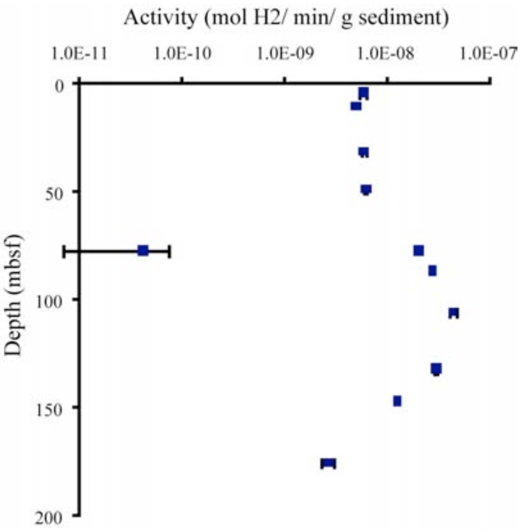

Figure 4. IODP Leg 307 Site 1317 Hydrogenase activity (± standard error) with depth. Data points standardized to specific activity, standard corrected, and kill corrected.

References

Morita, RY. 2000. "Is H_2 the universal energy source for long-term survival?" *Microbial Ecology*. Vol. 38:307-320.

Parkes, RJ, Cragg, BA, Bale, SJ, Getliff, JM Goodman, K, Rochelle, PA, Fry, JC, Weightman, AJ, and Harvey, SM. 1994. "Deep bacterial biosphere in Pacific Ocean sediments." *Nature*. Vol. 371: 410-413.

Schulz, H. D.; Zabel, M. (Eds). Marine Biogeochemistry. 455pp. Springer-Verlag, New York. 2000.

Soffientino, B, Spivack, AJ, Smith , DC, Roggenstein, EB, D'Hondt, SL. 2005. "A Versatile and sensitive tritium-based radioassay for measuring Hydrogenase activity in aquatic sediments." Submitted to Journal of Microbiological Methods.

Appendix

Calculating Headspace Specific Activity

$$\text{Moles } H_2 \text{ in headspace} = \frac{\text{pressure x volume x } 0.2004}{8314.5 \text{ J/Mol x Temperature (K)}}$$

$$\text{Total 3-H DPMs} = \frac{\text{Specific Activity (DPMs) / volume sampled x } 10^4\ \mu\text{l}}{\text{volume gas sampled from headspace (L) x total Headspace volume (L)}}$$

$$\text{Specific Activity (DPMs/ mole)} = \frac{\text{Total 3-H DPMs}}{\text{Moles } H_2 \text{ in headspace}}$$

$$\text{DPM Rate} = \frac{\text{DPMs/0.1 mL}}{\text{Time (minutes)}}$$

$$\text{Specific Activity (moles } H_2 \bullet \text{min}^{-1} \bullet \text{mL}^{-1}) = \frac{\dfrac{\text{DPM rate (dpm/min/0.1ml)}}{\text{Volume scintillations counted (mL)}}}{\text{Specific activity (DPMs/ mole)}}$$

Correcting to Specific Activity

$$\text{Volume sediment (mL)} = \frac{\text{Sediment mass}}{\text{Sediment density}}$$

$$\text{Sediment porosity} = \frac{\text{Volume water added to make slurry (mL)}}{\text{Volume sediments (mL)}}$$

Volume of solids = Volume sediment x (1- sediment porosity)

Volume of slurry water = Volume seawater + Volume sediments – Volume solids

$$\text{Hydrogenase activity (moles } H_2 \bullet \text{min}^{-1} \bullet \text{g sediment}^{-1}) = \frac{\text{Specific Activity/mL x Volume of slurry water (mL)}}{\text{Sediment mass}}$$

Long-term Standard Correction

$$\text{Correction factor} = \frac{\text{Specific Activity standard}}{\text{Long term standard average}}$$

$$\text{Long term corrected Hydrogenase activity} = \frac{\text{Hydrogenase Activity (moles } H_2 \bullet \text{min}^{-1} \bullet \text{g sediment}^{-1})}{\text{Correction Factor}}$$

Calculating Net Hydrogenase Activity

$$\text{Mercuric Chloride Dilution factor} = \frac{\text{Volume of slurry + Volume Mercuric Chloride}}{\text{Volume of slurry}}$$

$$\text{Activity of kill control} = \frac{\text{Slope of Kill control x Volume of slurry}}{\text{Sediment mass x Dilution factor}}$$

$$\text{Corrected kill control activity} = \frac{\text{Kill control activity}}{\text{Long term correction factor}}$$

Net Hydrogenase Activity = Long term corrected hydrogenase activity – long term corrected kill control activity

Table 1. Calculated Sediment Activity (mol H2/ min/g sediment)

Core Section	Depth (mbsf)	Chunk 1	Chunk 2	Uncorrected Average Activity	Standard-corrected Average Activity	Net (live-killed) Activity
1317A 1H3	4.2	2.93E-09	1.17E-08	7.32E-09	1.09E-08	5.98E-09
1317A 2H3	10.7			6.81049E-10	1.04E-09	4.99361E-09
1317A 3H3	20.2					
1317A 4H3	31.2	6.67E-09	7.77E-09	7.22E-09	7.33E-09	5.98E-09
1317A 5H3	39.2					
1317A 6H3	48.7	1.76E-10	2.43E-09	1.30E-09	7.03E-09	6.30E-09
1317A 7H3	58.2					
1317A 8H3	67.7					
1317A 9H3 (2)	77.2			1.49736E-08	2.06525E-08	2.06262E-08
1317A 9H3 (1)	77.2			7.96E-09	3.30E-10	4.19E-11
1317A 10H3	86.7			2.269E-08	3.12955E-08	2.78411E-08
1317A 11H3	96.2					
1317A 12H3	105.7			1.30E-08	5.03283E-08	4.43228E-08
1317A 13H3	115.2					
1317A 14H3	124.7					
1317A 17X3	131.97			2.27E-08	1.73898E-08	3.03947E-08
1317D 5R1	147.02			9.89E-09	1.50998E-08	1.27124E-08
1317D 9R1	175.57			2.01E-09	3.08E-09	2.72E-09

18S ribosomal RNA and *cytochrome oxidase* gene sequences of *Didemnum* sp., an invasive colonial tunicate

Argenta Price,[1] Jeremy Collie, and David Smith

Graduate School of Oceanography, University of Rhode Island, Narragansett, Rhode Island

Abstract. *Didemnum* sp. is an invasive colonial tunicate that has recently expanded rapidly on the Atlantic and Pacific coasts of North America as well as in the Netherlands and New Zealand. The tunicate attaches to hard surfaces and overgrows native fauna, causing ecological changes in areas where it becomes established. There has been controversy over the specific identity of *Didemnum* sp., and its original habitat remains unknown. The goal of this project was to sequence and compare two genes from various samples of *Didemnum* sp. to begin to clarify the phylogenic debate. To analyze the taxonomy of *Didemnum* sp. on a genetic basis, two genes were chosen for sequencing: the slowly evolving *18S rRNA* gene and the mitochondrial *cytochrome oxidase subunit 1* gene. Both have been used widely for phylogenic analysis of other organisms. Primers specific to the genes were developed from published primers and comparison of tunicate sequences available on GenBank. The primers were used for polymerase chain reaction to amplify the target genes from isolated *Didemnum* DNA, and the amplified products were sent for sequencing at the URI Genomics and Sequencing Center. Approximately 900 bp sequences of the *18S rRNA* gene were obtained from *Didemnum* sp. samples from three locations in North America and two in the Netherlands, as well as from one sample of *Diplosoma listerianum* from the Netherlands. Additionally, 600 bp of the *cytochrome oxidase* gene were sequenced from *Didemnum* sp. samples from three locations in North America. The *18S rRNA* sequences of *Didemnum* sp. from all five locations were identical, as were the *cytochrome oxidase* sequences from the three North American locations. Sequences were also compared to *Didemnum* and closely related species on GenBank. These results are consistent with the assumption that the *Didemnum* samples from North America, New Zealand, and the Netherlands are a single introduced species.

1. Introduction

In 2002 an invasive species of the colonial tunicate *Didemnum* was discovered growing on George's Bank (Figure 1). Since then, it has spread rapidly and now covers up to 50% of rocky sea floor, where it causes habitat alterations and can overgrow native benthic fauna (Bullard *et al.*, 2005; Valentine Page C. *et al.*, 2005a). The invasive species of *Didemnum* is currently located in New Zealand (Figure 2), the Netherlands, and the east and west coasts of North America. This colonial sea squirt varies in color from a very pale tan to light brownish yellow, and its morphology can range from large flat mats to hanging tendrils. The tunicate reproduces sexually by forming swimming larvae, and it can be spread over large distances by colony fragmentation which may be facilitated by human disturbances. For example, a barge in New Zealand was found encrusted with the tunicate and is blamed for the spread of *Didemnum* to the Marlborough Sounds (Coutts, 2002). *Didemnum* (like other invasive species) is threatening because it has few predators in areas where it opportunistically spreads. So far no natural predators of *Didemnum* sp. have been identified, although the common periwinkle has been found consuming dead or dying *Didemnum* in a New England tide pool (Valentine *et al.* 2005b).

The introduced species of *Didemnum* is usually referred to as *Didemnum* sp. because its identity remains unknown. The species was studied in New Zealand and identified as a new native species, named *Didemnum vestum* (Kott, 2002; Kott, 2004). The species in North America was then identified as a different species, *Didemnum vexilium* (Kott, 2004), though it has also been labeled *Didemnum lahelli* (after the *Didemnum* species found in Europe) (Bullard *et al.*, 2005). Most researchers disagree and believe that the*Didemnum* spreading in various parts of the world is most likely the same species. This debate can be clarified by genetic analysis.

Figure 1. Didemnum growing on George's Bank *Didemnum* on George's Bank forms light tan colored mats, covering rocky seafloor. Here, it is shown covering pebbles and a scallop. Photo credit Page Valentine.

---

[1] Now at Yale University, New Haven, Connecticut

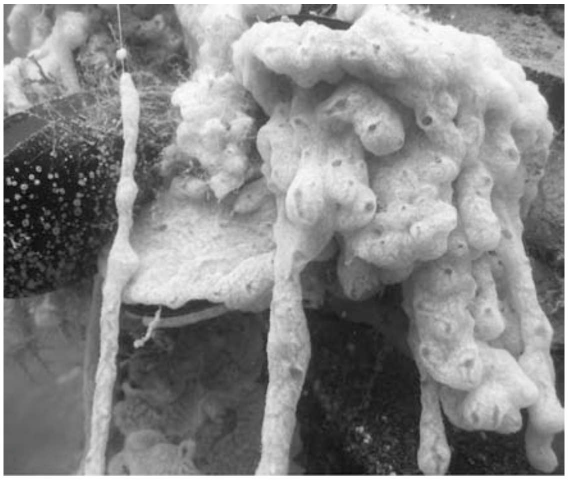

Figure2. *Didemnum* in New Zealand. *Didemnum sp.* has various growth patterns – large bubbling mats seen on Georges bank, or hanging tendrils like those seen here growing off of mussels. Photo credit Paul Barter

Genetic analysis has been used to explain phylogenic relationships between many other species (Bernston *et al.*; 1999; Herbert *et al.*, 2003; Stach *et al.* 2002). The same gene from a variety of organisms is sequenced, and the sequences are compared with computer programs to determine the genetic relationships between species. Two genes have been commonly used to construct eukaryotic phylogenies: the *18S ribosomal RNA* gene and the mitochondrial *cytochrome oxidase* subunit 1 gene. The *18S rRNA* gene evolves very slowly and primers can be developed from distantly related species that will anneal to and amplify portions of the gene in a wide range of organisms. This gene is good for constructing phylogenies from a wide range of phylogenic levels (from family to phylum). The *cytochrome oxidase* gene evolves more quickly, so greater difference appears in the sequences of closely related (ie same genus or family) species. However, universal primers have been published (Folmer *et al.*, 1994) to amplify a portion of the gene, so sequences can be obtained from previously unstudied species such as *Didemnum*. Relationships between organisms can be determined by comparison of these gene sequences combined with analysis of morphological characteristics.

The goal of this project was to sequence the *18S rRNA* and *cytochrome oxidase* genes from the *Didemnum* species growing on George's Bank, two other locations off the east coast of North America, and two locations in the Netherlands. These sequences were compared to determine their level of genetic relatedness. The *18S* gene was chosen as the primary target for sequencing because three *18S* sequences of *Didemnum* from New Zealand were available online (GenBank: http://www.ncbi.nlm.nih.gov/entrez/). The *cytochrome oxidase* gene was chosen as a secondary target because of concerns about the ability of the *18S* gene to resolve species-level differences (Xia *et al.*, 2003). Very little sequencing of *Didemnum* has been done, so this is novel work intended to expand available information about *Didemnum* and to help answer the taxonomic questions.

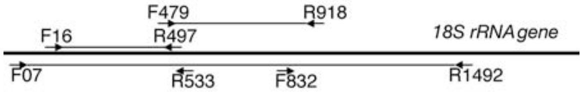

Figure 3. Position of primers relative to the *18S rRNA* gene. Primers F07 and F16 do not overlap because the numbering was based on different organisms. F497 is essentially the reverse compliment of F479.

2. Methods

2.1. DNA isolation

DNA was isolated from ethanol preserved samples of *Didemnum* from George's Bank (collected in 2004 by Jeremy Collie), a tide pool on Cape Cod (collected by Page Valentine), and two locations in the Netherlands (collected in 2003 by Adriaan Gittenberger). Fresh samples of *Didemnum* and *Botrylloides* (for comparison) from Narragansett Bay (the dock at the Graduate School of Oceanography) were also collected. For comparison, an ethanol preserved sample of *Diplosoma listerianum* from the Netherlands was provided by Adrian Gittenberger. DNA was isolated from 25-40 mg sample using the MOBio Ultra Clean Tissue DNA isolation kit. The recommended protocol was followed, except typically 600 ul solution TD1 (instead of the recommended 45 0ul) was added to the bead solution after vortexing to thin out viscous solution. DNA was eluted from the spin column in 60 ul of solution TD3.

2.2. Primer design

Primers for the *18S rRNA* gene were designed by comparison of sequences in the Didemnidae family. A consensus sequence was generated from the three available sequences of *Didemnum* sp. (Mahanga Bay, USA, and Whangamata) and submitted to IDT's Primerquest Program (www.idtdna.com). Two primer sets were ordered based on these consensus sequences: F16 with R497, and F476 with R917. (Numbers correspond to their position in the consensus sequence from the three sequences.) These two primer sets were used to amplify about 900 bases near the 5'end of the *18S rRNA* gene. Vicki Webb provided sequences for primers F07 and R1492 to amplify a larger portion of the gene (Numbering system is not the same as the one for the previously mentioned primers). Primers F833 and R532 were designed to sequence internal portions of the gene. They were designed from preliminary sequences using F476 and R917 on a *Didemnum* sample from the Narragansett Bay. The relative positions of the *18S* primers are shown in Figure 3.

To amplify a 658 bp portion of the *cytochrome oxidase* gene, sequences for universal primers LCO1490 and HCO2198 were obtained from www.barcodinglife.com (Folmer *et al.* 1994). Table 1 shows all of the primer sequences.

2.3. PCR amplification

Fragments of the *18S rRNA* and *cytochrome oxidase* genes were amplified using polymerase chain reaction. The Taq PCR core kit from Promega was used. Each 50 ul reaction contained: 1x Taq PCR buffer, 1.6 units Taq DNA polymerase, and 1 ul (200 uM final concentration) dNTP mix. Primer concentrations, magnesium chloride concentrations, and amount of template DNA varied depending on primer set: primers F16 and R497: 0.5 uM primer, 2.5 mM $MgCl_2$, 100 ng template; primers F476 and R917: 1 uM primer, 1.5 mM $MgCl_2$, and 200 ng template DNA; primers F07 and R1492: 0.5 uM primer, 1.5 mM $MgCl_2$, and 200 ng template; primers LCO1490 and HCO2198: 0.2 uM primer, 3.5 mM $MgCl_2$, and 100 ng template.

The PCR program for primers F15 and R497 and F476 and R917 was: 94ºC for 3min, then 30 cycles of 94ºC for 45seconds, 55ºC for 30 seconds, 72ºC for 1minute, ending with a final polymerization of 72ºC for 10minutes. For primers F07 and R1492, the cycles were: 94ºC for 3 min, then 35 cycles of 94ºC for 30seconds, 50ºC for 30 seconds, 72ºC for 1.5minutes, ending with a final polymerization at 72ºC for 10 minutes. The protocol for primers LCO1490 and HCO2198 was: 94ºC for 3 min, then 35 cycles of: 94ºC for 30 seconds, 45ºC for 30 seconds, 72ºC for 1.5 min, ending with a final polymerization at 72ºC for 10 minutes.

The PCR products were run on a 2% agarose gel (at 125 volts) to check success of the PCR reaction. Successful reactions were then cleaned up using the Qiagen Qiaquick PCR purification kit. The recommended protocol was followed, plus an extra wash with 250ul buffer PE. DNA was eluted with 50ul of buffer EB (Tris-Cl, pH 8.5).

Table 1: Primer Sequences

Primer	Primer Sequence	Gene
F16	AAGCCATGCAAGTGCAAGTACGAG	*18S rRNA* forward
R497	CTGAAATGGGTAATTTGCGCGCCT	*18S rRNA* reverse
F476	GCGCGCAAATTACCCATTTCAGAC	*18S rRNA* forward
R917	AACGACTCTCGACGTGCAACTT	*18S rRNA* reverse
F07	ACCTGGTTGATCCTGCCAG	*18S rRNA* forward
R1492	TACGGYTACCTTGTTACGACTT	*18S rRNA* reverse
F833	GCGTTCGTTCGGGTCCTTTGTAG	*18S rRNA* forward
R532	CGGCATCGGTATTTCTCGTCACTA	*18S rRNA* reverse
LCO1490	GGTCAACAAATCATAAAGATATTGG	*Cytochrome oxidase* forward
HCO2198	TAAACTTCAGGGTGACCAAAAAATCA	*Cytochrome oxidase* reverse

2.4. Sequencing

Purified PCR products were quantified using UV spectroscopy and were sent for sequencing at URI's Genomics and Sequencing Center on a CEQ 8000 sequencer. 2ul of 10nM primer was sent with 10ul template solution containing 50fmol PCR product DNA in Tris-Cl, pH 8.5.

2.5. Data analysis/alignment

Forward and reverse sequences were compared and errors in the sequencing corrected by eye through comparison of the spectral peaks from the sequencer output. Sequences from different samples were then aligned using the ClustalW program. Aligned sequences were compared using the program Mega3 (Kumar, Tamura, Nei 2004). Sequences were also aligned with various related sequences from GenBank. To compute relative genetic distances between sequences, pairwise p-distances (with pairwise deletion of gaps) were computed using Mega3.

3. Results

About 900 bases of the *18S rRNA* gene were sequenced from all samples. All five *Didemnum* samples yielded identical sequences, which were different than the *Diplosoma listerianum* sequence. The sequences were aligned using ClustalW (Figure 4).

About 600 bases of the *cytochrome oxidase* subunit 1 gene were sequenced for samples from George's Bank, the Cape Cod tide pool, and the Narragansett Bay. All three sequences were identical. The sequence from George's Bank is shown in Figure 5.

The sequencing of the *18S rRNA* gene using primers F07 and R1492 did not work, possibly because of problems with primer specificity. PCR amplification was successful, but neither the PCR primers nor the internal sequencing primers yielded strong enough fluorescent signals. PCR amplification was also successful for the *cytochrome oxidase* gene. However, sequences of samples from the Netherlands and some sequences from North American samples showed extensive peak overlap, probably caused by impure template or primer slippage. Table 2 is a summary of which sequences were attempted and how many times each was sequenced successfully.

3.1. Repeatability of results

The entire PCR and sequencing process was conducted in duplicate for all samples, and each sample was sequenced with forward and reverse primers. However, because of problems with primer specificity/slippage, template quality, and time constraints, successful sequences were not always obtained. The *18S* gene was only sequenced once from the *Diplosoma* and the Cape Cod tide pool samples. The *cytochrome oxidase* sequencing was only successful for three samples, and only the Cape Cod tide pool sequence was obtained more than once.

3.2. Alignment and analysis

Sequences were aligned using the ClustalW algorithm. Mega3 was used to compare sequences: pairwise p-distances were computed using the pairwise deletion option to deal with gaps in the sequences. For the *18S rRNA* gene, the *Didemnum* sequences from all five sites were identical, but differed from the *Diplosoma* sequence by 11%. A sample of *Botrylloides* (different order than *Didemnum*) from the Narragansett bay, was also sequenced – it differed from *Didemnum* by 19%. The *18S* sequences were also compared to *Didemnum* sequences available on GenBank. The sequences from Whangamata (New Zealand), and the US were identical to the *Didemnum* samples sequenced in this project. The sequence from Mahanga Bay, New Zealand differed by 8% (but only by 3.6% if the distance was computed by the complete deletion of gaps method). A sequence of *Didemnum candidum* was also available online, but the genetic distance was much higher than expected - 24%, possibly due to misalignment, so the reliability of this sequence is uncertain (Table 3). The three *cytochrome oxidase* sequences were also identical. The sequences were compared to the *Didemnum candidum* sequence on GenBank as well as to sequences of two other species in the Didemnidae family. The *Didemnum* samples differ by 35-38% from sequences of species in the same family and by an unexpected 45% from *Didemnum candidum* (again, the reliability of this sequence is unclear) (Table 4).

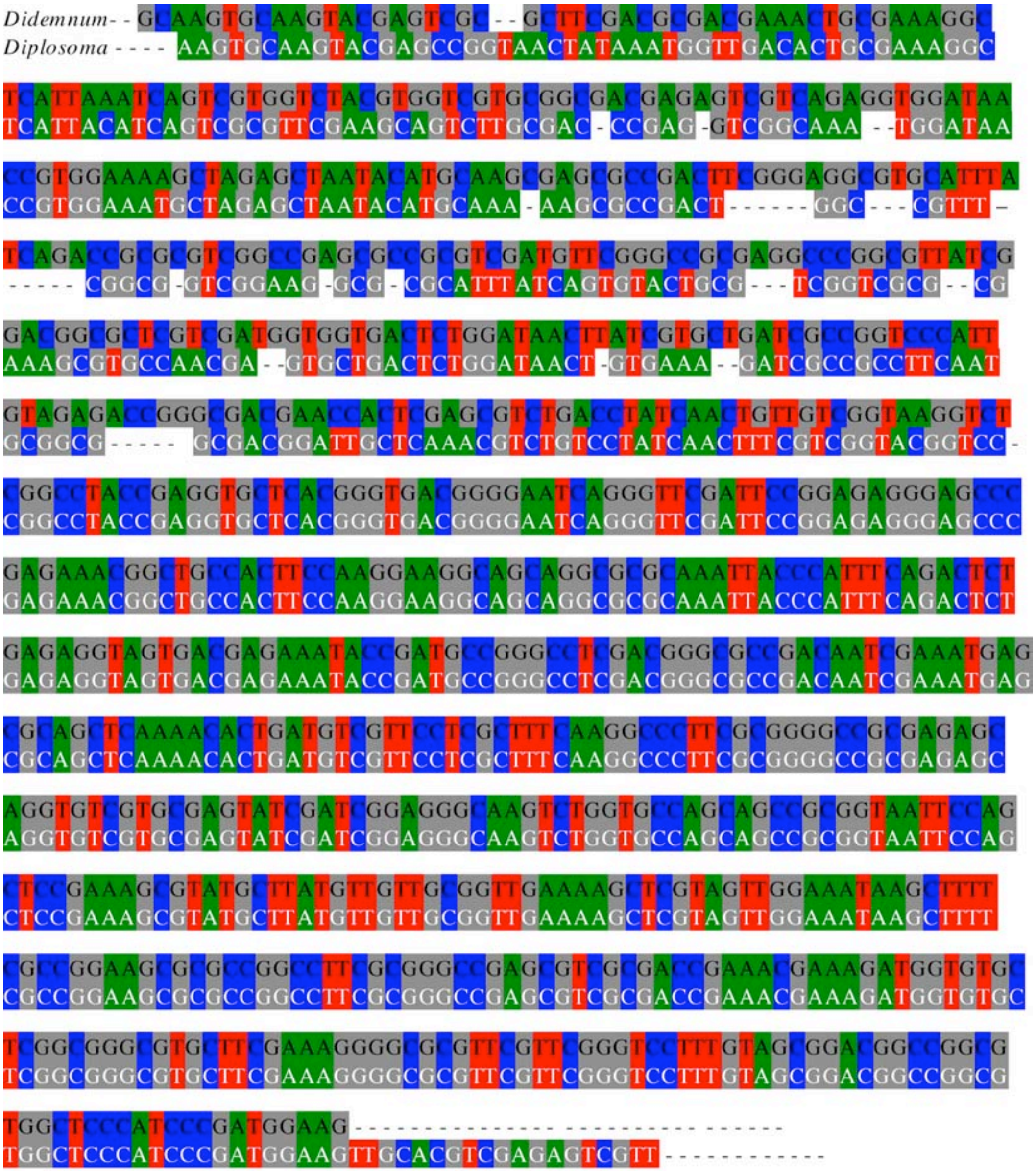

```
Didemnum- - GCAAGTGCAAGTACGAGTCGC - - GCTTCGACGCGACGAAACTGCGAAAGGC
Diplosoma - - - - AAGTGCAAGTACGAGCCGGTAACTATAAATGGTTGACACTGCGAAAGGC

TCATTAAATCAGTCGTGGTCTACGTGGTCGTGCGGCGACGAGAGTCGTCAGAGGTGGATAA
TCATTACATCAGTCGCGTTCGAAGCAGTCTTGCGAC - CCGAG -GTCGGCAAA - -TGGATAA

CCGTGGAAAAGCTAGAGCTAATACATGCAAGCGAGCGCCGACTTCGGGAGGCGTGCATTTA
CCGTGGAAATGCTAGAGCTAATACATGCAAA - AAGCGCCGACT - - - - - - GGC - - - CGTTT –

TCAGACCGCGCGTCGGCCGAGCGCCGCGTCGATGTTCGGGCCGCGAGGCCCGGCGTTATCG
 - - - - - CGGCG -GTCGGAAG -GCG - CGCATTTATCAGTGTACTGCG - - - TCGGTCGCG - - CG

GACGGCGCTCGTCGATGGTGGTGACTCTGGATAACTTATCGTGCTGATCGCCGGTCCCATT
AAAGCGTGCCAACGA - -GTGCTGACTCTGGATAACT -GTGAAA - -GATCGCCGCCTTCAAT

GTAGAGACCGGGCGACGAACCACTCGAGCGTCTGACCTATCAACTGTTGTCGGTAAGGTCT
GCGGCG - - - - - GCGACGGATTGCTCAAACGTCTGTCCTATCAACTTTCGTCGGTACGGTCC -

CGGCCTACCGAGGTGCTCACGGGTGACGGGGAATCAGGGTTCGATTCCGGAGAGGGAGCCC
CGGCCTACCGAGGTGCTCACGGGTGACGGGGAATCAGGGTTCGATTCCGGAGAGGGAGCCC

GAGAAACGGCTGCCACTTCCAAGGAAGGCAGCAGGCGCGCAAATTACCCATTTCAGACTCT
GAGAAACGGCTGCCACTTCCAAGGAAGGCAGCAGGCGCGCAAATTACCCATTTCAGACTCT

GAGAGGTAGTGACGAGAAATACCGATGCCGGGCCTCGACGGGCGCCGACAATCGAAATGAG
GAGAGGTAGTGACGAGAAATACCGATGCCGGGCCTCGACGGGCGCCGACAATCGAAATGAG

CGCAGCTCAAAACACTGATGTCGTTCCTCGCTTTCAAGGCCCTTCGCGGGGCCGCGAGAGC
CGCAGCTCAAAACACTGATGTCGTTCCTCGCTTTCAAGGCCCTTCGCGGGGCCGCGAGAGC

AGGTGTCGTGCGAGTATCGATCGGAGGGCAAGTCTGGTGCCAGCAGCCGCGGTAATTCCAG
AGGTGTCGTGCGAGTATCGATCGGAGGGCAAGTCTGGTGCCAGCAGCCGCGGTAATTCCAG

CTCCGAAAGCGTATGCTTATGTTGTTGCGGTTGAAAAGCTCGTAGTTGGAAATAAGCTTTT
CTCCGAAAGCGTATGCTTATGTTGTTGCGGTTGAAAAGCTCGTAGTTGGAAATAAGCTTTT

CGCCGGAAGCGCGCCGGCCTTCGCGGGCCGAGCGTCGCGACCGAAACGAAAGATGGTGTGC
CGCCGGAAGCGCGCCGGCCTTCGCGGGCCGAGCGTCGCGACCGAAACGAAAGATGGTGTGC

TCGGCGGGCGTGCTTCGAAAGGGGCGCGTTCGTTCGGGTCCTTTGTAGCGGACGGCCGGCG
TCGGCGGGCGTGCTTCGAAAGGGGCGCGTTCGTTCGGGTCCTTTGTAGCGGACGGCCGGCG

TGGCTCCCATCCCGATGGAAG - - - - - - - - - - - - - - - - - - - - - - - - - - - - - - - - - - - -
TGGCTCCCATCCCGATGGAAGTTGCACGTCGAGAGTCGTT - - - - - - - - - - - - -
```

Figure 4. 18S rRNA sequences of Didemnum from George's Bank aligned with Diplosoma listerianum 18S sequences are the combined sequences of primers F16-R497 and F476-R917. Sequences were aligned using ClustalW in Mega3 with default parameters. The George's Bank sequence is in black lettering while the Diplosoma sequence is in white. The other four Didemnum samples sequenced had sequences identical to the George's Bank sample.

TAGG AAC TGC TTT TTC AGT TTT AA TAAG ATT AGA ACT TAG TGG GCC TGG TGTA CAA TTT AT TGGA AAC AAT CAA TTA
TACA ATA GTA TTG TAA CAGC TCA TGC CAT CTT AA TGAT ATTTT TTA TGG TTA TGC CTG CTTTA ATC GGAG GAT TTGG
TAAT TTC TTAAT GCC TTT AAT GGT TGG AGGT CCTGAT ATG GCA TTC CCT AGA TTA AAT AAT ATT AGT TTC TGA TTA TT
ACCA CCT AGT TTA ATA CTA TTA GTG TTA TCT GCT TGTAT AGAA GGT GGAG TAG GTA CAG GTT GAAC TCTTT ATC CTC
CTCT ATC AGG TTT ACA AAG CCA TAGT GGA CCA AGTG TAG ATTTAG CTA TCTTT GCT TTA CAT TTATC AGGG GTA AGT
AGTT TAT TAG GTG CAG TAAA CTTTA TAA CTA CTA TTG CTA ATA TGA GAAC TCC AGG TAT AAGA TTACA TAAA TTAA
CTTTAT TTG GAT GAGC AGT TGT TATAAC AGC TAT ATT ATTAT TAT TAT CAT TAC CTG TTTTAG CTG GAG GTA TTA CTA
TGAT TTTAAC AGA TAG AAAT TTTAA TAC TTC TTTCT TG

Figure 5. Cytochrome oxidase sequence of Didemnum from George's Bank. Cytochrome oxidase sequence of George's Bank sample between primers LCO1490 and HCO2198. The sequences from Narragansett Bay and Cape Cod were identical to the George's Bank sequence.

Table 2: Summary of sequences attempted and obtained

Sample	Number of times sequenced *18S* part 1 (F16 - R497)	*18S* part 2 (F476-R917)	*18S* larger portion (F07-R1492, and internal primers)	18S portion using internal primer for PCR (F07-R533)	*Cytochrome Oxidase* (LCO1490-HCO2198)
George's Bank	2	2	0	0	1
Narragansett Bay (GSO dock)	3	4	0	1	1
Tide Pool on Cape Cod	1	1	0	0	2
Grevelingen, the Netherlands	2	2	0	0	0
Oosterschelde, the Netherlands	2	2	0	0	0
Diplosoma listerianum, the Netherlands	1	1 (?)	0	0	0
Botrylloides, Narragansett Bay (GSO dock)	1	0	0	0	0

Table 3: *18S rRNA* gene sequence pairwise p-distances calculated by Mega3

	1	**2**	**3**	**4**	**5**	**6**	**7**	**8**	**9**	**10**
1. Cape Cod tide pool										
2. George's Bank	0.000									
3. Narragansett Bay (GSO)	0.000	0.000								
4. Netherlands, Grevelingen	0.000	0.000	0.000							
5. Netherlands, Oosterschelde	0.000	0.000	0.000	0.000						
6. *Whangamata*, New Zealand (GenBank)	0.000	0.000	0.000	0.003	0.003					
7. North America (GenBank)	0.003	0.003	0.003	0.007	0.007	0.004				
8. Mahanga Bay, New Zealand (GenBank)	0.080	0.081	0.080	0.082	0.082	0.078	0.081			
9. *Diplosoma listerianum*, Netherlands	0.107	0.109	0.108	0.108	0.108	0.107	0.111	0.155		
10. *Didemnum candidum* (GenBank)	0.372	0.362	0.372	0.372	0.372	0.588	0.381	0.398	0.397	
11. *Botrylloides*, Narragansett Bay	0.189	0.189	0.191	0.189	0.189	0.189	0.189	0.189	0.254	0.136

4. Discussion

All five *Didemnum* samples have identical sequences for the 900 base portion of the *18S* gene, and the three samples from North America have identical *cytochrome oxidase* sequences. These results suggest that the invasive *Didemnum* species living in North America and in the Netherlands are the same species. These sequences were compared to the three *Didemnum* sequences available on GenBank, and the samples from this project had identical sequences to the sample from Whangamata, New Zealand, which suggests that the species living in New Zealand is also the same species. However, the sequence from Mahanga Bay, New Zealand differed from the new sequences by 8%. This may indicate that this is another species of *Didemnum*, but it is unclear whether or not this small genetic distance is significant.

Because the *18S rRNA* gene evolves very slowly, it is unlikely that species from the same genus will have many differences in their *18S* sequences. To determine if some differences will occur, *Diplosoma listerianum* (from the same family as *Didemnum*) was sequenced. The two sequences differed by 11%. This shows that variation is present between species of the same family. However, first 450 bases (sequenced with primers F16, R496) differed by 21% from the *Didemnum* sequences while the second half (sequenced with primers F476, R917) was identical to *Didemnum*. The two pieces of the *Diplosoma* gene were only sequenced once, so it is possible that the identical fragment was a mislabeled sample of *Didemnum* DNA, or the significantly different fragment could have been caused by contamination. The *Diplosoma* sample should be sequenced again to resolve this. Additioanlly, the goal of this project was to examine differences between species, so in order to determine whether or not the *18S* gene can resolve species level differences, several known species from the genus *Didemnum* should be sequenced and compared. Determining the sequences of known species will also help identify the species to which the introduced *Didemnum* is most closely related, providing clues to its location of origin.

The *cytochrome oxidase* gene proved tricky to sequence. PCR amplification was successful for all of the samples and resulted in single bands around 700 bp in size. However, most of the sequencing results had significant peak overlap and were not interpretable. This type of result is usually indicative of impure template or poor primer specificity (Paul Johnson, pers. comm..). There are a few possible explanations for the problem. First, the primers were universal primers which were supposed to amplify the gene in all Eukaryotes. This means that if the *Didemnum* samples contained DNA from any other Eukaryotes (for example, something the colonies were growing on that could not be separated from the sample prior to DNA extraction), the *cytochrome oxidase* gene from the contaminating DNA would also be amplified. The sequencer would then try to interpret multiple sequences at once, causing peak overlap. A second explanation could be the primers did not bind well to the target portions of the gene. Instead, they may have slipped around in the PCR reaction, creating roughly 700 bp products with slightly different start points. The shifts in reading frame for the sequencer would cause confusion and peak overlap. Luckily some of the sequences did run successfully, perhaps because in those samples the concentration of contaminating or frame-shifted PCR product was somehow lower. Only the Tide Pool sample was successful both times the *cytochrome oxidase* gene was sequenced.

18S rRNA Primers F07 and R1492 as well as the internal primers for sequencing (R532, F833, F476, and R917) were unsuccessful. The sequences had high fluorescence at the start, but then no interpretable sequence after that. This type of output is often indicative of poor primer binding or possibly impure template. Template impurities would have been caused by problems similar to the ones encountered with the *cytochrome oxidase* sequencing. Poor primer binding would have resulted if the primers had too many bases different than their target sequences and therefore could not bind reliably. They may have needed different conditions for the PCR used for sequencing – such as a lower annealing temperature or more MgCl2 to facilitate primer binding.

The complications with sequencing both genes should be solved by cloning the PCR products into bacterial plasmids. Only one replicated gene fragment would be incorporated into each plasmid, and the plasmid would then be grown up/copied in a bacterial culture and purified. The gene could be sequenced from the pure plasmid preparations. This would improve template quality by ensuring that the plasmids contained exactly identical fragments of gene product – no frame differences or contaminating genes. Multiple plasmid preparations would have to be sequenced to make sure some of them contained the desired *Didemnum* insert.

The sequences were aligned using ClustalW and were compared with Mega3. When only the sequences obtained in this project and the online sequences of *Didemnum* were compared, the results made sense – the *Didemnum* samples from various places in the world appeared to be the same as each other but different than closely related species. However, when sequences from more distantly related species (same order) were obtained from GenBank and compared, the results became more confusing. Mega3 was used to create a neighbor-joining tree of the sequences. The samples sequenced in this project and the three previously published *Didemnum* sequences group together, while all of the other species (including ones in the same suborder as *Didemnum*) grouped in a distinctly different branch of the tree (Figure 6). Similar results occurred with the *cytochrome oxidase* gene (Data not shown).

One explanation for this confusing result could be that the genes were not aligned properly. The ClustalW algorithm places a strong penalty on opening and extending gaps in sequences, but the *Didemnum 18S* gene has frequent insertions and deletions (Communication with Vicky Webb), so this might have caused the sequences to align poorly. Therefore,

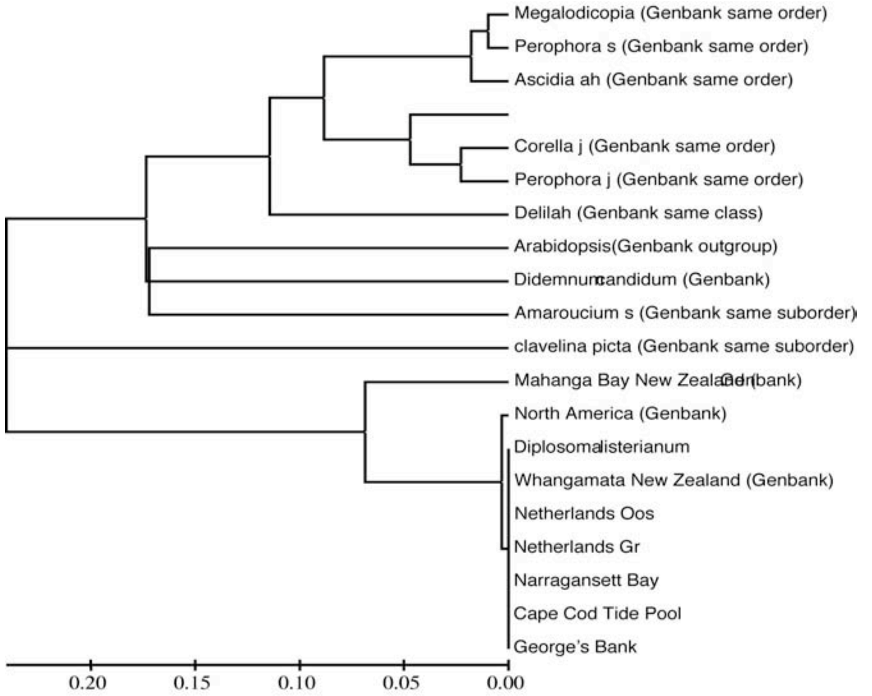

Figure 6. Neighbor-joining tree based on 18S gene from samples and sequences on GenBank Linearized neighbor-joining tree constructed with Mega3, based on p-distances between the 18S rRNA gene sequences. The Didemnum samples from this project group together at the bottom of the tree, branching off very early from the other tunicates which form their own group. Note that Arabidopsis appears more closely related (than Didemnum) to the other tunicates.

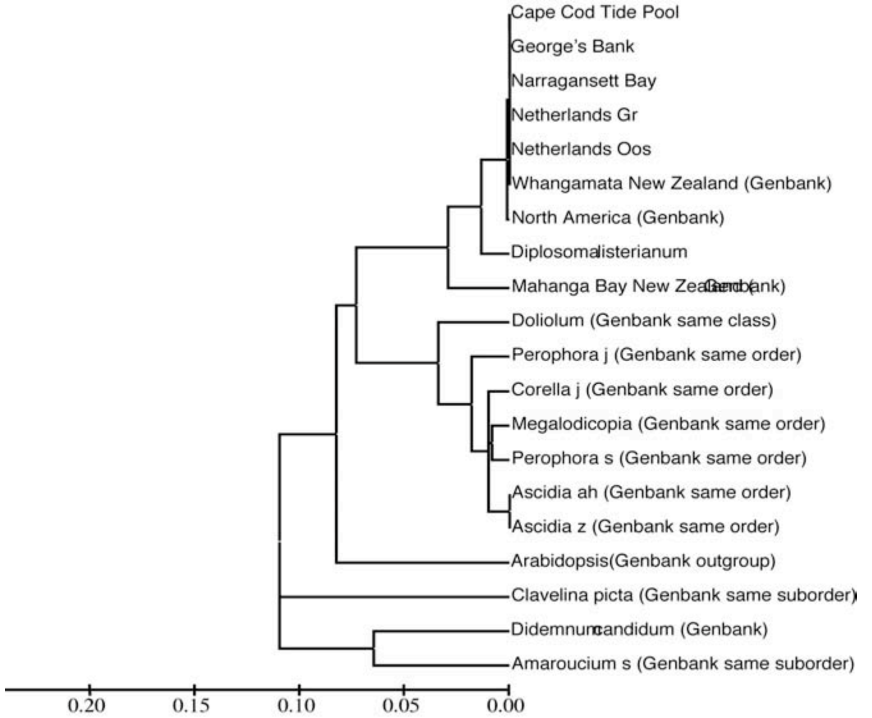

Figure 7. Neighbor-joining tree of Didemnum and related species, based on central 400bp of 18S gene. Linearized neighbor-joining tree constructed with Mega3, based on p-distances between the central 400 bases of the 18S rRNA gene sequences. To improve alignment, the sequences were first aligned according to the position of primer F476 then aligned using ClustalW. The 400 bases around the primer aligned most well, so only that portion of the gene was used to construct the tree. Note that Arabidopsis now branches off early and the Didemnum sequences from this project (top of figure) now group more closely with other tunicates, although they still form their own branch. Didemnum candidum, Clavelina picta, and Amaroucium s. do not fit well into the tree, probably still due to problems with alignment.

distances between *Didemnum* species and species from the same order are probably not as large as calculated and the tree should be less disjointed. When sequences were aligned by eye to make primer F476 line up and then aligned with Clustal, the 400 bases around the primer seemed better aligned. A tree was generated using only these 400 bases, and the *Didemnum* sequences grouped closer to the other tunicates. However, three sequences did not seem to fit well into the tree (Figure 7). Further analysis and more phylogenic expertise would be required to fully resolve this. However, for the purpose of comparing closely related species of *Didemnum*, the sequences are able to align, so the results of this project are still valid.

5. Conclusions

The results of this experiment show that the *18S rRNA* gene from the invasive species of *Didemnum* is identical or very similar in samples from North America, the Netherlands, and New Zealand. This strongly suggests that these species are indeed the same species. This supports conclusions based on morphological analysis which suggests that the species are the same. Furthermore, the *cytochrome oxidase* sequences of the three samples from North America are identical, which more conclusively indicates that the *Didemnum* growing on George's Bank is the same species as the *Didemnum* invading other parts of the Atlantic coast.

Future work is necessary to draw more certain conclusions. First, a larger portion of the *18S rRNA* gene should be sequenced, and the *cytochrome* oxidae gene needs to be sequenced for all samples. The larger portion of the *18S* gene would provide more bases for comparison and allow for more differences between species to appear. The *cytochrome oxidase* sequences would provide a more conclusive test of variation at the species level. Both of these sequences should be easier to obtain if the PCR products are cloned into plasmids before being sequenced, and if possible, DNA should be isolated from samples of tunicate larvae to avoid potential contamination. Second, several known species of *Didemnum* should be sequenced to determine the usefulness of using the *18S rRNA* gene for investigating differences at the species level. At this point, scientists believe that the *18S* gene can not be used to analyze the taxonomy of such closely related species. Sequencing known species of *Didemnum* would determine whether species level comparisons based on the *18S* gene are possible for these tunicates, and would also provide clues to determine the known species to which the invasive *Didemnum* is most closely related. That answer will help pinpoint the location from where *Didemnum* sp. was first introduced. Finally, computer analysis should be continued and parameters for alignment and distance calculation changed to attempt to understand and resolve the unexpected phylogenic separation between *Didemnum* and other tunicates.

Acknowledgments. I thank Vicky Webb for her help with primer sequences for the *18S rRNA* gene, Adriaan Gittenberger for sending samples of *Didemnum* and *Diplosoma* from the Netherlands, and Marek Kirs for helping in the lab. I would also like to thank Rob Pockalany and the Univedsity of Rhode Island, Graduate School of Oceanography SURFO program. This project was made possible by grants from the NSF-REU program and the National College Seagrant program.

Argenta M. Price, Jeremy Collie, and David Smith, Graduate School of Oceanography, Univeristy of Rhode Island, Narragansett, RI 02882. (argenta.price@yale.edu, jcollie@gso.uri.edu)

References

Berntson, E. A., S. C. France and L. S. Mullineaux. (1999) Phylogenetic Relationships within the Class Anthozoa (Phylum Cnidaria) Based on Nuclear *18S rDNA* Sequence Information. Molecular Phylogenetics and Evolution 13(2): 417-433.

Bullard, S. G., et al. (2005) Distribution and ecology of the invasive colonial ascidian Ddiemnum cf. lahillei on the east and west coasts of the United States. (not yet published)

Coutts, Ashley D.M. (2002) A biosecurity investigation of a barge in the Marlborough Sounds. Cawthron Report No. 744

Folmer, O. et al., 1994. DNA primers for amplification of mitochondrial *cytochrome c oxidase* subunit I from diverse metazoan invertebrates. Molecular Marine Biology and Biotechnology. 3, 294-297.

Herbert, Paul D.N., Ratnasingham, S., DeWaard, J.R. (2003) Barcoding animal life: *cytochrome c oxidase* subunit 1 divergences among closely related species. Proceedings of the Royal Society of London (suppl.) 270, S96-S99.

Kott, P. (2002) A complex didemnid ascidian from Whangamata, New Zealand. J. of the Marine Biological Association of the United Kingdom v. 82. pp 635-628.

Kott, Patricia. (2004) A new species of *Didemnum* (Ascidiacea, Tunicata) from the Atlantic coast of North America. Zootaxa 732: 1-10;

Kumar S., K Tamura, and M Nei. (2004) MEGA3: Integrated software for Molecular Evolutionary Genetics Analysis and sequence alignment. Briefings in Bioinformatics 5:150-163.

Lambert, C. C. and Lambert, G. (2003). Persistence and differential distribution of nonindigenous ascidians in harbors of the Southern California Bight. Mar. Ecol. Prog. Ser. 259: 145-161.

Stach, T.; Turbeville, JM. (2002). Phylogeny of Tunicata inferred from molecular and morphological characters. Molecular Phylogenies and Evolution 25 408-428.

Valentine, P. et al. (2005a). The invasive tunicate *Didemnum* sp. on George's Bank – ecological observations and potential effects on groundfish and scallop fisheries. International Invasive Sea Squirt Conference, Woods Hole.

Valentine, P. et al., (2005b) Ecological observations of the colonial tunicate *Didemnum* sp. in a New England tide pool habitat and strategies for managing invasive colonial ascidian species. International Invasive Sea Squirt Conference, Woods Hole

Xia, X., Xie, Z.; Kjer, K. M. (2003) *18S Ribosomal RNA* and Tetrapod Phylogeny. Systematic Biology. 53(3): 283-295.

Marine nuisance species genus *Didemnum*. USGS woods hole science center. http://woodshole.er.usgs.gov/project-pages/stellwagen/*Didemnum*/

Abstracts and posters from the International Invasive Sea Squirt Conference at Woods Hole. http://www.whoi.edu/institutes/oli/activities/seasquirt-program.html 2005.

Barcodinglife initiative www.barcodinglife.com

GenBank database of nucleotide sequences http://www.ncbi.nlm.nih.gov/entrez/query.fcgi?db=taxonomy Integrated DNA technologies www.idtdna.com

Dipping magnetic reversal boundary on south wall of Endeavor Deep: Implications for ocean crust formation

Amanda Shields[1] and Rob Pockalny

Graduate School of Oceanography, University of Rhode Island, Narragansett, Rhode Island

Abstract. Recent studies using magnetic data predict a complex pattern of sloping reversal boundaries within a vertical section of oceanic crust. Within the model, the top extrusive layers start with a shallow dip toward the ridge axis and steepen with depth while dyke layers dip away from the axis and remain rather steep. Endeavor Deep offers an ideal location to study "normal" oceanic crust to test this model. Forward modeling was performed with the anomalous magnetic intensity for multiple vertical and horizontal transects along an exposure of upper crust to locate areas of polarity reversals or changes in magnetic intensity. The resulting models were then projected back onto the scarp for correlating and mapping purposes where a distinctive dipping top reversal boundary is present. This boundary can be correlated to magnetic anomaly 2a as mapped on the sea-surface. This boundary begins dipping shallowly at 16˚ and gradually increases to 23˚. Two more reversal boundaries are mapped with dips of 5˚ and 3˚, but are best interpreted as later stage intrusions from off-axis volcanism.

1. Introduction

Recently proposed models of crustal accretion at intermediate to fast spreading rates suggest the entire upper crustal section of the seafloor is created within a few kilometers of the ridge axis. These models are based on evidence of volcanic flows up to four kilometers off-axis [Macdonald et al. 1996], rapid thickening of seismic layer 2a [Christeson et al., 1994], and evidence of flows and dykes rotated back toward the ridge axis [Tivey 1996, 1998]. All of these factors predict a complex pattern of sloping reversal boundaries within a vertical section of oceanic crust. Top extrusive layers start shallow and steepen as they dip toward the ridge axis while dyke layers dip away from the axis and remain rather steep (Fig. 1).

Recent studies using magnetic data from exposures in the Blanco Fracture Zone have recorded these dipping reversal boundaries [Tivey 1996, Tivey et al. 1998], but the question remains whether a fracture zone represents "normal" oceanic crust. Other research using magnetic data from drill cores has identified multiple magnetic reversal boundaries within a vertical section of crust [Tivey et al. 2005]. This suggests that significant overlap occurs between sections of normal polarity and reversed, but the lack of drill cores, the cost, and the uncertain lateral correlation between distant cores leaves utilizing individual drill core data unfavorable for analyzing a cross-section of crust.

In this study, we present findings of a dipping reversal boundary located on the south wall of Endeavor Deep. Few places in the ocean offer a tectonic window that supplies a large enough exposure of bedrock created at a fast-spreading center and is located in a region of a known sea surface reversal boundary. Our location in Endeavor Deep not only supplies us with an ideal study area by exposing fresh unaltered oceanic crust, but also provides us with a significant perspective of the vertical structure of typical oceanic crust.

2. Data

Data for this study were collected during January-February, 2004 aboard cruise TN165. A deep-tow, 3-component magnetometer mounted on the ROV Jason was used to collect magnetic readings from the sloping crustal exposure at Endeavor Deep. This slope is located on the southern wall of a current amagmatic rift between the Nazca Plate and Juan Fernandez Microplate (Fig. 2a), and lies within magnetic anomaly 2a along the boundary of a magnetic reversal. The exposure consists of the entire extrusive layer, pillow/dyke transition zone, and upper most section of dykes.

During the cruise three vertical profiles (078, 079, 081c) tied together by several horizontal transects (081d, 080, 080a, 080b) were collected to ensure adequate coverage of the study area (Fig.2b). In situ observations, rock samples, and rock orientations were also taken for related work regarding the structure of oceanic crust.

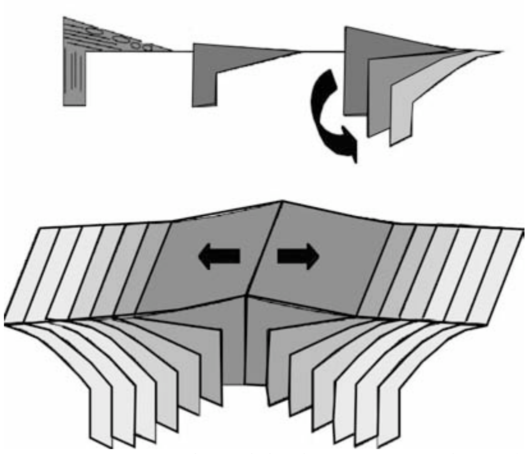

Figure 1. Proposed model of ocean crust formation. The extrusive layer dips shallowly near the surfaces and increases in dip with depth.

---

[1] Currently at Winona State University, Winona, Minnesota

3. Methods

3.1 Corrections

Several corrections to the raw magnetic data were performed to obtain the anomalous magnetization that is associated with the observed anomalies on the seafloor. These corrections include: 1) orientating the magnetometer, 2) removing an induced magnetic field, and 3) removing the regional magnetic field.

The initial orientation of the magnetometer was determined by spinning Jason in the water to observe sinusoidal orientation in x, y, and z coordinate vectors. The amplitude and phase of each sinusoid was then used to calculate the original orientation of magnetization. The total magnetic intensity was then determined by summing the squares of the x, y, and z magnetic vectors.

An induced magnetic field is created by the ROV upon which the magnetometer is mounted. This induced field adds to any data obtained and needs to be filtered, as it is unrelated to the magnetization of the rocks. Filtering of the induced field is done at the same time as spinning is taking place. In addition, the regional magnetic field created by the earth also adds or subtracts to any magnetic readings taken depending on their polarity. Removing the regional and induced fields leaves only the anomalous field, which is in the range of –4000 to 4000 nT.

3.2 Modeling

Forward modeling was performed with the anomalous magnetic intensity for each transect to locate areas of reversals or changes in magnetic intensity using code developed by Tivey [1996] for the studies conducted in the Blanco Fracture Zone. Set parameters of regional longitude and latitude (–110° and –32°, respectively), source layer thickness (1km), observation level (10 m), and orientation of the ridge axis (10°) were used for all our model runs. Using the current orientation of the East Pacific Ridge at 10° off north south imparted no skewness values to our model. All of these parameters can be varied, but for the purpose of our study they remained fixed.

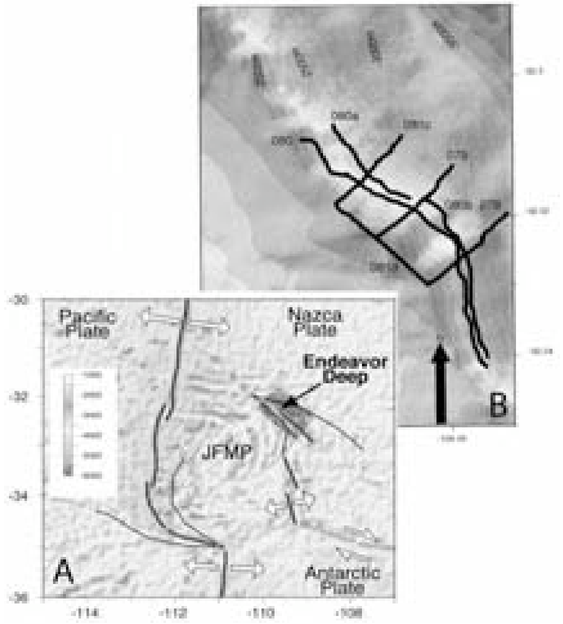

Figure 2. A) General location of Endeavor Deep, between the Juan Fernandez Microplate and the Nazca Plate. B) map view location of track lines used to collect magnetic data.

Magnetic modeling of each vertical and horizontal profile was performed assuming the initial crustal magnetization of 5 A/m. The location of polarity transition was varied to obtain a visual best-fit between the observed and predicted magnetic intensity profile. For some of the magnetic polarity intervals, the magnetic intensity was increased or decreased from the initial 5 A/m to obtain a better fit (Fig. 3). Each of the resulting models was then projected back onto the scarp for correlating and mapping purposes (Fig. 4).

4. Results

Many polarity transitions are observed within the profiles along with several changes in magnetic intensity that are not necessarily changes in polarity. These polarity reversals are present in the horizontal and vertical transects. Three reversal boundaries can be identified when the modeled data is transferred to the wall and sections of normal and reversed polarities are correlated. In addition multiple rock bodies with differing polarity intensities can be found in larger sections of opposite polarity. These anomalous areas are small-scale magnetic intensity variations and are not used in determining our larger scale dipping reversal boundaries. Modeling of the magnetic data reveals numerous drops in magnetic intensity within a uniform polarity (Fig. 3). These drops in intensity appear in the corrected data to be small reversals, but modeling reveals that they are simply areas in which the magnetic intensity has changed.

4.1 Vertical Profiles

Profile 079 shows three bodies of alternating polarity. Moving from the top of the scarp to the bottom, it starts normal, becomes reversed, and then back to normal polarity. The upper most body of normally magnetized rock reflects a drop is magnetic intensity about a third of the way down (Fig. 3). This change in magnetization is not a reversal as indicated by the raw data, but rather a change is magnetic intensity associated with the rock located in this area.

The middle vertical profile, 079, indicates four bodies of alternating polarity. The top of the transect starts with reversed polarity and goes to normal then reversed, and ends with normal polarity again. No changes in magnetic intensity were observed for this transect.

The last vertical profile, 081c, only shows two bodies of opposite polarity. The majority of the upper section is reversely magnetized and has a modeled drop in intensity half way through. The lower section shows normal magnetization, but displays a very weak intensity compared to the rest of the profile.

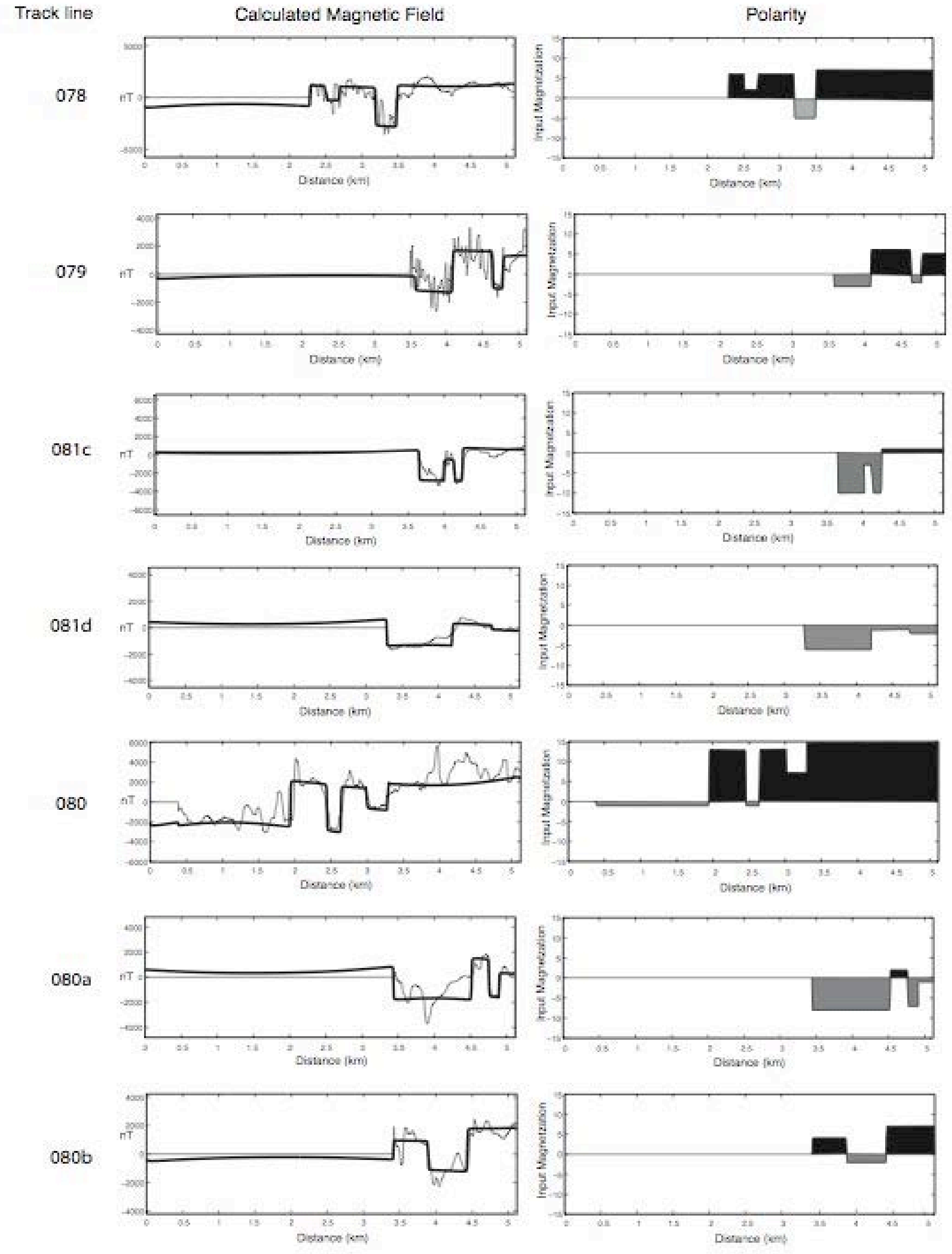

Figure 3. Modeled magnetic data from each track line along with corresponding polarities. The real data is shown as a thin line while the modeled data is in bold. Vertical profiles are 078, 079, and 081c and start at the top of the wall and go down with depth. Profiles 081d, 080, 080a, and 080b are horizontal transects. It is important to note that these transects were collected starting at the right side of the wall and move to the left, so when comparing with data on the wall, they must be flipped.

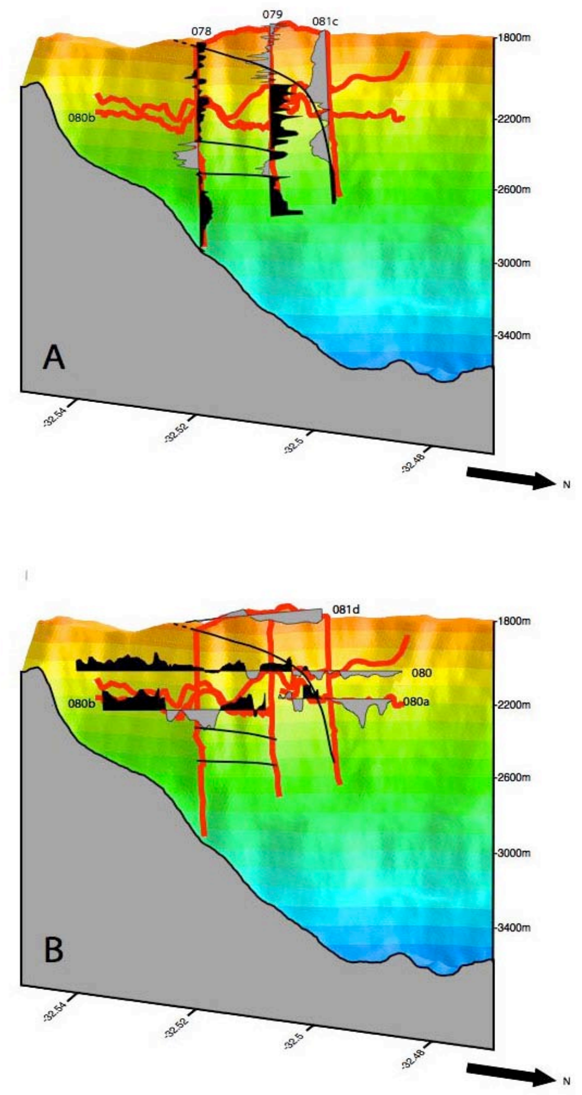

Figure 4. Magnetic modeled data superimposed on wall with reversal boundaries mapped in (bold black lines). A) Vertical profiles B) Horizontal profiles. The corrected magnetic data is shaded in according to the modeled polarity readings. Black shading refers to normal polarity; gray shading refers to reversed. Track lines are highlighted in red.

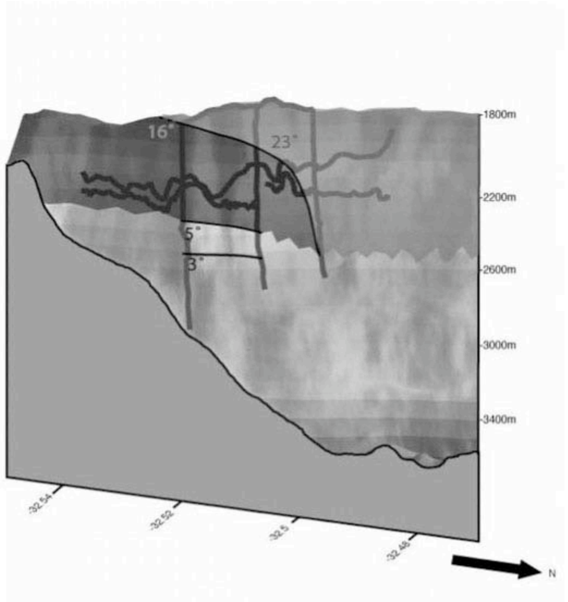

Figure 5. Mapped area of reversal boundaries with dip angles. The vertical exaggeration is 3:1. Shading is an extension of anomaly 2a observed on the sea-surface (black is normal polarity, grey is reversed).

4.2 Horizontal Profiles

Transect 081d, located at the top of the escarpment, is all reversed polarity. Several changes is magnetization occur, which may have to do with its location at the edge of the slope. The reversed intensity does decrease, however, closer to the east side of the transect, which is towards the transition between reversed and normally polarized crust.

The longest profile is 080 and the most complicated to model (Fig. 3). Four major sections of alternating polarity are shown. The two areas of reversed polarity show weak magnetic intensity compared to the intensity of the normal bodies. The left section of the profile also demonstrates multiple changes in intensity and has the highest magnetic readings of any of the transects.

Track line 080a has three bodies of differing polarity. Starting on the right side of the scarp, the magnetic profile goes from reversed to normal and then back to reversed. The areas of reversed polarity are strongly magnetized with the exception of a weaker intensity at the very end (Fig. 3). The small area containing normal polarity also shows weaker overall intensity than the reversed sections.

The last horizontal transect is 080b and is a continuation of 080a. Three sections of polarity are identified and modeled, as normal, reversed, and normal. The normally polarized areas contain stronger magnetization values than the reversed section. No changes in magnetic intensity are observed in any of the three areas.

4.3 Dipping Boundaries

Placing the modeled polarity profiles of each transect on the wall (indicated by gray and black shading of the data in Fig. 4) shows a clear magnetic reversal is present along the scarp. The west side of the wall is dominated by reversed polarity while the east side is normal indicating that the reversal boundary is located within magnetic anomaly 2a. Correlating the vertical profiles with the horizontal transects, a boundary can be drawn from the top of 078, through 079, across 080 and 080a, to the bottom of 081c. This boundary has an initial dip of 16° at the top of 078 and gradually steepens to 23° just after 079 (Fig. 5).

Two more possible reversal boundaries are located between 078 and 079 towards the bottom of the scarp.

Without any horizontal transects to verify the correlation between these highly magnetized areas of reversed polarity, it is difficult to know if this feature is laterally continuous. Dip angles are calculated to be 5˚ for the upper boundary and 3˚ for the bottom boundary. Assuming all three boundaries are correct, four alternating layers of polarity are identified within this vertical section of oceanic crust.

4.4 Anomalous Bodies

Several anomalous bodies of reversed polarity are found among larger sections of normal rock. These bodies tend to have weaker magnetic signals but still display an opposite polarity. Transects 078, 079, 080, 080a, and 080b all contain these anomalous bodies (Fig. 4). Because the “hiccups” contain the same signature (a small reversed blip in a larger section of normal crust) they may be the result of some later, off-axis volcanism [Sohn and Sims 2005], which is unrelated to the initial onset of crustal formation.

5. Discussion

The top boundary mapped at Endeavor Deep strongly supports the recently proposed models of crustal accretion at intermediate to fast spreading rates. Our boundary goes from shallow dipping in the extrusive layers to steeper dipping associated with the transition zone. Dip angles are predicted to be around 15˚ and 30˚ for the model, which is consistent with our study.

Structural observations and orientations taken at Endeavor Deep during the same cruise match the dipping reversal boundaries we mapped [Popham 2005]. Popham estimates an average dip angle in the extrusive layers to be around 17˚ with dips ranging from 15˚ to 25˚, well within range of our dips at 16˚ and 23˚ in the top boundary. Furthermore these structural observations record a steepening of dip angles with depth in track line 079. This track line intersects the location of the top reversal boundary and strongly correlates with our data.

Studies conducted on a similar escarpment at the Blanco Fracture Zone conclude similar results [Tivey 1996, 1998]. Dipping reversal boundaries, much like those mapped in this study, were used to support the recently proposed models of ocean accretion (Fig.1), however, the fact that Blanco is located at a fracture zone calls into question the validity of these results in modeling “normal” ocean crust. After comparing our study area, which is representative of typical oceanic crust, it is safe to assume that the Blanco Fracture Zone does indeed portray an accurate window into the vertical structure of oceanic crust.

Farther down the escarpment two more possible boundaries are identified, but because of their low dip angles and lack of horizontal magnetic data to accurately correlate these reversed magnetic bodies, they may not be labeled as true reversal boundaries. A better explanation as to why these intensely magnetized bodies of reversed polarity rock are located in an area of normal polarity is off-axis volcanism. Magmatic penetration up to ~20 km off-axis has been documented and is attributed to bending of the lithosphere which creates conduits for magma to flow. These cracks allow for the emplacement of sills and dykes several kilometers off-axis in already solidified bodies of oceanic crust [e.g., Sohn and Sims, 2005]. This mechanism of late-stage intrusion can also explain the other smaller reversals located in transects 080 and 080a.

6. Conclusion

A distinctive dipping top reversal boundary is present on the vertical escarpment on the southern wall of Endeavor Deep and can be correlated to anomaly 2a mapped on the sea surface (Fig. 5). This boundary begins dipping shallowly at 16˚ and gradually increases to 23˚ through the pillow/dyke transition zone. Since our study area is located at the edge of a propagating amagmatic rift it is an ideal location to study the structure of “normal” oceanic crust, and our findings here support the rotating model of ocean accretion and previous studies conducted in fracture zones.

The middle and lower boundaries appear to be two more reversal boundaries, but are best interpreted as later stage intrusions from off-axis volcanism. Multiple bodies of strongly magnetized rock differing in polarity can be found in areas dominated by the opposite polarity. These “hiccups” strongly suggest late stage off-axis volcanism in the area, and cannot be factored into determining the larger scale reversal boundaries.

Acknowledgments. We would like to thank the National Science Foundation for providing the funding to the SURFO program, the researchers and crew aboard cruise TN165, and everyone associated with the 2005 SURFO program for making this research possible.

References

Christeson, G.L., Purdy, G.M., and Fryer, G.J., Seismic constraints on shallow crustal emplacement processes at the fast spreading East Pacific Rise, *J. Geophys. Res. 99*, 17,957-17,973, 1994.

MacDonald, K.C., Fox, P.J., Alexander, R.T., Pockalny, R.A., and Gente, P., Volcanic growth faults and the origin of Pacific abyssal hills, *Nature, 380*, 125-129, 1996.

Sohn, R.A., and Sims, K.W.W., Bending as a mechanism for triggering off-axis volcanism on the East Pacific Rise, *Geology, 33*, 93-96, 2005.

Tivey, M.A., Vertical magnetic structure of ocean crust determined from near-bottom magnetic field measurements, *Journal Geophysical Research, 101*, 20,275-20,296, 1996.

Tivey, M.A., Johnson, H.P., Fleutelot, C., Hussenoeder, S., Lawrence, R., Waters, C., and Wooding, B., Direct measurement of magnetic reversal boundaries in a cross-section of oceanic crust, *Geophysical Research Letters, 25,* 3631-3634, 1998.

Tivey, M.A., Larson, R., Schouten, H., and Pockalny, R., Downhole magnetic measurements of ODP Hole 801C: Implications for Pacific oceanic crust magnetic field behavior in the Middle Jurassic, *Geochem. Geophys. Geosyst.*, *6*, 2005.

A.C. Shields and R.A. Pockalny, Graduate School of Oceanography, University of Rhode Island, Narragansett, RI 02882. (acshield6166@winona.edu, robp@gso.uri.edu)

Grain Size Analysis of ACEX cores

Betsy Zunk, [1] Kathryn Moran and Matt O'Regan

Graduate School of Oceanography, University of Rhode Island, Narragansett, Rhode Island

Abstract. Global warming has been a hot topic lately and there are many ongoing studies to better understand the Earth's climate. One area that is an ideal site for climate study is the Arctic. Relatively little is known about the sediments that lie beneath the sea ice of the Arctic Ocean, because it has never been cored to a deep depth. Recently, the first scientific drilling expedition to the central Arctic Ocean was completed. The expedition recovered sediment cores from deeper than 400 meters below the sea floor covering the Cenozoic (65 Ma). The location of the drill site is the Lomonosov Ridge. It is thought to once have been a part of the continental crust off the Eurasian Plate. This ridge has gradually subsided as it moved northward and now rises about 3km above the surrounding abyssal plains. Its elevation means that sedimentation on the ridge remains unaffected by turbidity currents, making it an ideal site to core. The sediment cores recovered from the Lomonosov Ridge hold a record of the past climate. The climate record is extracted using various physical, chemical, geological, and biological techniques. One of the physical tests, and the focus of this research, is grain size analysis. The methods that will be used to determine differences in grain size are sieving, hydrometer, and the Malvern laser analysis. Because changes in the depositional environment often affect grain size distributions in sediments, grain size can help determine past climates. On the elevated Lomonosov Ridge, coarse grained material is believed to be deposited by sea ice or icebergs. Differences in grain size throughout the cores will help determine the occurrence and duration of glacial periods in the Northern Hemisphere, and test the existing paradigm that North Hemisphere glaciation began ~2.5 Ma.

1. Introduction

The Arctic has always been an area of interest, because of its influence on the Earth's climate. The Arctic has an influence on climate because this is where the deep waters forms and it is the area that reflects the most light back into space keeping the earth's temperature moderate. Until the summer of 2004 there has been little known about the Arctic's paleoclimate. The Arctic Coring Expedition (ACEX), which happened in the summer of 2004, was the first alternate platform leg of the new Integrated Ocean Drilling Program. One of the challenges of this expedition was keeping the drill ship in one place long enough to keep the drillstring in the seabed so that conitnous coring operations could be performed in the moving sea ice. To overcome this challenge, they used an ice management strategy, which entailed two other ships that were icebreakers to break up the pieces of sea ice before it reached the drill ship. The site that they chose to drill at was the Losmonosov Ridge in the central Arctic. The ridge is theorized to have once been part of the Eurasian plate, around 56 million years ago. At this time the Gakkel ridge became an active spreading center and this sliver of continent started to breakaway. The reason they chose this site is because of its elevation in the water. The ridge rises about 3 kilometers above the surrounding abyssal plain which indicates that it is high enough off the ocean bottom to be out of the reach of turbidity currents and bottom currents that would resuspend the sediment and cause erosion. The ridge was also around 1300 meters below the ocean surface so it is out of the active zone of surface currents. They also drilled in the middle of the ridge, far from the places where the ridge meets the continental shelf, so that sediment deposition would not be affected by river discharge or other continental shelf processes that could carry coarser material (Figure 1). Theoretically this means that that sediment deposition on the ridge is from very fine material that settles out of the water column, or from coarser material that is carried by ice to the Central Arctic and deposited as ice rafted debris (IRD).

There have been studies in the past about the earth's climate from the Arctic, but have not been able to study more than a 10 meter core that does not tell to much about the paleoclimate. This expedition is to help further understand the Northern Hemisphere Glaciation and the Arctic's role in climate change by recovering cores that go down to around 400 meters below the sea floor. It is the common belief that permanent ice cover in the Northern Hemisphere began around 2.5 or 2.7 million years ago (Raymo 1994). Much of this evidence comes from occurrences of ice rafted debris or IRD found in the high

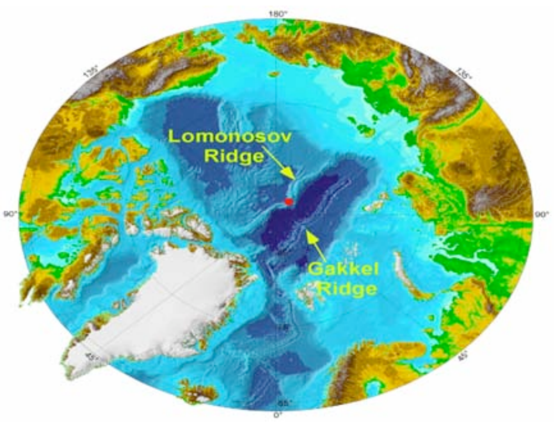

Figure 1. Picture of drill site in the Central Arctic. The Amerasian is on the left side of the Lomonosov Ridge and the Eurasin is on the right side of the ridge.

---

[1]Now at Muskingum College, New Concord,OH

northern latitude sites around 2.7 million years ago. The IRD was found from other ODP drilling expeditions in the North Atlantic and in the Norwegian and Barents Sea (Table 1). There has also been some cores from the Northern Pacific and the sediments contained the same fauna as the North Atlantic cores (Haug et al., 2005). Recent studies have shown that stratification in the subarctic Pacific could have help trigger the initiation of Northern Hemisphere glaciation (Haug et al.. 2005). These IRD events coincided with other climate proxy records like the O18 record, where changes in the O18 of benthic microfssils track ice-volume changes (Raymo 1994).

One possible reason for the initiation of glaciation around this time is the closing on the Isthmus of Panama. The closing of the Isthmus of Panama increased moisture and some heat transfer to the Northern Hemisphere. Increasing moisture and freshwater transport to the Arctic. This event is believed to have occurred in the late Miocene early Pliocene. The closing of the Isthmus of Panama redirected the warm Gulf Stream up the coast of North America. Since the Gulf Stream is a warm body of water it also brought heat with the excess moisture, and caused a slight warming around 4.6 million years ago with full glaciation not until around 2.5 million years ago (Driscoll, Haug 1998). It is thought that the excess moisture and heat overrode the consequences of more freshwater for some time in the Arctic and this could be a reason why glaciation succeeded closer to 2.7 million years ago (Driscoll, Haug 1998).

Once sea ice was established on the Arctic Ocean it acted like a barrier between the ocean and the atmosphere. The atmosphere is effectively cut off from the high heat capacity of the ocean and the earth's albedo (reflectivity) is increased from the ice cover. The ice cover on the poles acts like a land mass and cools the earth. The O 18 record is used as a paleothermometer for calculating temperature and the ice volume (Figure 2). The O 18 record also shows major changes in the earth's climate from the green house world to the icehouse world. The O 18 record shows the gradual cooling of the earth.

Leg	Site	Longitude	Latitude	Ocean/Sea
165	999	78˚ 44'W	12˚ 45'N	Caribbean
108	659	21˚ 02'W	18˚ 05'N	Atlantic
145	882	167˚ 36'E	50˚ 22'N	North Pacific
108	665	19˚ 40'W	2˚ 57'N	Atlantic
154	925	43˚ 29W	4˚ 12'N	North Atlantic
154	926	42˚ 54'W	3˚ 43'N	North Atlantic
154	928	43˚ 45'W	5˚ 24'N	North Atlantic
154	929	43˚ 44'W	5˚ 59' N	North Atlantic
81	552	23˚ 13'W	56˚ 17' N	North Atlantic
31	297	134˚ 16'E	30˚ 87'N	North Pacific
68	502	79˚ 38'W	11˚ 38'N	North Atlantic

Table 1. ODP Sites where ice rafted debris was found.

The earth's rotation around the sun affects the climate more than people realize. It affects the climate by the amount of solar radiation that reaches the earth. The obliquity of the earth is the earth's tilt or rotation on its axis. The larger the obliquity, the larger the seasonal contrast in the amount of light that reaches the earth. Milankovitch's theory predicts that glaciations are more probable when obliquity results in cool summers, and winter ice accumulations do not melt. Around 2.7 million years ago, there was a period of low tilt or obliquity that caused cold summers in the northern hemisphere. Milankovithc's theory also requires the other two orbital parameters, eccentricity and precession of equinoxes, to produce optimal glacial conditions. The larger obliquity was the final straw to send the world from a greenhouse world into an icehouse world (Zachos et al 2001). To have the other two parts work with the obliquity the eccentricity needs to be large and the aphelion need to be in the Northern Hemispheres winter, which it is today.

There are two different currents in the Arctic that control what areas have icebergs and what areas contain sea ice (Figure 1). The Beaufort Gyre is on the Western side of the Ridge in the Amerasian basin. The Beaufort Gyre has icebergs in its current that break off from the Greenland Ice sheet and from the Canadian Islands and those icebergs circulate in the gyre until the iceberg reaches a place either through the Bering Strait into the Pacific or through the Labrador Sea to the Atlantic and do not cross the Losmonosov Ridge. The other mode of circulation in the

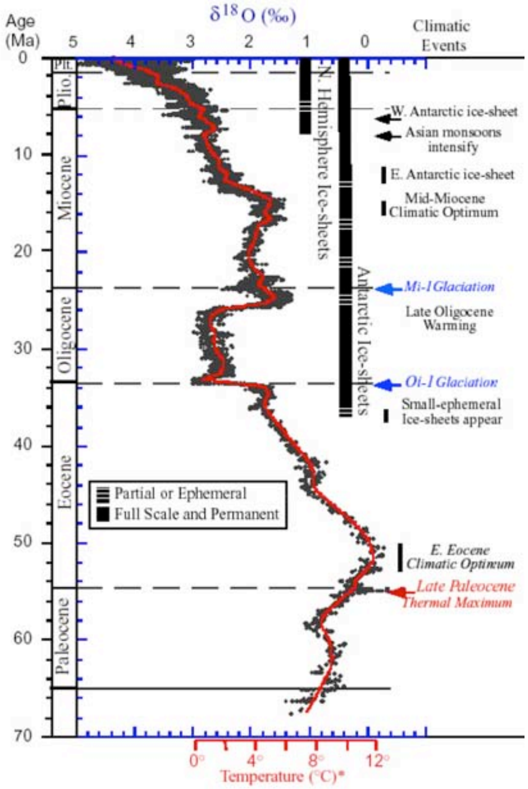

Figure 2. δ^{18}O Record. The larger δ^{18}O value corresponds to colder temperatures and indicates glaciation.

Arctic is the Transpolar Drift. This current contains sea ice that forms on the shallow continental shelves and entrains medium size sediment and then flows out through the Fram Strait into the North Atlantic. This describes the modern circulation pattern, however, sea floor images clearly show evidence of ice scouring believed to have occurred during the Pleistocene. This indicates that there was ice sheets over 1 km thick, or the presence of icebergs embedded in the sea ice, that crossed over the Lomonosov Ridge (Moran et al 2005). So this might mean that at one time the circulation pattern in the Arctic was shifted so the Beaufort gyre was over the Losmonosov Ridge.

Sea Ice forms on shallow Siberian continental shelves and is carried across the arctic in the transpolar drift. As the sea ice forms, the sediment that is suspended in the water column gets frozen into and entrained in the sea ice and then settles out as the sea ice melts. Sea ice normally carries the silt to the very fine sand grain size (3.91-125 microns). Icebergs on the other hand break off the thick continental ice sheets. Since icebergs are from the continental ice sheets the sediment the continental ice sheets have in them are from scraping the continental landmasses. The grain size that is expected to be carried in the icebergs is from the coarser part of the very fine sand up to the very coarse sand (90-2000 microns).

The goal of this project is to use the grain size distribution of the ACEX cores to track major climatic events associated with the Northern Hemisphere evolution of glaciation. To do this we aim to be able to distinguish between two different modes of transport for the coarser sediment that can only come from sea ice or icebergs because of the location of the drill site. The model that we came up with for this project is that sea ice contains medium size material, coarse silt to fine sand (31-175 um), and icebergs contain coarser materials, from fine sand to coarse sand (176- 2000 um) We predict that changes in the contribution of these size classes reflects changes in the dominant mode of sediment transport and can be used to distinguish between the presence of sea ice and icebergs.

2. Methods

2.1. Malvern Grain Size Analysis

Grain size analysis was performed using laser analysis with the Malvern Mastersizer 2000. This is a new machine acquired by the University of Rhode Island. The Malvern laser analyzer works by measuring the amount of light scatter by each particle. The way the light is scattered can be predicted by using the Mie theory. The Mie theory descrobes the way the light passes through or is absorbed by the particles. To use the Mie theory instead of the simpler Fraunhofer theory, which predicts the way light passed through a spherical solid particle, one needs to know the refractive index and absorption of your sediment samples or else your results will be wrong. The unique pattern produced from particles scattering light originates because each different size of sediments reflects the light in a different way than the next size. So this can be used as a fingerprint for grain size. The Malvern laser analyzer actually applies this theory backwards, and by finding the scattering patterns of the particles it calculates the grain size distribution of the samples. The optical unit is composed of many detectors and each detector only detects a certain size class. It only detects the scattering pattern from the particles that are passing the laser at that time. The detectors take a reading or a picture every millisecond so it takes many pictures and then averages them together. The Udden Wentworth grain size scale is used to bin the data into appropriate size classes for presentation

2.2. Sample Preparation

There were 167, 5-gram samples that were used in this analysis. The amount of sample required by the Malvern Laser Analyzer was dependant on the average grain size of the sample. For more silty sediments, which were what the Arctic sediments were, the analyzer only needs around 0.2 grams. The Malvern Laser Analyzer only can measure grain size from 2 millimeter in diameter and smaller. To remove > 2 mm particles samples were sieved prior to running. To make sure that our sample was a good representative sample, there were 3 splits (0.2 grams each) taken from each sample. Each split was put into a jar and then soaked in a 10 ml of 4 molar sodium hexametaphosphate, which was a dispersant so the particles do not stick together or flock. Just enough of the dispersant was used to make sure the sediment was covered so not to put to much extra liquid into the Malvern Laser Analyzer. The samples are then left to soak in the dispersant for 24 hours. After the 24-hour period each sample is put into a sonification bath and left for at least 10 minutes. The sample is taken directly from the sonification bath to the Malvern Laser Analyzer. The Malvern Laser Analyzer is previously set to a specific refractive index and other measurement instructions for that individual type of sediment. The settings that were used for every sample are the solution was set at water and the refractive index was set at the Franhofer. The sample is then rinsed into the Malvern Laser Analyzer water bath, called the Hydro 2000, with distilled water and each sub sample is run through the laser 3 times to ensure that the results are reproducible and that there was no air bubbles. All together the samples were run 9 times to make sure that the sample is representative and results are reproducible. After the data is collected the data can be tweaked and interpreted to see what the results are. The data is automatically put into data sheets that show the grain size class in a table and in a continuous graph. The Malvern Laser Analyzer even divides the data into each individual phi and micron size so that the clay size encompasses a few different size classes.

2.3. Traditional method for grain size analysis

The sieve and hydrometer method, which is the traditional method for grain size analysis, were also used on a few samples to use as a comparison to the new machine. The samples were soaked in the sodium hexametaphosphate for 24 hours and then they were wet sieved down to 63 microns. The samples were then put in the oven to dry. The samples that were caught in the sieves were then weighed to get that size class percentage of the sample. Then 50 grams of the sediment dry weight was taken out of the sediment that passed through all the sieves and into a pan. The remainder of that sediment was weighed too. The 50 grams was soaked in sodium hexametaphosphate overnight to get ready to run the hydrometer on the sample. The Hydrometer is only used on sediment less than 63 microns. After the soaking period the sample was then stirred and put into a 1000 ml cylinder. The cylinder was then filled up to the 1000 ml line with distilled water and then shaken to make sure the sediment has an even distribution in the solution. As soon as the cylinder is put down after shaking the timing starts and measurement are taken on the hydrometer at 2, 5, 15, 30, 60, 250, and 1440 minutes. The hydrometer method only gives the grain size to 1.5 microns. To know the further distribution and more in-depth analysis of the smaller grains the experiment would have to go on for a week or two.

2.4. Comparison between the two methods

The Malvern Laser is a better more accurate method than the hydrometer method especially when the grain size is in the silty category. Using the Malvern Laser you can get the sample run after the preparation in a half hour rather than a week. The Malvern Laser Analyzer is more reliable for a sample mainly composed of silt and clay materials. The Malvern also give a more detailed analysis of all the grains sizes it reads

3. Results

3.1. Initial Results

The data from the Malvern Laser Analyzer was put into a spreadsheet to compare the points and to find any trends. The first plot made with the data was a scattered x-y plot (Figure 3). The Analyzer already divided up the grain size distribution of the samples into the 8 different size classes shown on the plot. The size classes are from the Udden Wentworth Grain Size Scale. This plot compares what percentage of that sample falls into the different size classes (y-axis) compared to the percent clay size that is 0-2 micron (x-axis). This plot shows that as clay increases the fine silt also increases, so the fine silt has a positive correlation with the clay. On the other as the clay increases the coarse silt decreases, so it has a negative correlation with clay. This may mean that the coarse silt may be an indicator of IRD, which could be either sea ice or iceberg transport. The most likely cause of this size of IRD is from sea ice transport. The silt category, from 3.91-31 microns, does not have either a positive or negative correlation. This may mean that the silt category covers too wide of a grain size range. It is possible that if subdivided, a portion of the silt class will have a positive correlation and the other half will have a negative correlation.

The next plot that was made was a down hole plot

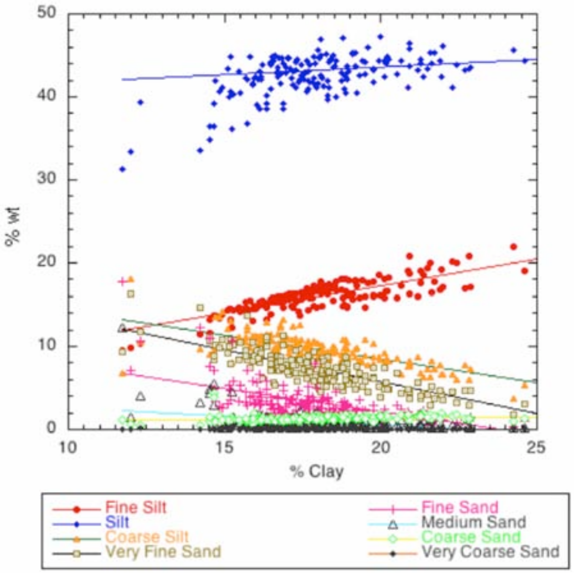

Figure 3. Grain Size trends

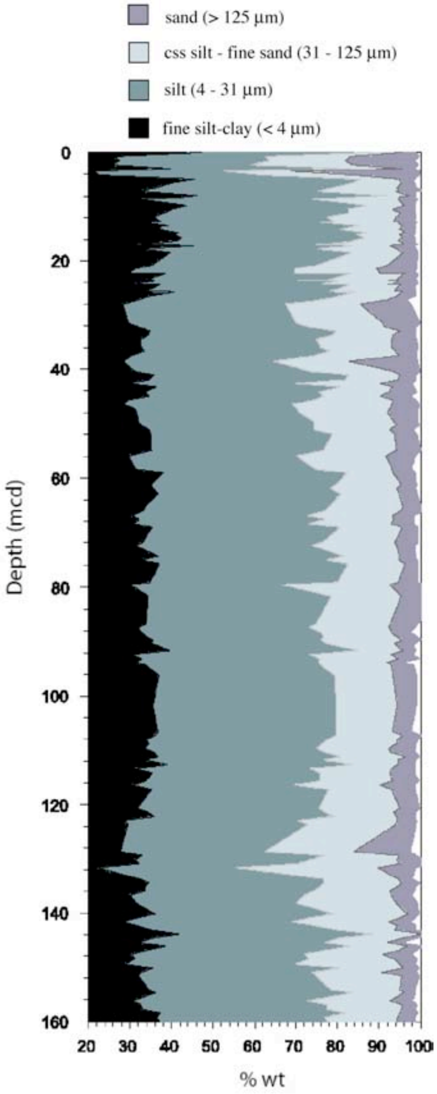

Figure 4. Down hole plot of depth Meters Composite depth is a revised depth using magnetic reversals to make a continuous core from the different drill site

with depth on the y axis and percent weight or composition on the x-axis (Figure 4). Some of the size classes were grouped together to make the plot easier to interpret and the sizes that were grouped shared the same trend. There are a few sections that are points of interest. One section is around 130 meters composite depth (mcd). This could be an area of IRD, probably from iceberg transport since it is coarser materials. The next area is the interval between 28 and 43 mcd. This area has more coarse material in it while the silt and clay percentage becomes less. The last area is one that is fairly recent in geological time and it is in the interval between 0 and 8 mcd. This area shows some major jumps in the coarser material percentage, which would indicate IRD. Both of these last two areas would likely indicate IRD deposition related to icebergs since the grain size favors coarse materials from fine sand to coarse sand. The samples that were run were only down to 200 mcd out of the possible 400+ mcd drilled during ACEX.

4. Discussion

After the original plots were made from the data, there needed to be a way to be able to tie the major grain size changes with periods of known climatic change in the geologic past. To do this, the down hole plot was recreated with age instead of depth. To convert depth to age, a preliminary age model was used (Figure 5). The y-axis is the depth and the samples are plotted against age (x-axis). Other members of the scientific party on the ACEX cruise created the age model, and they are still working on revising it. The age model was created using a combination of magnetostraigraphy and biostratigrpahy. Each of the red dots on the plot is the depth and magnetic reversals that they matched up with the well-known record of the earth's magnetic reversals. To use this age model one would find the depth on the y-axis and draw a straight line over to the line and then go straight down to the age on the x-axis. This is how the depth down hole plot was changed into an age down whole plot (Figure 6). The reason this plot was changed into an age down hole plot is to be able to compare the major climatic events taken from the O18 records to our grain size data to see if the major climatic events can be seen in the grain size distribution. So looking at the points of interest from the plot it can now be determined if some of those events were IRD events. The first point of interest is around 10 to 11 millions years ago and actually is around the same time period of an IRD event that was tied to the O18 record (Zachos et al 2001). Also this event is around the same time as the opening of the Fram strait and deposits of IRD material from icebergs found there.

The next point of interest was dated around 2 to 3 million years ago and this is around the time of the intensification of Northern Hemisphere Glaciation according to the O18 record (Zachos et all 2001). At this time there is expected to be an increase in coarser grain size and there is. The clay and silt size particles decrease in percentage during this time. The sediment records of the recent half million years shows the glacial

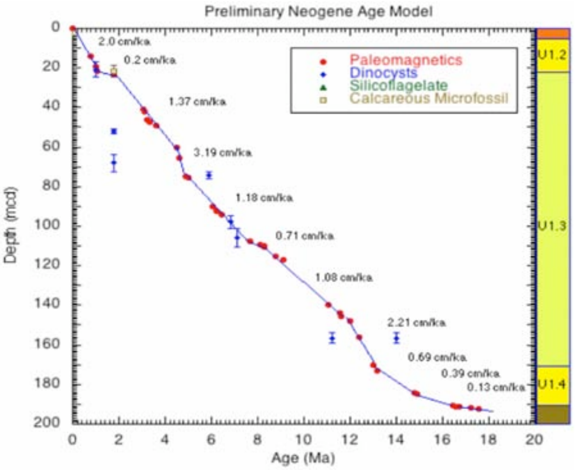

Figure 5. Age model developed by the shipboard scientific party.

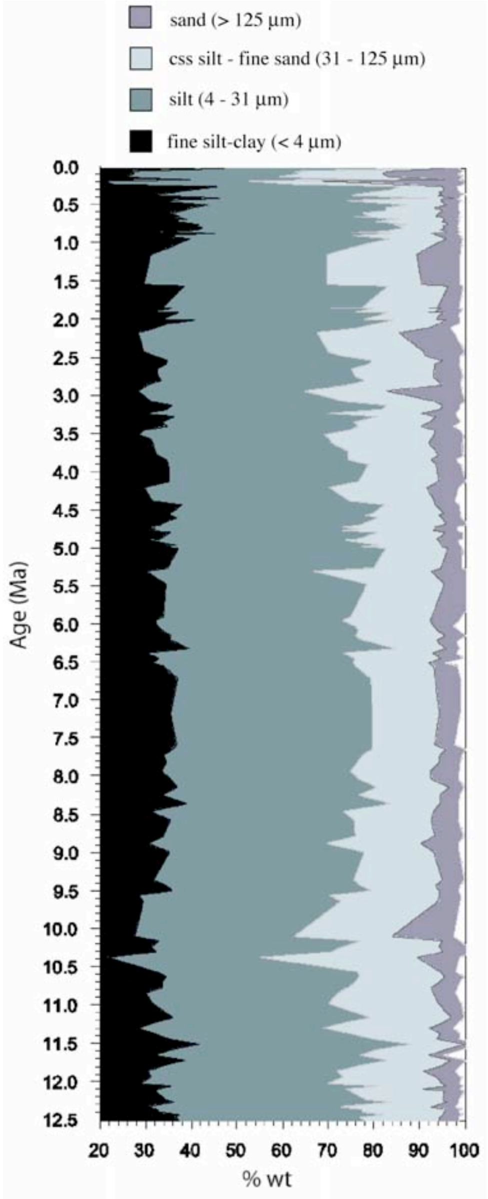

Figure 6. Age model developed by the shipboard scientific party.

interglacial periods that are known to have occurred in recent history. The two long points of the coarser material would indicate, according to our model, that this was during a glacial period that had icebergs present above the Lomonosov Ridge. The clay and silt size class goes way down during the glacial periods. These points of interest of the data show that grain size may be a sensitive indicator of climatic changes in sediment from Lomonosov Ridge.

There is one climatic change that grain size is not showing around 1 million years ago, the Mid-Pleistocene Revolution (MPR). During this time the earth's climate or ice dynamic were shifting to more pronounced periods of glacial- interglacial cycles, which continue today. The MPR was a major event because the earth climate cycles shifted to a longer period, which was 40 to 100 ka, so there could be a longer time for the ice to accumulate. This is known from the O 18 record by how the variability increases (Figure 2). So according to our model there should be peaks of coarser grain material and then of the medium size sediment like up above. This area of the grain size does not show the climate change so our model is not fitting properly. There are a few reasons that this grain size is not showing an increase in coarser materials. One reason could be that during this time the glaciation was very heavy and had an ice cap or solid sea ice/sheet in the Arctic so no icebergs could get through to deposit the coarser materials. Another reason is that there could have been a lot of icebergs and sea ice covering the Arctic, so the currents had less space to pass the ridge. The current started to get stronger from the less space, resulting in a winnowing effect on the Lomonosov Ridge. This means that the current eroded some of the sediment. The current did not have enough velocity to pick up the clay and silt material because they are cohesive. However the current was strong enough to pick up the coarse silt to the fine sand, but not strong enough to pick up the medium to the very coarse sand. This explains why the area of 'coarse silt to the very fine sand' is the smallest in this interval. The last reason is the age model is not refined enough and needs to be revised and have higher resolution across the areas in question.

Most of the points of interests that have been looked at so far have dealt with IRD deposits from icebergs since they are more noticeable. Iceberg size sediment is also easier to identify than sea ice deposition. There are places in the down hole plot that indicate sea ice deposition. These are the places where the very fine sand and coarse silt increase when the coarser material does not. One of these areas is around 10.5 million years. This area is also in the area of the opening of the Fram strait. This area is also just before the peak in the coarse grain category. Another area is around 11.5 million years ago and both of these surround the time period that it is thought that glaciation tried to initiate (Driscoll, Haug 1998). Another area is from 3.5 to 4.5 million years ago and this is another area that glaciation tried to initiate (Driscoll, Haug 1998). This is also another interval where the age model needs to be refined. The rest of samples from the deeper depths (>200 mcd) are needed to see the grain size analysis from the Mid-Miocene Climatic Optimum that is a well know ice-free time. So the grain size analysis can be used to help determine the differences between an ice-free environment and a sea ice environment.

5. Conclusions

The method of using grain size analysis to identify periods of glaciation from grain size records seems to show the major climatic events of the earth's history. There still needs to be more research on the deeper sediments to be able to compare the three types of arctic depositional environment, which are ice-free, sea ice, and icebergs/ ice sheets environments. The age model also needs to be revised to make sure the events are placed at the right time. Also there needs to be a higher resolution of samples, so that the areas of interest can be look at and analyzed further. Our model may also be too one variable and not taking in other factors like erosion and currents. The model does seem to be able to show the difference between sea ice, iceberg depositions

Acknowledgments. I would like to thank Dr. Kathryn Moran, Matt O'regan , GSO, and the SURFO program.

References

Driscoll, N.W.,Haug G.H. (1998) A Short Circuit in Thermohaline Circulation: A cause for Northern Hemisphere Glaciation? Science 282.

Haug et all. (2005) North Pacific Seasonality and the glaciation of North America 2.7 million years ago Nature 433

Moran, Kathryn et all. (not yet published) A First Look at the Cenozoic History of the Arctic Ocean.

Raymo, M.E. (1994) The Initiation of Northern Hemisphere Glaciation, Annual Reviews Inc.

Zachos, James et all (2001) Trends, Rhythms, and Aberrations in Global Climate 65 Ma to Present Science 292.

Betsy Zunk and Dr. Kathryn Moran and Matt O'regan, Graduate School of Oceanography, Univeristy of Rhode Island, Narragansett, RI 02882. (bzunk@muskingum.edu, moran@oce.uri.edu, oregan@gso.uri.edu)

---

[1] Muskingum College, New Concord,OH 43762